INTERNSHIP REPORT
(October 2016 - June 2017)

Author

Aurélien PÉLISSIER
ARPE Student

Study of High Harmonic Generation in high repetition rate systems

Supervisor : Arthur K. MILLS
Director : David JONES

Ultrafast Spectroscopy Laboratory
UBC, VANCOUVER, CANADA

Vancouver, June 2017

Abstract

High Harmonic Generation (HHG) involving noble gas targets with high repetition rates systems has proven successful regarding the significant improvements in electron imaging and attosecondphysic as well as photoemission spectroscopy. However, optimizing the conversion efficiency of the process is challenging because many parameters such as driving field intensity, gas pressure or nozzle diameter can be adjusted, and the highly nonlinear phenomenons involved in the harmonic generation make the choice not obvious. We study in this thesis all the parameters involved in high repetition rates HHG systems, focusing on ions dynamic, atomic response, phase matching and absorption. Measurements performed with a femtosecond enhancement cavity (fsEC) and numerical simulations with *COMSOL* are presented. A new dynamic nozzle design as well as a helium mixing technique to improve the conversion efficiency of the HHG process is also proposed.

Résumé

La génération d'harmoniques d'ordre élevés impliquant des cibles de gaz noble avec des systèmes à taux de répétition élevés a fait ses preuves en ce qui concerne les améliorations significatives en imagerie électronique, physique attoseconde et spectroscopie de photoémission. Cependant, l'optimisation du taux de conversion du procédé est difficile car de nombreux paramètres comme par exemple l'intensité du laser, la pression du gaz ou encore le diamètre de la buse peuvent être ajustés, et les phénomènes physiques fortement non linéaires impliqués dans la génération d'harmoniques rendent le choix non trivial. Dans ce rapport, tous les paramètres impliqués dans la génération d'harmoniques d'ordre élevés ont été étudiés, en s'intéressant plus particulièrement à la dynamique des ions dans le plasma, la réponse atomique quantique, les correspondances de phase entre les harmoniques et le fondamental et au phénomène d'absorption.. Des mesures effectuées avec une cavité d'amplification femtoseconde ainsi que des simulations numériques à l'aide de *COMSOL* sont présentés. Un nouveau design de buse dynamique et une méthode de mélange avec de l'hélium est également proposé pour améliorer l'efficacité du procédé de génération.
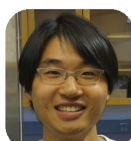
David Jones
Director

Arthur K. Mills
Post-doc

Fuhao Ji
Post-doc

MengXing Na
Master student

Michael Schneider
Engineer

Outline :

Notations

STP	Standard Temperature ($T = 0\,^\circ\text{C}$) and Pressure ($P = 1\,\text{atm}$)
$e = 1.602 \times 10^{-19}\,\text{C}$	Elementary electric charge
$m_e = 9.109 \times 10^{-31}\,\text{kg}$	Electron mass
$c = 299\,792\,458\,\text{m/s}$	Celerity of light in free space
$\hbar = 1.055 \times 10^{-34}\,\text{m}^2\text{kg/s}$	Reduced Plank constant
$\varepsilon_o = 8.854 \times 10^{-12}\,\text{F/m}$	Permittivity of free space
$\mu_o = 1.256 \times 10^{-6}\,\text{H/m}$	Permeability of free space
$\eta_o = \frac{1}{\varepsilon_o c} = 376.7\,\Omega$	Impedance of free space
$P_{\text{atm}} = 1013\,\text{mbar}$	Pressure at $1\,\text{atm}$
$N_{\text{atm}} = 2.7 \times 10^{25}\,\text{atoms/m}^3$	Gas density at STP
ω_1	Fundamental angular frequency
$\omega_q = q\omega_1$	Harmonic angular frequency
q	Harmonic order
$I(r, z, t)$	Laser intensity
I_o	Laser peak intensity
t_p	Laser pulse length (FWHM)
I_p	Ionization potential
$U_p \propto I$	Ponderomotive potential of the laser field
ω_o	Beam radius of the fundamental
P_{Cav}	Intracavity average power
$f(t) = \exp\left(-2\ln(2)\left(\frac{t}{t_p}\right)^2\right)$	Laser pulse envelope
P_0	Backing pressure
$P(r, z)$	Gas pressure
$\eta(r, z, t)$	Ionization fraction
V	Gas velocity
l_p	Nozzle diameter / Interaction length
z_{noz}	Nozzle position
δ	Difference from unity of the refractive index at STP
σ	Absorption cross section
$T_0 = 293\,\text{K}$	Room temperature
$T_i = 293\,\text{K}$	Ion temperature, taken as the room temperature
$T_e = 3\,\text{eV}$	Electron temperature
μ_i^0	Ion mobility in his parent gas at STP

Introduction

Since its discovery in 1987 [1], the High Harmonic Generation (HHG) process using noble gas targets has been widely studied and improved. It has enabled the generation of spatially and temporally coherent radiation from the vacuum/extreme ultra-violet (VUV/XUV) down to the soft X-ray region, which has led to significant improvement in electron imaging and attosecond physics (Fig.1). One of the most charming advantages of HHG sources is their realization on a table-top, making them particularly attractive as an alternative to large-scale facilities, such as synchrotrons or free electron lasers, which only offer restricted user access.
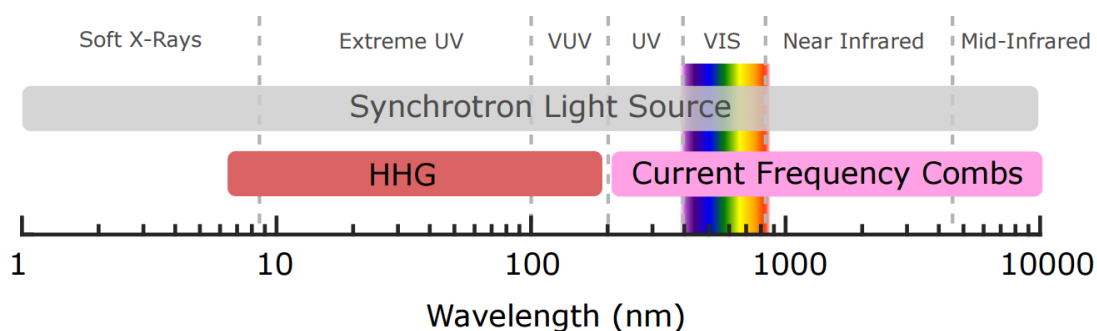
Figure 1: Range of electromagnetic spectrum covered by current-generation frequency combs. High harmonic generation (HHG) provides a way to extend this range to the VUV and XUV wavelength regimes, which are currently only accessible with synchrotron sources, from [2].

However the low repetition rate of traditional single-pass HHG sources $(1-500\text{kHz})$ causes a variety of problems including prohibitively low data rates and high peak XUV power, which makes them not ideal for many experiments such as photoemission spectroscopy. In the last decade, a new type of VUV/XUV femtosecond source has emerged by employing a femtosecond enhancement cavity (fsEC), reaching repetition rates up-to $100\,\text{MHz}$ [3, 4]. However, beside the benefits of such sources, the high repetition rate creates new challenges that were not encounter for lower repetition rate. For example, the plasma cloud does not have the time to fully leave the focus area between two pulses which leads to a higher plasma density in the interaction region and makes the HHG process less efficient. Another problem is that high repetition rate HHG requires tight focusing of the peak power driving pulses, and the conversion efficiencies that have been achieved in this regime are orders of magnitude behind the values that have been demonstrated with loose focusing [5].

In this work we precisely describe and study all the parameters involved in high repetition rates HHG systems. We give in Chapter I the basics tools to understand the HHG process, absorption, gaussian beam and refractive index. The Chapter II is dedicated to the behavior of the plasma cloud between laser pulses. And after having explained in Chapter III how to calculate the harmonic output power, we finally describe in Chapter IV the experimental setup and present some measurements to compare with our numerical simulations.

I Theoretical basis and preliminary work

I.1 The High Harmonic Generation process

High harmonic generation (HHG) refers to the process of creating vacuum or extreme ultraviolet (VUV or XUV) light through a nonlinear interaction of an intense laser field with gas (Figure.2). The pulses are usually focused in an open gas cell filled with a noble gas, and due to the extreme non-linear nature of this process, intense femtosecond laser pulses with intensities on the order of $1 \times 10^{14}\,\mathrm{W/cm^2}$ are needed.
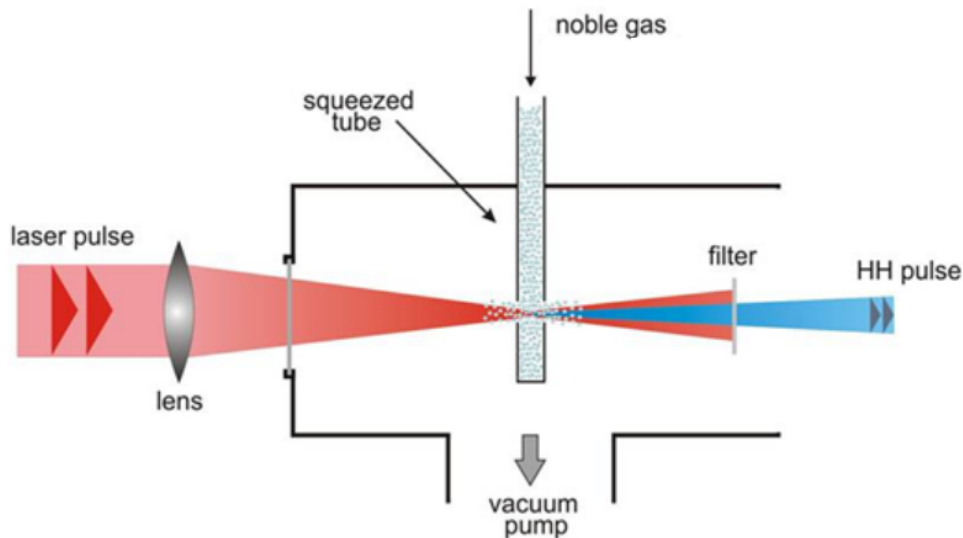
Figure 2: Generation of High Harmonics in a squeezed tube, from [6].

The harmonic order q refers to the ratio between the angular frequency of the harmonic ω_q and the fundamental ω_1. Due to symmetry conditions discussed below, q is always an odd number, and is limited by the ionization potential (I_p) and the ponderomotive potential (U_p) of the system. The harmonics are all generated simultaneously, and a typical obtained spectra is presented Fig.3(a) ; the cut-off harmonic is defined to be the last harmonic of the plateau, and can be calculated with a classical model discussed below. The Fig.3(b) is highlighting the differences on the harmonic spectrum for different gas.
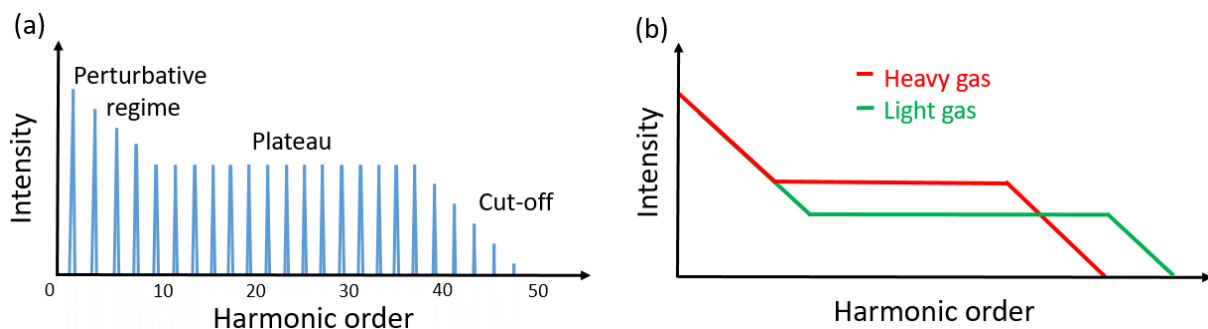
Figure 3: (a)Typical High-Harmonics spectrum. (b)For the same driving field intensity, using a heavier gas leads to a smaller plateau but a higher conversion efficiency.

I.1.1   The three steps model

The generation process with a laser field $\vec{E}(t) = \vec{E}_o \cos(\omega_1 t)$ can be described by a semi-classical three step model [7], first proposed by Corkum in 1993 [8]:
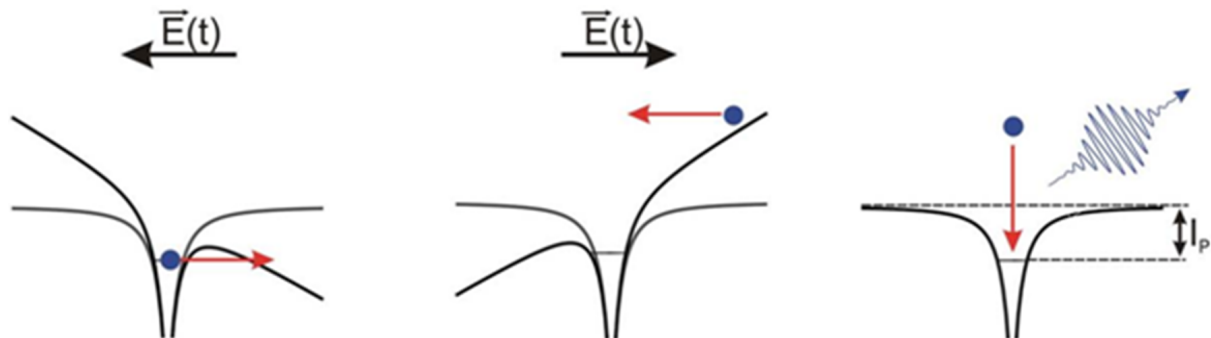
Figure 4: Three step model, from [6].

- *Step 1, Tunneling*: An electron is bound by the Coulomb potential of an atom. An incoming intense laser field distorts the potential and allows the tunneling of the electron through the Coulomb barrier (see II.1).

- *Step 2, Acceleration*: The freed electron is accelerated away from its parent ion by the laser field. After half an optical cycle the sign of the laser field reverses, this leads to an acceleration back towards the ion (see I.1.2).

- *Step 3, Recombination*: The electron recombines with its parent ion and emits a photon with its energy being determined by the ionization energy of the atom I_p and the kinetic energy of the electron gained by its interaction with the laser field (see B.3).

By conservation of energy, the generated photon cannot have energy higher than the sum of the electron kinetic energy and the ionization potential, the maximum photon energy (cut-off) is then given by [7]:

$$E_{\gamma,\mathrm{max}} = 3.17 U_p + I_p \quad \text{with} \quad U_p = \frac{e^2 E_o^2}{4 m_e \omega^2} \tag{1}$$

Moreover, the spherical symmetry of the atomic system imply that the symmetry of the electron cloud must also be spherical. This means that the polarization must satisfy the condition $P(E) = -P(-E)$. Given the fact that a general non-linear polarization can be described by an equation of the form [7]:

$$P(t) = \epsilon_0[\chi_1 E(t) + \chi_2 E(t)^2 + \chi_3 E(t)^3 + ...] \tag{2}$$

All even electric susceptibilities χ_{2n} have to be zero. And we are left with only the odds harmonics.

The ionization potential I_p of the most commonly used rare gas are given in Table.1, we notice that I_p is getting bigger for lighter gas, which imply that, as highlighted in the Figure.5, the intensity required to generate a given harmonic is higher for heavier gases.

Gas	Helium	Neon	Argon	Krypton	Xenon
I_p [eV]	24.6	21.6	15.8	14.0	12.1

Table 1: Ionization potential of common noble gas.
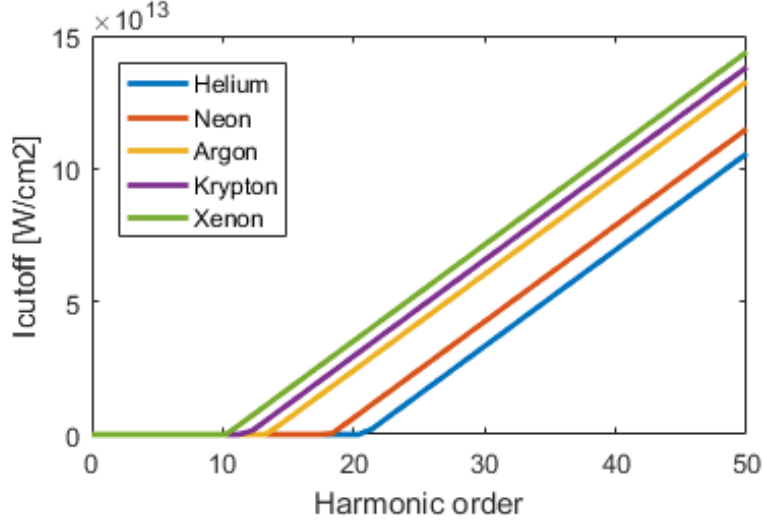
Figure 5: Required intensity (I_{cut}) to generate harmonic for most common noble gases, the driving field wavelength is $1050\,\mathrm{nm}$.

I.1.2   Trajectory and phase of the returning electron

In this section, we look deeper into the step 2 and study the behavior of freed electrons using a classical model. After the ionization at the time $t = t_o$, the motion of the freed electron is governed by the laser field:

$$m_e\ddot{x}(t) = -eE_o\cos(\omega_1 t) \tag{3}$$

The momentum $p(t)$ and the position $x(t)$ of the electron are then:

$$
\begin{aligned}
x(t) &= \frac{eE_o}{m_e\omega_1^2}(\cos(\omega_1 t) - \cos(\omega_1 t_o) + \omega_1(t - t_o)\sin(\omega_1 t_o)) \\
p(t) &= \frac{-eE_o}{\omega_1^2}(\sin(\omega_1 t) - \sin(\omega_1 t_o))
\end{aligned}
\tag{4}
$$

We now define the returning time t_r such that $x(t_r) = 0$, and calculate the return kinetic energy of the electron $E = p^2(t_r)/2m_e$. The Fig.6 gives the impact energy as a function of emission time.

From this figure we notice that, with the exception of the $3.17\,\mathrm{U_p}$ maximum impact energy at time $t_{max} = 18°/\omega_1$ given in Eq. 1, there are two emission times t_o that give the same impact energy, one shorter and one longer than t_{max}. An electron which as been freed at $t_o < t_{max}$ is called a long trajectory electron, and likewise, an electron freed at $t_o > t_{max}$ is a short trajectory electron.
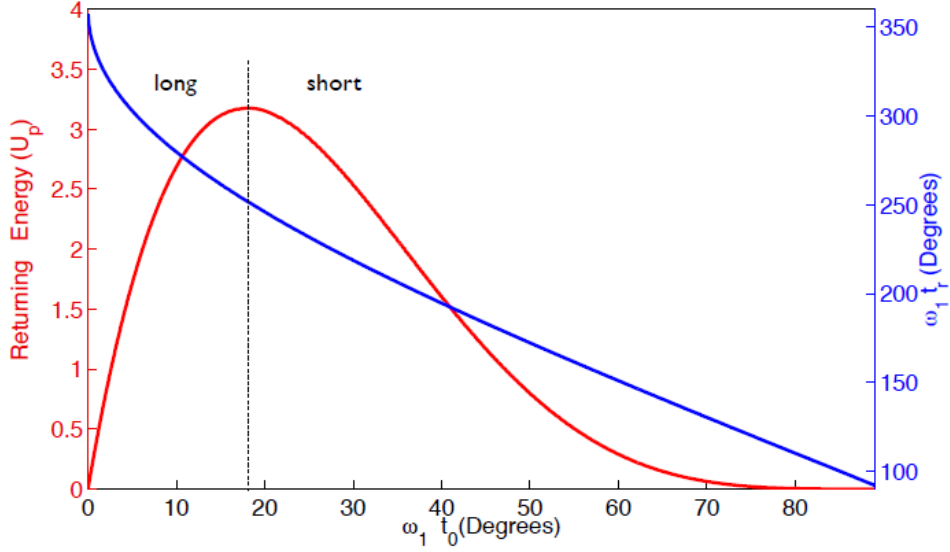
Figure 6: Time t_r and Kinetic energy at the re-impact on the atom for different electron emission times, taken from [9].

Long and short trajectory electrons have different phase shift, which can be calculated from the classical action :

$$S = \int_{t_o}^{t_r} L dt \tag{5}$$

$L = T - V$ is the Lagrangian, and for high intensities ($I \gg 1 \times 10^{14}\,\mathrm{W/cm^2}$), we can approximate the Lagrangian $L = T$, since $T \propto U_p \gg V \propto I_p$, which gives :

$$S = \frac{(-eE_o)^2}{2m_e\omega_1^2} \int_{t_o}^{t_r} (\sin(\omega_1 t) - \sin(\omega_1 t_o))^2 dt \tag{6}$$

The phase shift is then calculated with:

$$\Phi_{\text{dipole}} = -\frac{S}{\hbar} = \alpha I_o \tag{7}$$

With the following definitions

$$f(t_o, t_r) = 2\omega_1 \int_{t_o}^{t_r} (\sin(\omega_1 t) - \sin(\omega_1 t_o))^2 dt$$
$$U_p = \frac{(-eE_o)^2}{4m_e\omega_1^2} = \frac{(-e)^2}{2m_e\omega_1^2}\eta_o I_o \tag{8}$$
$$\alpha = \frac{f_o(t_o, t_r)}{\hbar\omega_1}U_p$$

This classical model gives $\alpha \approx 1 - 5 \times 10^{-14}\,\mathrm{cm^2/W}$ for short trajectory electrons and $\alpha \approx 20 - 25 \times 10^{-14}\,\mathrm{cm^2/W}$ for long trajectory electrons. It is in good agreement with quantum calculations [9, 10, 11]. Also, even for lower intensity ($I \ll 1 \times 10^{14}\,\mathrm{W/cm^2}$) where the potential V can no longer be neglected on the Lagrangian calculation, it still accurate gives results.

I.2   Pressure and Absorption

I.2.1   The density profile

The pressure $P(z,r)$ in cylindrical coordinate is usually modeled either with a square profile or a gaussian profile depending on the experimental system we are using. For a nozzle of diameter l_p, and a nozzle outlet position $(z_{\text{noz}}, r_{\text{noz}})$, with $r \geq r_{\text{noz}}$ we have:

- *Gaussian*: if we use a basic end-fire nozzle (Fig.7a) with a diameter lp, the density profile can be reasonably modeled by a two-dimension Gaussian function [9, 12, 13] (C.1):

$$P(z,r) = P_m \exp\left(-\frac{(z - z_{\text{noz}})^2}{2\sigma_z^2}\right) \exp\left(-\frac{(r - r_{\text{noz}})^2}{2\sigma_r^2}\right), \quad \sigma_z = \frac{lp}{2\sqrt{2\ln(2)}} \quad (9)$$

- *Square*: If we use a dynamic nozzle (Fig.7b), then the density can be modeled by a square - gaussian density profile of length l_p/m (IV.4.2), where m is an experimentally tunable parameter.

$$P(r,z) = P_m \exp\left(-\frac{(r - r_{\text{noz}})^2}{2\sigma_r^2}\right) \times \left(|z| \leq \frac{l_p}{2m}\right) \quad + \quad 0 \times \left(|z| > \frac{l_p}{2m}\right) \quad (10)$$

The diameter σ_r is due to the high pressure gradient between the gas jet output and the vacuum chamber, its value has been simulated around $\sigma_r = 120\,\mu\text{m}$ [12] for $l_p = 150\,\mu\text{m}$, but it strongly depends on the nozzle diameter. More details on end-fire nozzle properties can be found in [13].

As there is a strong asymmetry between $r > 0$ and $r < 0$ in the pressure profile, we consider in our simulations that $P(-r, z) = P(r, z)$ to make calculations simpler.
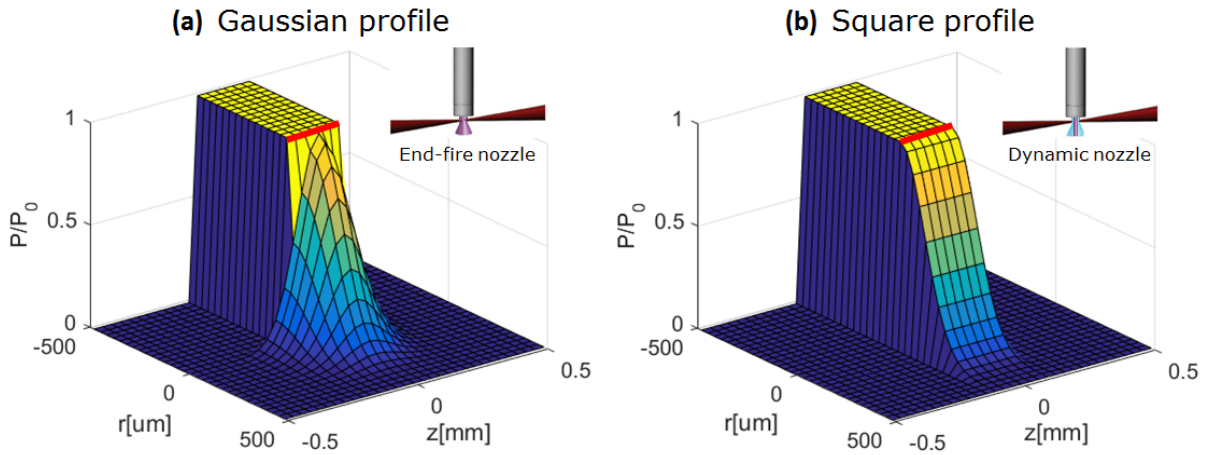
Figure 7: (a)Gaussian and (b)square density profile, with a medium length $l_p = 200\,\mu\text{m}$, $m = 1$. The red line represent the nozzle outlet positon.

I.2.2   Absorption & Beer-Lambert's law

We now consider the light absorption on the axis z, which is propagation direction of our laser beam.

The Beer-Lambert's law

When light go through a medium, The intensity fall off exponentially in the medium with an assumed constant decay following the Beer's law [9]:

$$I(z) = I_o \exp\left(-\frac{\alpha}{2}z\right) \tag{11}$$

The absorption coefficient α an be calculated from the extinction coefficient κ (imaginary part of the refractive index) following:

$$\alpha = \frac{4\pi\kappa}{\lambda} \tag{12}$$

However κ scale inversely with pressure, so it is common in literature to talk about the absorption cross section σ, which is only wavelength dependant.

$$\sigma = \frac{\alpha}{\rho} \tag{13}$$

We also often talk about the absorption length L_{abs}, which correspond to the length when 63% of intensity has been absorbed:

$$L_{abs} = \frac{2}{\alpha} = \frac{2}{\sigma\rho} \tag{14}$$

Difference between square and gaussian profile

As the pressure along z is not always constant and because α is pressure dependent, The Beer's law is no longer true, and we have to write the differential equation for a more accurate understanding:

$$\frac{\partial I}{\partial z} = -\frac{\rho(z)\sigma}{2}I(z) \tag{15}$$

The atomic density $\rho(z)$ is directly related to the pressure $P(z)$ by the perfect gas law : $P(z) = \rho(z)k_B T$.

For the same medium length, we plot the output Intensity for square and Gaussian density profile. And from the figure we note that the square and gaussian density profile leads to nearly the same final intensity.
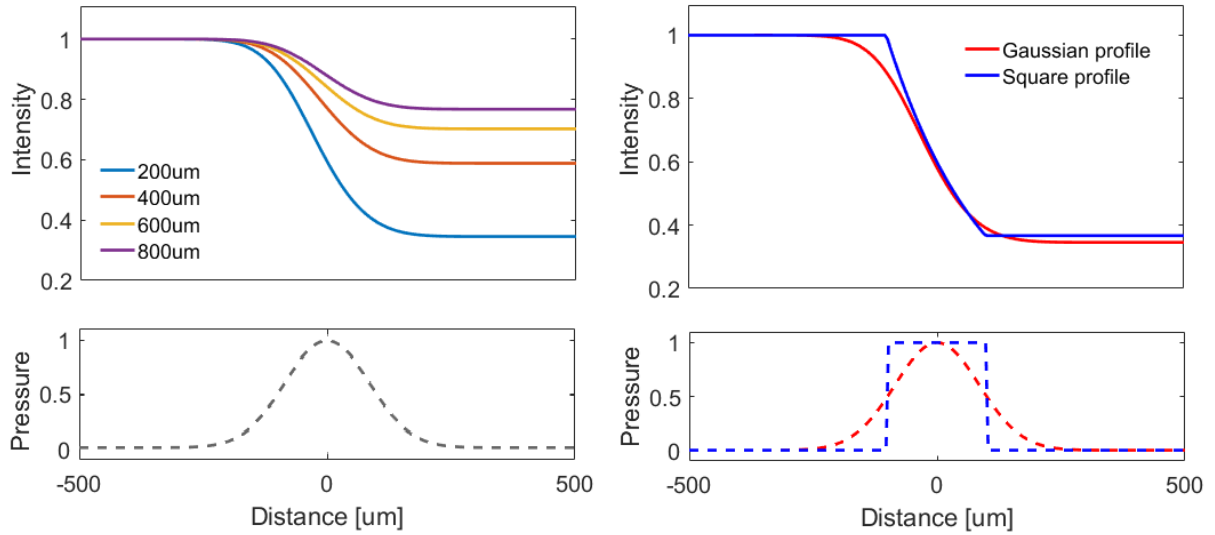
Figure 8: (a) Intensity evolution for different absorption length with a Gaussian density profile. (b) Absorption for a square and Gaussian density profile with $L_{abs} = 200\,\mu\text{m}$.

Wavelength dependence

It has been suggested by Rayleigh that the absorption cross section vary with the wavelength λ following [14]:

$$\sigma \propto \frac{1}{\lambda^4} \tag{16}$$

Measurements taken in [15, 16] are plotted Fig.9. Even though we notice strong variations, the overall absorption is in good agreement with the Rayleigh absorption. Note that because of experimental problem, no measurement has been done for energy lower that $14\,\text{eV}$ (ionization potential of Krypton)
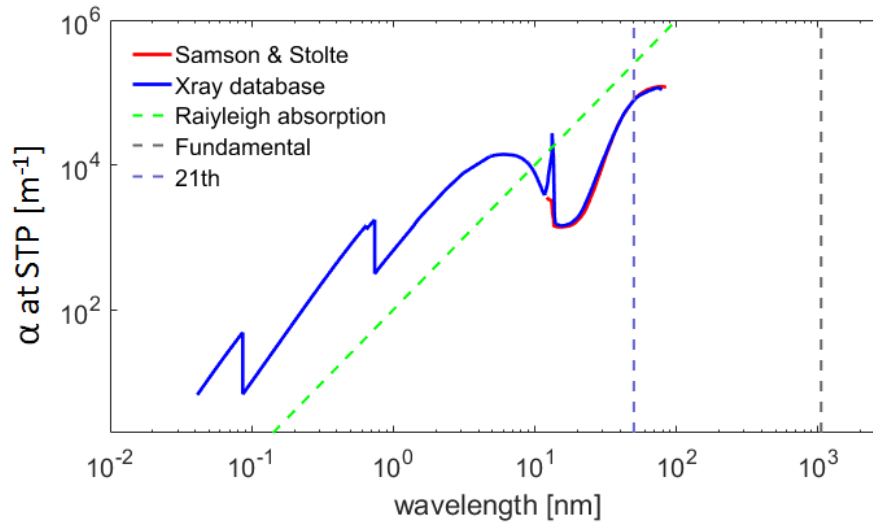
Figure 9: Absorption coefficient of Krypton at STP, $\lambda = 1050\,\text{nm}$, calculated from refractive index Xray data base [15] and cross section measurement [16].

I.3   Gaussian beam

A Gaussian beam is a solution of the paraxial wave equation, and is a beam of monochromatic electromagnetic radiation whose electric field amplitude profiles are given by a Gaussian function. It gives a good description of most laser beams.

I.3.1   Gaussian beam function

The basic formula of the Gaussian beam electric field with a propagating wavelength λ in free space is:

$$E(z,r) = E_o \frac{\omega_o}{\omega(z)} \exp\left(-\frac{r^2}{\omega^2(z)}\right) \exp\left(-i(k_o z + k_o \frac{r^2}{2R(z)} - \zeta(z))\right) \hat{x} \tag{17}$$

With: $\omega(z) = \omega_o \left(1 + \frac{z}{z_R}\right)$ the position dependent radius,

$R(z) = z \left(1 + \left(\frac{z_R}{z}\right)^2\right)$ the wavefront curvature,

and $\zeta(z) = \arctan\left(\frac{z}{z_R}\right)$ the Gouy phase.

$k_o = \frac{2\pi}{\lambda}$ is the wave-vector number, ω_o the $1/e^2$ beam radius, and $z_R = \frac{\pi \omega_o^2}{\lambda}$ denotes the Rayleigh range. Here, the electric field is polarized in the x direction, and propagating in the z direction.
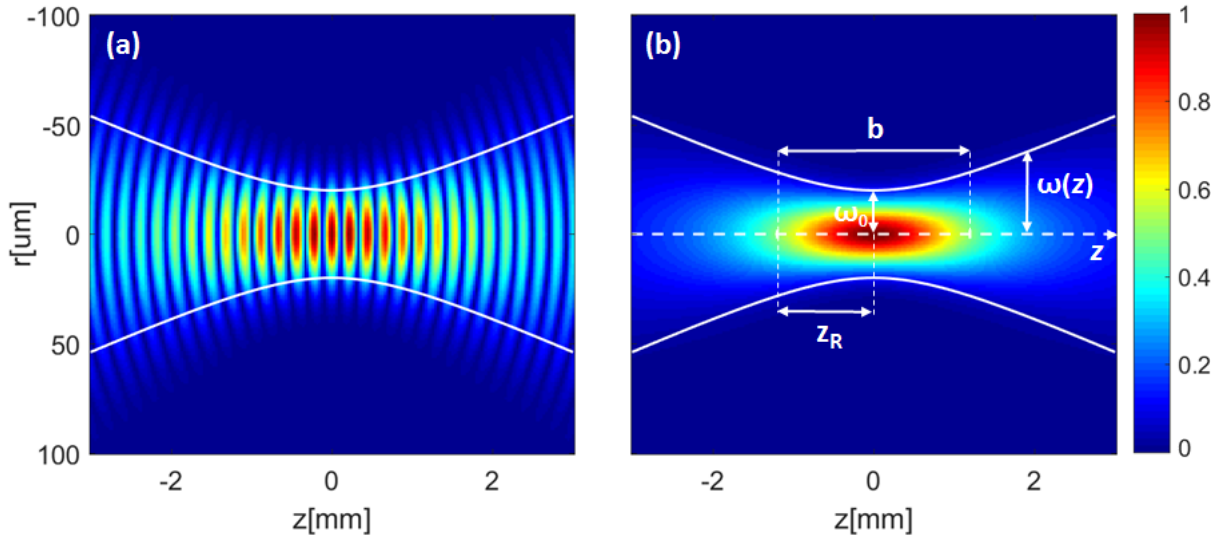
Figure 10: Gaussian beam with radius $20\,\mu\mathrm{m}$ and wavelength $1050\,\mathrm{nm}$. (a) The electric field $|E(z,r)|$ and (b) the intensity $I(z,r)$ are plotted along axis z and r.

The intensity of the beam is given by $I(z,r) = \frac{|E(z,r)^2|}{2\eta_o}$, and if we add the pulse profile (t_p being the FWHM of the laser pulse), the equation becomes:

$$I(z,r,t) = I_o \left(\frac{\omega_o}{\omega(z)} \right)^2 \exp \left(-\frac{2r^2}{\omega^2(z)} \right) \exp \left(-2\ln(2) \left(\frac{t}{t_p} \right)^2 \right) \tag{18}$$

I.3.2   The phase of a Gaussian beam

The gaussian beam acquires a phase as it propagates, and this is given by the second exponential term in Eq. 17 :

$$\phi(z,r) = k_o z + k_o \frac{r^2}{2R(z)} - \zeta(z) \tag{19}$$

The first term corresponds to the phase shift of a plane wave, the second term adds the effect of the curvature of the wavefront, and the third term is the Gouy phase. When computing the phase of a Gaussian beam, it is also possible to use the following expression, $b = 2z_R$ being the confocal parameter [17]:

$$\phi(z,r) = k_o z + \arg \left[\frac{1}{b + 2iz} \exp \left(-\frac{kr^2}{b + 2iz} \right) \right] \tag{20}$$

It is important to note that, depending on where in the focus the HHG occurs, the phase will not be the same. It is also useful to look at the wave vector $\vec{k} = \vec{\nabla}\phi$ and the wave vector mismatch due to the focus $\Delta k_{\text{foc}} = k_o - |\vec{k}|$ (see III.2.1).
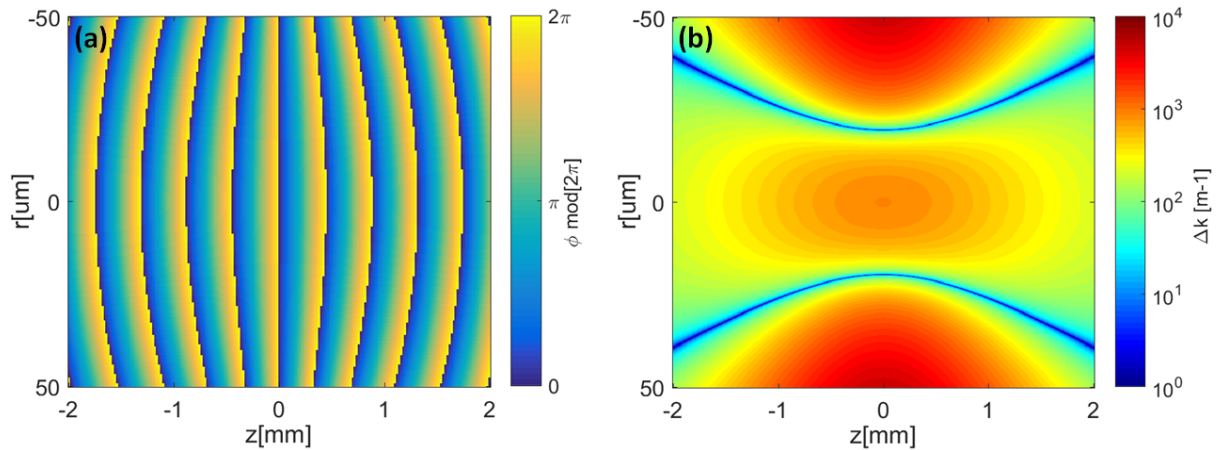
Figure 11: Gaussian beam with radius $20\,\mu\text{m}$ and wavelength $1050\,\text{nm}$. (a)The phase and the (b)wavevector mismatch Δk_{foc} are plotted along axis z and r.

I.4   Refractive index

I.4.1   Wavelength dependence

Sellmeier equation

For any given material, the refractive index is not a constant with respect to wavelength, and it has been demonstrated with the dipole oscillator model of the atom [14] that materials has resonances (Fig.12). The refractive index may have multiple resonances across the vibrational and optical frequency range, and experimentally, we can model this for different materials using the Sellmeier equation, which gives:

$$n(\lambda) - 1 = \sum_{i=1}^{r} \frac{B_i}{C_i - \lambda^{-2}} \tag{21}$$

Where r is the number of resonances, and B_i and C_i are experimentally determined parameters. Argon, Krypton and Xenon have 3 resonances, their Sellmeier constant at STP are given in Table.2.
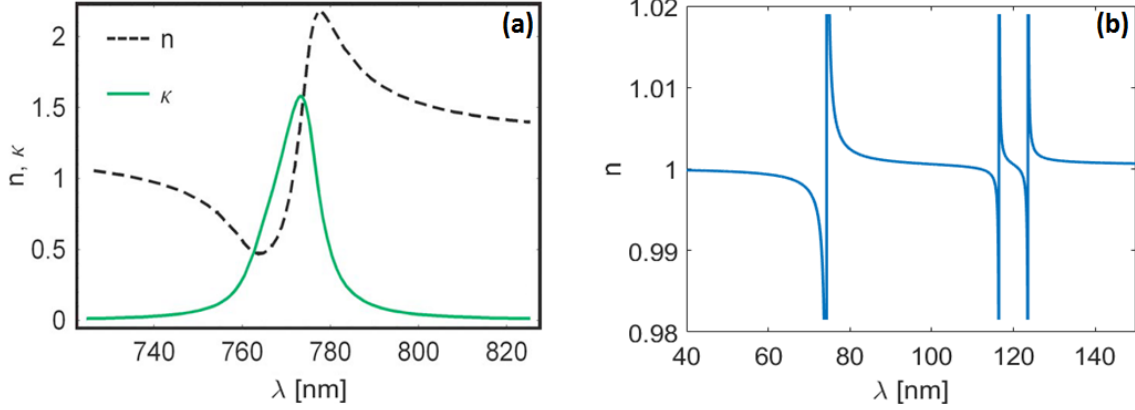
Figure 12: (a) Example of the Real and imaginary parts (n and κ, respectively) of the complex index of refraction near resonance, obtained from the classic electron oscillator model of the dielectric constant [18]. (b) Refractive index as a function of wavelength for Krypton using Sellmeier equation.

It is useful for us to have Eq.55 in terms of ω. And to match our references we will relabel this difference from unity, $n(\omega) - 1$ as $\delta(\omega)$. So then:

$$\delta(\omega) = \sum_{i=1}^{3} \frac{B_i}{C_i - (\frac{\omega}{2\pi c})^2} \tag{22}$$

Gas	$B_i[\text{um}^{-2} \times 10^3]$			$C_i[\text{um}^{-2}]$		
	B_1	B_2	B_3	C_1	C_2	C_3
Argon	2.5	0.50	52	91	88	214
Krypton	2.5	2.7	62	65	74	182
Xenon	3.2	3.6	61	46	51	113

Table 2: Sellmeier parameter of Argon, Krypton and Xenon at STP, from [19].

Scaling with pressure

The refractive index scales linearly with pressure, so the index can be scaled by $P(z,r)/P_{atm}$, and we can write the neutral gas contribution to the refractive index:

$$\delta_{\text{neutral}}(z,r,t,\omega) \approx \frac{P(z,r)}{P_{atm}}\delta(\omega)\left(1 - \eta(z,r,t)\right) \tag{23}$$

$\delta(\omega)$ is the difference from unity of the refractive index at STP (given by Sellmeier equation). $\eta(z,r,t)$ is the ionization fraction, it does change within the pulse duration of the laser, and decays between laser pulses.

I.4.2 Plasma contribution

The refractive index of plasma can be treated even more simply than the dipole oscillator model of neutral atoms. It is identical, with the exception that there is no restoring force, as the electron is free, and consequently there are no resonances. The index is given by the well known equation

$$n(\omega) = \sqrt{1 - \frac{\omega_p^2}{\omega^2}} \approx 1 - \frac{\omega_p^2}{2\omega^2} \tag{24}$$

Where $\omega_p = \sqrt{\frac{N_e e^2}{m_e \varepsilon_o}}$ is defined as the plasma frequency. Note that since we are using a gas jet, then the number density of electrons N_e is not constant throughout, and also vary with time, so we need to scale it as follows:

$$N_e(z,r,t) = \eta(z,r,t)N_{\text{atm}}\frac{P(z,r)}{P_{\text{atm}}} \tag{25}$$

The difference from unity contribution to the refractive index from plasma is then [20]:

$$\delta_{\text{plasma}}(z,r,t,\omega) \approx -\frac{P(z,r)}{P_{atm}}\eta(z,r,t)\frac{N_{atm}e^2}{2\omega^2 m_e \varepsilon_o} \tag{26}$$

We can now write the final refractive index:

$$\begin{aligned} n(z,r,t,\omega) &= 1 + \delta_{\text{neutral}} + \delta_{\text{plasma}} \\ &= 1 + \frac{P(z,r)}{P_{atm}}\left(\left(1 - \eta(z,r,t)\right)\delta(\omega) - \eta(z,r,t)\frac{N_{atm}e^2}{2\omega^2 m_e \varepsilon_o}\right) \end{aligned} \tag{27}$$

To model phase matching, the ionization fraction is thus far an undetermined variable, and it is to this that we turn our attention.

II Ions and atoms dynamic

II.1 Tunnel ionization process

In classical ionization, an electron must have enough energy, so called ionization potential I_p, to make it over the potential barrier. This can be understood as a process by which a bound electron, through the absorption of more than one photon from the laser field, is ionized ; this picture is generally known as multiphoton ionization (MPI). But quantum tunneling also allows the electron simply to go through the potential barrier instead of going all the way over it (cf Fig.13).
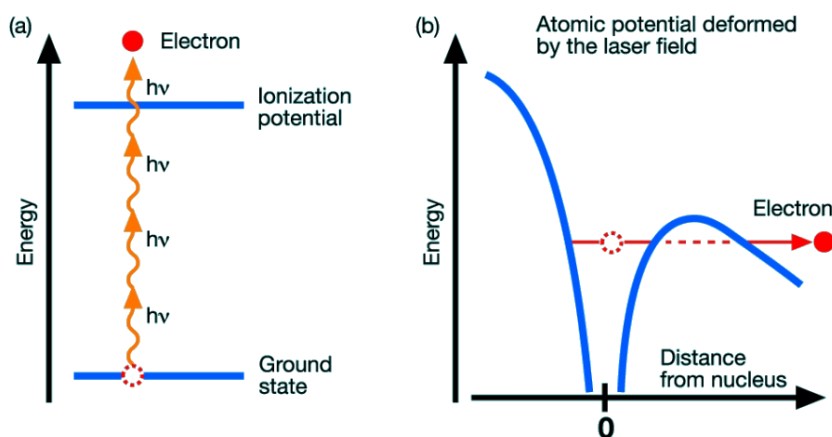
Figure 13: (a) MPI, in classical ionization, the electron needs an energy I_p to be freed. (b) The electron is bound by the Coulomb potential of an atom, an incoming intense laser field distorts the potential and allows the tunneling of the electron through the Coulomb barrier. Adapted from [21].

In the context of a chemical reaction, the creation of ions from atoms A is given by:

$$A + N\hbar\omega \rightarrow A^+ + e^- \tag{28}$$
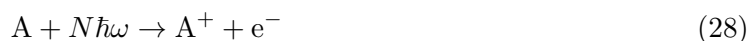
The Keldysh parameter γ determines whether multiphoton or tunneling ionization dominates the nonlinear ionization processes. For $\gamma \gg 1$, multiphoton ionization dominates, whereas for $\gamma \ll 1$ tunneling ionization takes over.

$$\gamma = \sqrt{\frac{I_p}{2U_p}} \tag{29}$$

We are working with gaussian laser pulses given by an electric field of amplitude E_o, and envelope $f(t)$, which is slowly varying on time scales of the tunneling ionization.

$$\vec{E}(t) = \vec{E}_o f(t) \cos(\omega_1 t + \phi_o)$$
$$\text{with} \quad E_o f(t) = \sqrt{2\eta_o I(t)} \tag{30}$$

$I(t)$ is the instantaneous intensity experienced by the gas and η_o is the impedance of free space. The ponderomotive enery is proportional to the laser field intensity $U_p \propto I(t)$.

II.1.1   ADK and Yudin rate

Several models exist in literature to calculate the ionization rate of gases in laser fields. Traditionally, the ADK model [22] developed in the 1960s using quasistatic approximation was often used for describing tunneling ionization because of his mathematical simplicity. However, it is limited to the strong field regime and is only valid for $\gamma \ll 1$ which correspond in our work to intensities $I \gg 10^{14}$.

The ADK-theory after Coulomb correction yield the following expression [23]:

$$W_{\text{ADK}} = A_{n^*}\omega_p \left(\frac{4\omega_p}{\omega_t}\right)^{2n^*-1} \exp\left(-\frac{4\omega_p}{3\omega_t}\right) \tag{31}$$

with the definitions

$$\omega_p = \frac{I_p}{\hbar} \qquad\qquad \omega_t = \frac{eE(t)}{\sqrt{2m_e I_p}}$$

$$n^* = Z\sqrt{\frac{I_{ph}}{I_p}} \qquad\qquad A_{n^*} = \frac{2^{2n^*}}{n^*\Gamma(n^*+1)\Gamma(n^*)} \tag{32}$$

While this may be useful for an approximate calculation, the intensity of the fundamental in the HHG process varies with time, and thus for an accurate description of ionization rate we look into the Yudin rate [24], which also consider MPI, and is valid for any γ regime.

$$W_{\text{Yudin}} = N(t) \exp\left(-\frac{2\eta_o e^2}{\hbar m_e}\frac{I(t)}{\omega_1^3}\phi(t)\right) \tag{33}$$

With the following definitions:

$$\phi(t) = (\gamma^2 + \sin^2(\omega_1 t) + \frac{1}{2})\ln(c) - \frac{3\sqrt{b-a}}{2\sqrt{2}}\sin|\omega_1 t| - \gamma\frac{\sqrt{b+a}}{2\sqrt{2}}$$

$$a = 1 + \gamma^2 - \sin^2(\omega_1 t)$$

$$b = \sqrt{a^2 + 4\gamma^2 \sin^2(\omega_1 t)} \tag{34}$$

$$c = \left[\left(\sqrt{\frac{b+a}{2}} + \gamma\right)^2 + \left(\sqrt{\frac{b-a}{2}}\sin(\omega_1 t)\right)^2\right]^{\frac{1}{2}}$$

The pre-factor to the exponential $N(t)$ is based on matrix-element calculations for the tunneling and MPI. The equation derived from [24] reads:

$$N(t) = A_{n^*} \sqrt{\frac{3\kappa}{\gamma^3}} C \frac{I_p}{\hbar} \left(\frac{4I_p}{\hbar e} \sqrt{\frac{m_e I_p}{\eta_o I(t)}} \right)^{2n^* - 1}$$

$$\text{where} \quad \kappa = \ln(\gamma + \sqrt{\gamma^2 + 1}) - \frac{\gamma}{\sqrt{\gamma^2 + 1}}$$

(35)

C is the Perelomov-Popov-Terent'ev correction [25]. In the high intensity regime $\gamma \ll 1$, $C \approx 1$, and in the low intensity regime, where $\gamma \gg 1$, this factor is approximately $C \approx \frac{1.2}{\sqrt{\gamma}}$. The Figure 14 highlight the differences between the ADK and Yudin rate.
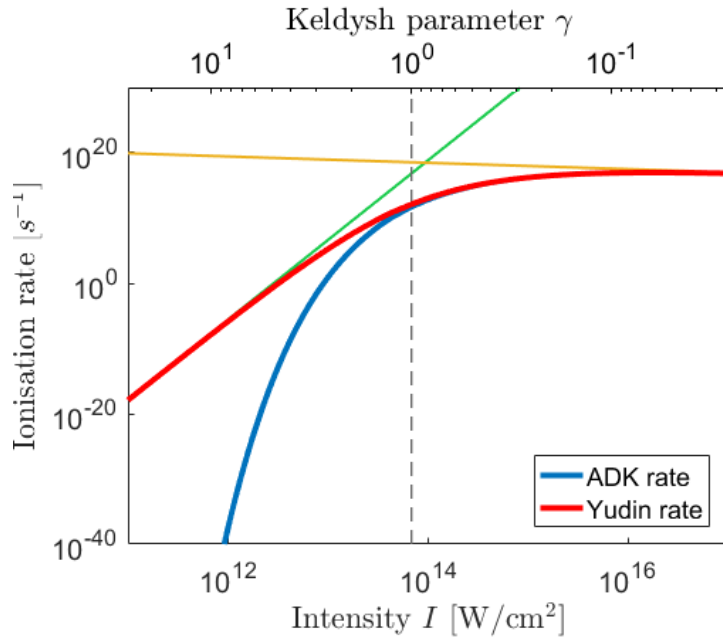
Figure 14: Ionization rate of Krypton at $t = 0$, with a $1050\,\text{nm}$ laser. The Yudin model bridges the perturbative regime with the high intensity regime, ADK and Yudin rate are the same For $I > 1e14$. The dashed line correspond to $\gamma = 1$.

II.1.2   Ionization evolution during a pulse

Having calculated the ionization rate, the fraction of ionized atoms during the duration of a pulse can be obtained simply by integrating over the gaussian intensity profile in time:

$$\eta(t) = 1 - \exp\left(-\int_{-\infty}^{t} W_{\text{Yudin}}(t)dt \right)$$

(36)

The ionization fraction as a function of time, plotted alongside the pulse duration, is given in Figure 15. Unsurprisingly, the ionization fraction increases with both intensity and pulse duration. For Krypton, with a pulse duration of $t_p = 130\,\text{fs}$, the ionization fraction reaches unity at approximately $2.1 \times 10^{14}\,\text{W/cm}^2$.
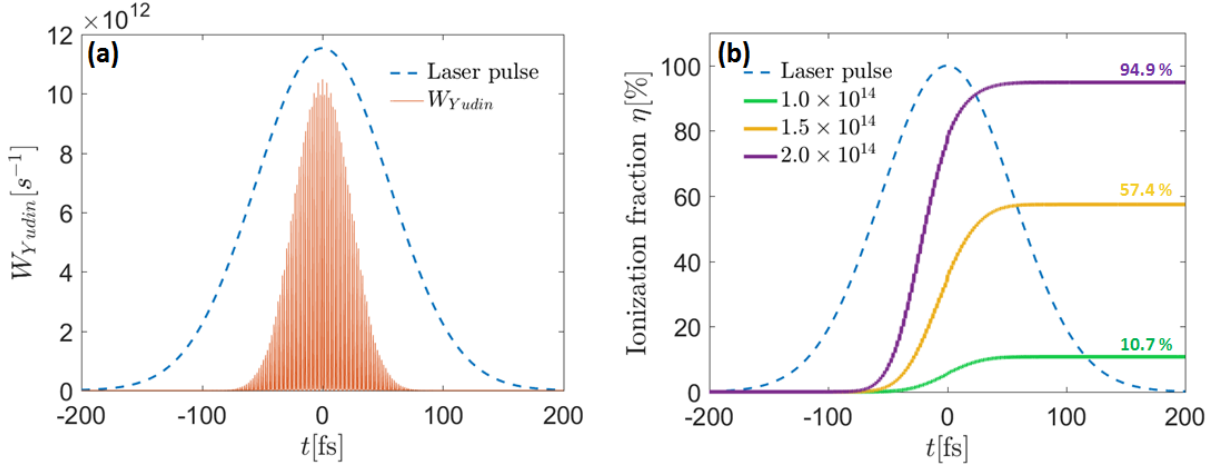
Figure 15: (a) Ionization rate as a function of time for $I_o = 2 \times 10^{14}\,\mathrm{W/cm^2}$. (b) Ionization fraction evolution through the duration of a pulse. The fraction of ionized atoms per pulse scales quickly with intensity up to unity. Krypton, $t_p = 130\,\mathrm{fs}$.

II.2   Ions recombination and diffusion

Given atoms initially ionized by the driving field, only a fraction of the electron trajectories are used in the HHG process (B.3), returning the parent atom to a neutral state. And this leaves a population of ionized atoms and plasma. In low repetition rate systems ($f < 1\,\mathrm{MHz}$), all the ions have enough time to completely leave the interaction region between 2 pulses, so we simply consider each pulse independently. However in high repetition rate system like ours ($f = 60\,\mathrm{MHz}$), the exited ions will "see" more than one pulse as they move through the focus, and it is now important to study how the plasma population evolves between each pulse. There is two large effects which govern this evolution:

- *Recombination*: The population of ionized atoms is decaying over time and may recombine to an excited neutral state (II.2.1)

- *Diffusion*: Atoms and ions are ejected from the gas jet with a certain velocity (which depends on the gas) [9] and the plasma cloud also expand as it continues to move away from the focus (II.2.2).

A last thing to consider is that atoms that went through the recombination process remain in an excited state until the next pulse. Since an excited state has a lower ionization energy, its probability of being ionized on the next pulse is higher than the ground state. (II.2.3).

We will consider in our study that imbalances in the fluxes and densities between electrons and ions are negligible, thus the ion and electron density at a given position and time are always equal: $\rho_e = \rho_i = \rho$.

II.2.1   Three body recombination rate

There are many channels in which ionized Hydrogen-like atoms can return to a neutral state, each with their own rate that is determined by the environment [26] (see C.2 for more details). In our system, we have a high density of plasma and neutral atoms in the region, and in this regime it has been demonstrated that the three-body collisional recombination stabilized by an electron is the dominant process [9]: $A^+ + e + e \rightarrow A^* + e$

With the rate at electron temperature T_e given by [27]:

$$\Gamma_{\text{TBR},e^-} = \Gamma_o\rho^2 \qquad \text{with} \qquad \Gamma_o = 1.1 \times 10^{-20}\, T_e^{-9/2} \text{ m}^6/\text{s} \tag{37}$$

It has been demonstrated in [9] that the electron temperature for our system is around $T_e = 3\,\text{eV}$. The density of electrons is then given by:

$$\frac{\partial \rho}{\partial t} = \Gamma_{\text{TBR}}\rho = -\Gamma_o\rho^3 \tag{38}$$

This differential equation has an analytic solution:

$$\rho(t) = \left(2\Gamma_o t + \frac{1}{\rho_i^2}\right)^{-\frac{1}{2}} \qquad \rho_i = \eta_i \frac{P}{k_B T_0} \tag{39}$$

The initial electron density is calculated from the Yudin ionization fraction $\eta_i = \eta(\infty)$ in Eq.36. We also define the plasma half-lifetime $t_{1/2}$ (which is the time when half of the plasma has decayed):

$$t_{1/2} = \frac{3}{2\Gamma_o\rho_i^2} \tag{40}$$

The time evolution of the ionization fraction for different η_i, and the pressure dependence on the plasma lifetime is plotted Fig.18.
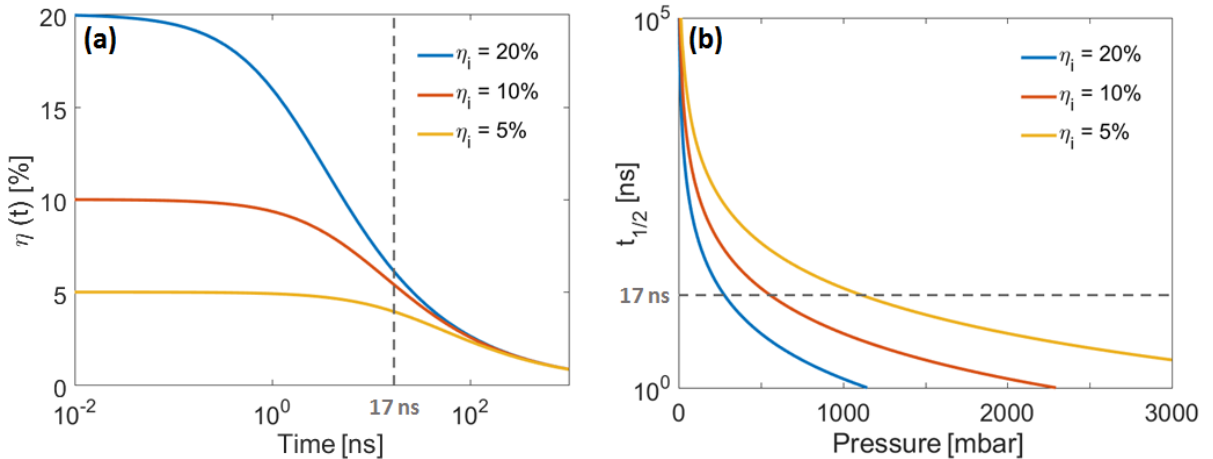
Figure 16: (a) Time evolution of the ionization fraction for $P = 500\,\text{mbar}$ and (b) Pressure dependence of the three-body recombination half time for different η_i.

These figures emphasise how important the initial conditions are on the plasma decay : For a high η_i at $P = 500\,\text{mbar}$, more than half of the ions returned to the neutral state, whereas it's nearly none for a low η_i. Similarly, the pressure has a strong impact on the recombination.

II.2.2   Ambipolar diffusion

The electrons that have sufficient energy to leave the focus will leave behind a positive charge density of ions and create a charge gradient in the plasma. The electric field that results will then draws the ions away from the focus and the net result is that both ions and electrons will stream outward at the same speed (Fig.17).
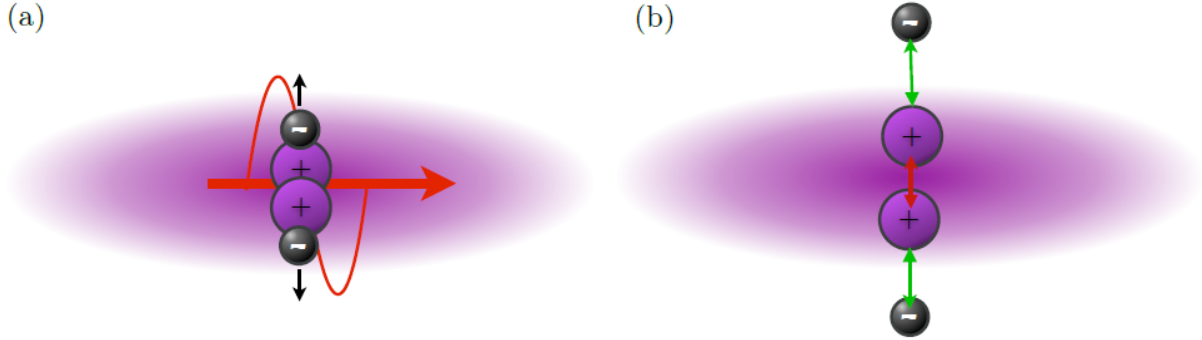
Figure 17: (a) The electric field (red arrow) ionizes the atoms, allowing the energetic electrons to leave the focus while the ions remain. (b) The resulting electric field from the repulsion of the ions (red) and electron-ion attraction (green) moves the ions out of the focus. Taken from [9].

If we assume that imbalances in the fluxes and densities between electrons and ions are very small, we can write $\rho_i = \rho_e = \rho$, and the density then follow the diffusion equation [proof] (note that we are interested only in the diffusion on the r axis, since it's negligible on the z axis):

$$\frac{\partial \rho}{\partial t} = -D_\alpha \frac{\partial^2 \rho}{\partial r^2} \tag{41}$$

D_α is the ambipolar diffusion coefficient: $D_\alpha = D_i \left(1 + \frac{T_e}{T_i} \right)$

D_i is the ion diffusion coefficient in his parent gas (Einstein relation): $D_i = \dfrac{\mu_i k_B T_i}{e}$

μ_i is the ion mobility in his parent gas (scale inversely with P [28]): $\mu_i = \mu_i^0 \dfrac{P_{\text{atm}}}{P}$

So in the end we have :
$$D_\alpha = \frac{P_{\text{atm}}}{P} \left(\frac{k_B T_i \mu_i^0}{e} \right) \left(1 + \frac{T_e}{T_i} \right) \tag{42}$$

μ_i^0 is the mobility of ions in their parent gas at STP (Table 3). The ion temperature is taken as the room temperature $T_i = 293\,\text{K}$ and the electron temperature is taken as $T_e = 3\,\text{eV}$ [9].

Gas	Argon	Krypton	Xenon
μ_i^0 [m^2/Vs]	1.4×10^{-4}	1.0×10^{-4}	6×10^{-5}
ref.	[29]	[29, 30]	[28, 30]

Table 3: mobility if ions in their parent gas at STP

As we did for the recombination, we can define a diffusion half lifetime $t_{1/2}$, which correspond to the time when the ionization fraction at the focus decreased by a factor of two. Unlike the recombination, the diffusion doesn't depends on the initial ionization fraction, but does depends on the gas.
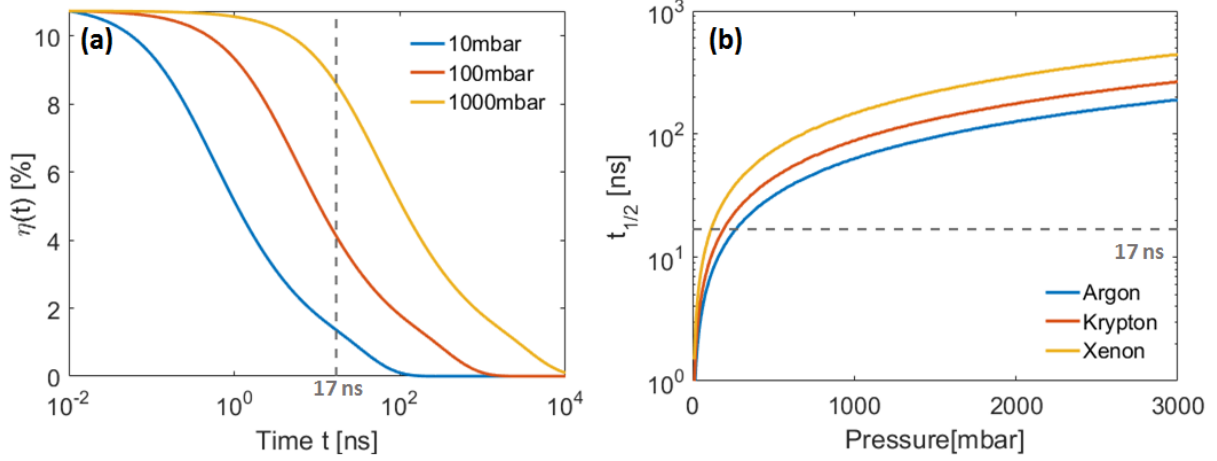
Figure 18: (a) Time evolution of the ionization fraction at the focus for different pressure in Krypton and (b) Diffusion half time as a function of pressure for different gas.

It is now clear that for low pressure, the diffusion will dominate the plasma dynamic, whereas for high pressure, it will be determined by the recombination ($t_{1/2} < 17ns$).

II.2.3   Metastables atoms dynamic

Now that we have studied the ions A^+ behavior, we know that some of them will recombine into excited neutral atoms A^*. However metastable atoms may also decay into lower energy states. In this section we summarize the behavior of the metastable atoms in our system, a detailed study is presented in C.2.

Recombination and diffusion

The timescale of the recombination of metastable hydrogen-like atoms is in the order of $100\,\text{ns} - 1\,\text{µs}$ [31, 32, 33], which is much higher than the time between 2 pulses ($17\,\text{ns}$). Also, as metastable atoms are neutral, they are not attracted away by electrons, so they diffuse very slowly and its negligible.

Ionization of metastable atom

The ionization potentials of excited states are much lower than the one of the ground state (around $I_p = 4\,\text{eV}$ for the less energetic metastable atoms [34]), which makes them very likely to ionize. Calculation with the Yudin rate (II.1.1) show that the ionization probability on the next pulse is 1. thus for our study we will consider that all of the metastable atoms are ionized on each pulse, even if they are far from the focus.

II.2.4   Final ion density

To describe the evolution of the plasma cloud, we simply merge the two differential equations studied before:

$$\frac{\partial \rho}{\partial t} = -\Gamma_o \rho^3 - D_\alpha \frac{\partial^2 \rho}{\partial r^2} \tag{43}$$

Once we know $\rho(t)$, the metastable atoms density $\rho_*(t)$ is calculated with:

$$\rho_*(t) = \Gamma_o \int_0^t \rho(t)^3 dt \tag{44}$$

The Figure.19 is an example of the ions and metastable atoms density time evolution with an initial single pulsed ionized gas (which can be considered gaussian for $I_o < 1.7 \times 10^{14} \, \text{W/cm}^2$). To emphasize both diffusion and recombination, we take a low pressure (fast diffusion) and a high intensity (fast recombination) : $I = 1.65 \times 10^{14} \, \text{W/cm}^2$ and $P = 60 \, \text{mbar}$, the initial ionization fraction after one pulse at the focus is $\eta = 73\,\%$.
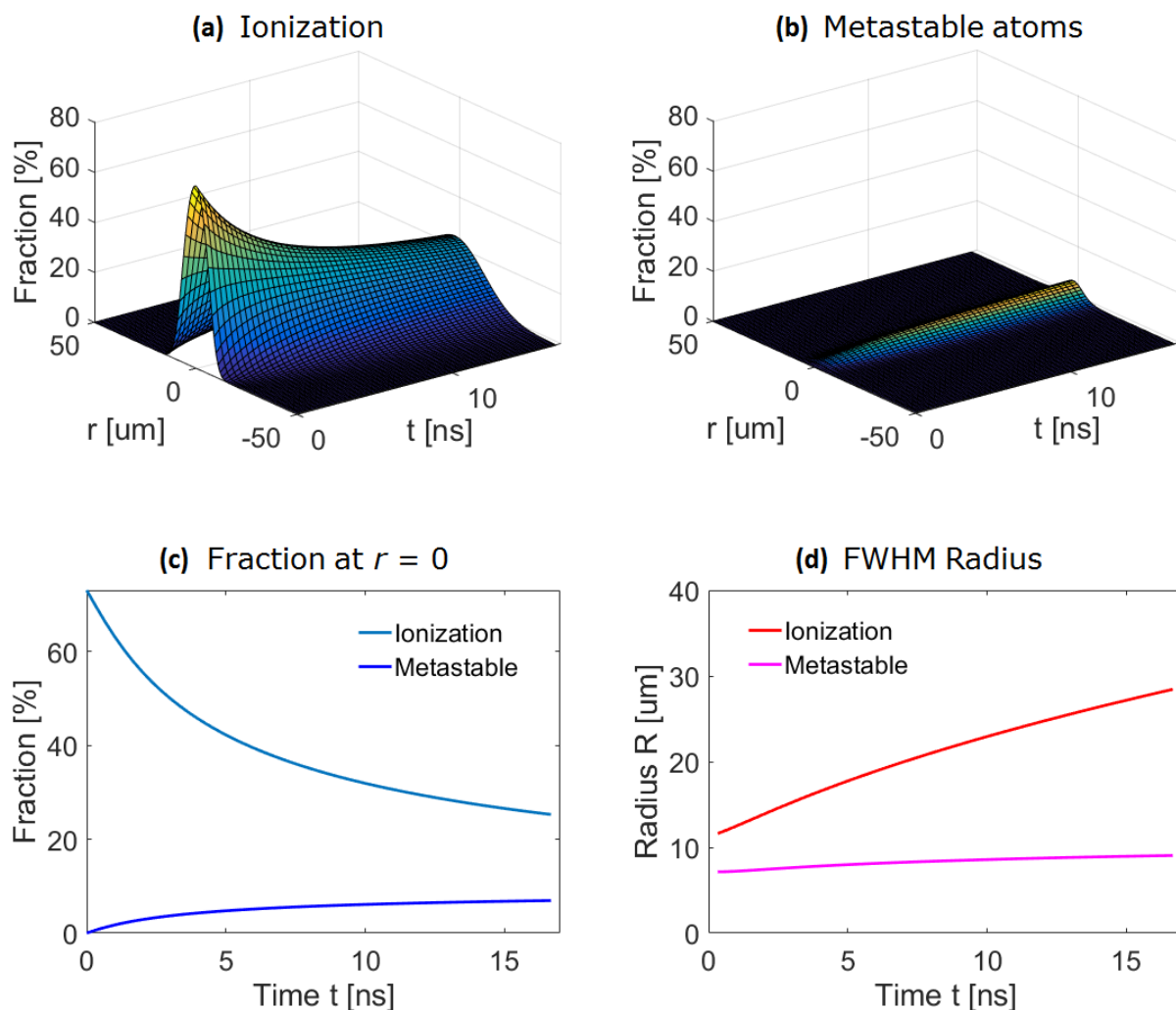

Figure 19: (a)Ionization fraction and (b)Metastable atoms fraction as a function of time between the first and the second pulse, the ionization and metastable atoms (c) fraction at the focus and (d) FWHM are also plotted. $I = 1.65 \times 10^{14} \, \text{W/cm}^2$ and $P = 60 \, \text{mbar}$.

II.3 Ionization of multiple pulsed gas

II.3.1 Gas velocity and pressure

Because a high gas velocity in the focus area will remove the ions quicker than a low gas velocity, and thus lead to a lower ionization fraction, it is crucial to study the gas velocity at the outlet of the nozzle. A typical nozzle shape used in HHG experiment is shown Fig.20, from the figure we can already see that the backing pressure P_o is not the same as the pressure at the outlet P^*.
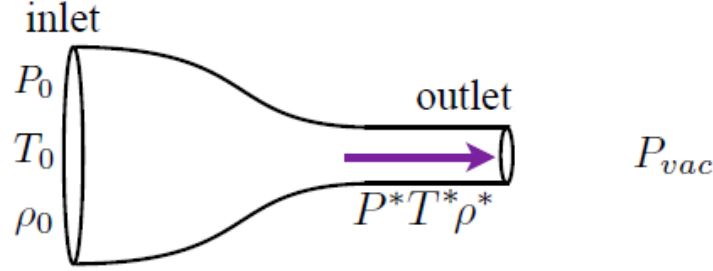
Figure 20: Typical nozzle shape used in HHG experiment. Taken from [9].

The backing pressure $P_0 \approx 1\,\mathrm{bar}$ being much higher than the pressure in the chamber $P_{\mathrm{vac}} \approx 1 \times 10^{-5}\,\mathrm{bar}$, the gas velocity on the outlet is the speed of sound in the gas [9] (the speed of sound in an ideal gas depends only on its temperature and composition):

$$V_s = \gamma R_s T^* \tag{45}$$

T^* is the temperature of the gas at the outlet.
$\gamma = c_p/c_v$ is the Laplace constant of the gas.
$R_s = R/M = c_p - c_v$ is the ideal gas constant R divided by the molar mass of the gas M.
c_p is the specific heat capacity at constant pressure of the gas.
c_v is the specific heat capacity at constant volume of the gas.

The speed of the gas can also be written [9]:

$$V_s = \sqrt{2c_p(T_0 - T^*)} \tag{46}$$

from Eq.45 and 46 we can deduce the temperature and the pressure at the outlet:

$$T^* = T_0\frac{2}{\gamma + 1} \qquad P^* = P_0 \left(\frac{T^*}{T_0}\right)^{\frac{\gamma}{\gamma - 1}} \tag{47}$$

The calculation gives $T^* = 0.75 \times T_0$ and $P^* = 0.49 \times P_0$ for noble gases. It means that the backing pressure that we are able to experimentally measure is not the same as the actual pressure used in the HHG process.
Table 4 gives the calculated speed of sound for different gas.

Gas	Helium	Argon	Krypton	Xenon
γ at $20\,°\text{C}$	1.66	1.67	1.68	1.66
c_p $[\text{J}\,\text{g}^{-1}\,\text{K}^{-1}]$	5.2	0.52	0.25	0.16
V_s $[\text{m}\,\text{s}^{-1}]$	880	280	194	153

Table 4: Laplace constant γ, heat capacity c_p and sound velocity V_s of noble gases.

After the outlet

We just showed that the pressure after the outlet is two times smaller than the backing pressure P_o. However, because it is hard to experimentally place the nozzle outlet precisely at the focus $r = 0$ ($r_{\text{nozzle}} = -100 \pm 50\,\mu\text{m}$), the distance between the nozzle outlet and the laser focus may have strong consequences on the actual gas pressure P and gas velocity V used in the experiment. As we studied in I.2, the pressure drop with a gaussian profile after the outlet, and it is reasonable to predict $P_o = 2$ - $10 \times P$. Fluid flow simulations in [9] and C.1 also suggest that the gas velocity can increase up-to $V = 2V_s$ after the nozzle outlet.

II.3.2   Simulation result

Now that we know how atoms and ions evolve between each pulse, we can study the behavior of our system after several pulses. Fig.21 is a video showing the time evolution of the ionization fraction in the focus area. Every $17\,\text{ns}$, a new pulse arrive and ionizes more atoms. The gas velocity being around $V = 250\,\text{m/s}$ for Krypton, atoms will "see" about 8 pulses before they leave the focus area ($\pm\omega_o$). The interaction length is taken as $l_p = 500\,\mu\text{m}$ to make the figure clearer.
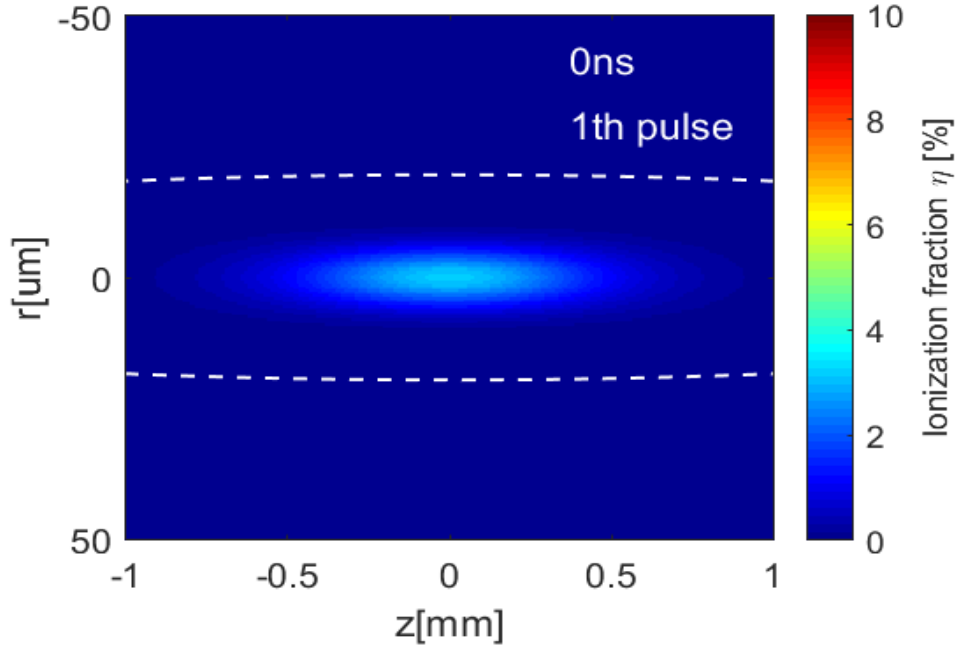

Figure 21: Ionization fraction evolving as a function of time for the first 20 pulses, the $1/e^2$ focus area is delimited by the dashed line. Krypton, $V = 250\,\text{m/s}$, $I_o = 8 \times 10^{13}\,\text{W/cm}^2$, $P_o = 500\,\text{mbar}$, $l_p = 500\,\mu\text{m}$, $f = 60\,\text{MHz}$.

In this calculation we do the assumption that the pressure $P(r, z)$ is not affected by the ions diffusion. Since we usually work with an ionization fraction lower than $10\,\%$, it is realistic.

In the plot we first notice that the diffusion is faster on the sides, it is because the pressure on the sides is lower than in the middle (gaussian density profile). Simulations show that the ionization fraction in the focus area always stabilise after the first pulsed atoms reach $\sim 2.5\omega_o$ ($50\,\mu$m in our case), we can then talk about the "final ionization fraction" η_f, defined as the ionization fraction just after a pulse when the loop state is reached. in our case, the gas velocity being around $V = 250\,\mathrm{m/s}$, the ionization fraction reach the loop state after 12 pulses. We now have the tools to study the behavior of our system for different gas pressure and gas velocity.

Pressure dependance

As studied in II.2.2, the diffusion coefficient scale inversely with pressure, which mean that increasing the pressure should lead to a higher resulting ionization fraction. The Fig.22 plot the final ionization fraction as a function of pressure for different gas velocity.
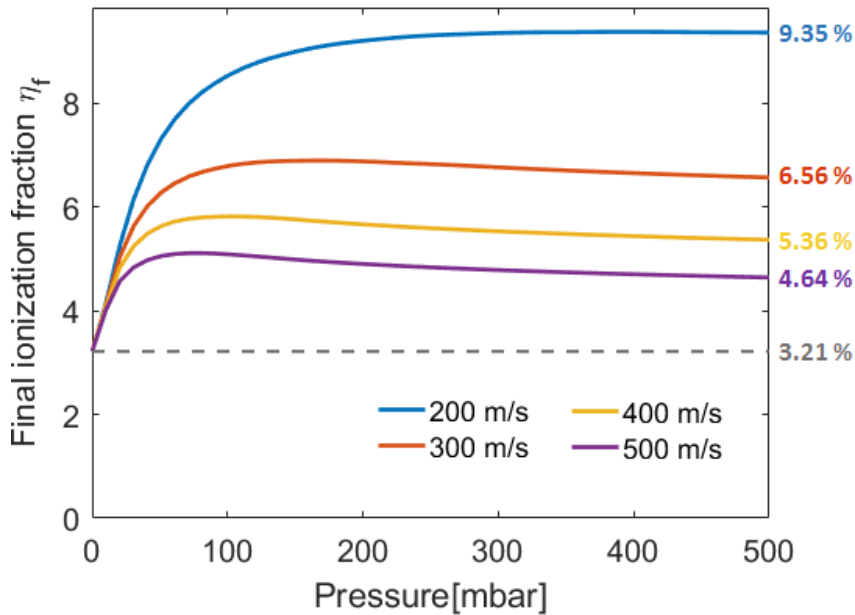
Figure 22: Ionization fraction after 16 pulses depending on pressure for different gas velocity. The peak intensity is $I_o = 8 \times 10^{13}\,\mathrm{W/cm^2}$ which correspond after a single pulse to $\eta = 3.21\,\%$ at the focus for Krypton.

From the figure we can see that, after a certain pressure, the ionization fraction always saturate to a limit ionization fraction η_{lim}. This is when the diffusion become negligible compared to the gas velocity, and it is important to note that η_{lim} strongly depends on the gas velocity V. We can see that the gas velocity doesn't have the same impact on the phase matching for different pressure. Indeed, for very low pressure, the final ionization fraction is the same for all gas velocity, but after $25\,\mathrm{mbar}$, it start splitting on the gas velocity play a more important role.

The importance of gas velocity

It is now clear that increasing gas velocity can significantly decrease the resulting ionization fraction (cf Fig.22). As the ionization fraction always saturate after a certain pressure, we can plot η_{lim} as a function of V.
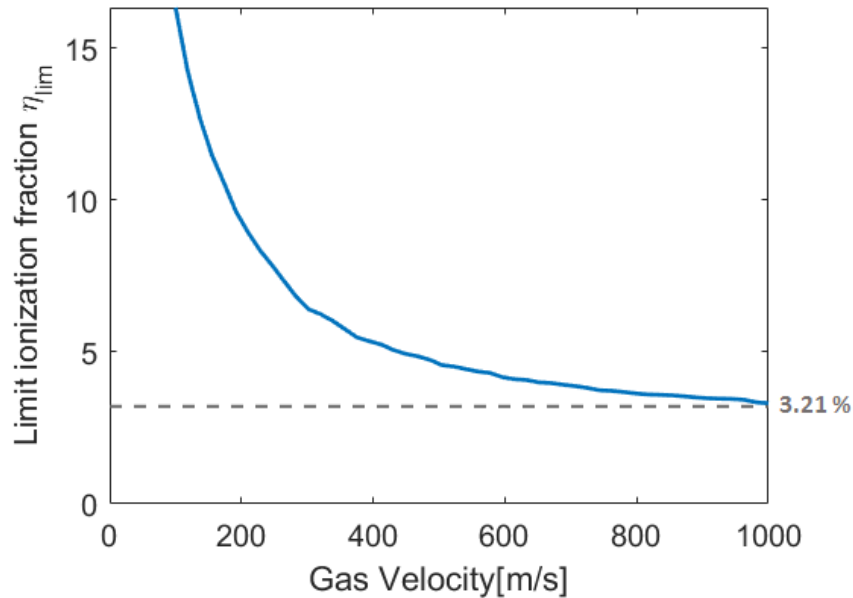
Figure 23: Limit ionization fraction as a function of gas velocity (the pressure is taken as 500mbar for the plot). The peak intensity is $I_o = 8 \times 10^{13}\,\text{W/cm}^2$ which correspond after a single pulse to $\eta = 3.21\,\%$ at the focus for Krypton.

This figure emphasize how changing the gas velocity can impact the phase matching. Increasing V from $200\,\text{m/s}$ to $400\,\text{m/s}$ decrease the ionization fraction by nearly a factor of 2, whereas increasing from $400\,\text{m/s}$ to $600\,\text{m/s}$ doesnt have a significant impact.

III   Harmonic amplitude calculation

It has been demonstrated from Maxwell equations that the on axis harmonic field amplitude can be calculated by solving the differential equation [9, 35]:

$$\frac{\partial E_o(z)}{\partial z} = -\frac{\rho(z)\sigma}{2}E_o(z) + i\frac{\mu_o c\omega_q}{2}A_q(z)\rho(z)[1 - \eta(z)]e^{i\Delta\phi(z)} \tag{48}$$

This differential equation is composed of two terms: the first one is the decaying due to absorption (see I.2.2) and the second term is the harmonic growing depending on the dipole response A_q and the phase matching $\Delta\phi$. The $[1 - \eta(z)]$ is added because only the neutral atoms participate to the harmonic generation.

III.1   Dipole response

In this section, we numerically solve the 1D time dependent Schrodinger equation (TDSE) to calculate the amplitude of the atomic response A_q.

Let's consider a ground state valence electron subjected to a potential $V = V_{\text{atom}} + V_{\text{field}}$:

- $V_{\text{field}}(x, t) = -exE_o f(t)\cos(\omega_1 t)$ is the oscillating potential of the driving field.

- $V_{\text{atom}}(x) = -\dfrac{1}{4\pi\varepsilon_o}\dfrac{e^2}{\sqrt{x^2 + X_o^2}}$ is the Coulomb potential of the atom.

X_o is the depth of the Coulomb potential (Table.5) and is defined as the position where the ground energy state $Eg = -Ip$. The ground state wave function is assumed to be [9]:

$$\psi(x, 0) = \frac{1}{\sqrt{2X_o}}\text{sech}\left(\frac{x}{X_o}\right) \tag{49}$$

Gas	Argon	Krypton	Xenon
X_o [au]	1.20	1.365	1.625
X_o [pm]	63.5	72.2	86.0

Table 5: Calculated potential depth of Argon, Krypton and Xenon, $\left(1\,\text{au} = 5.29 \times 10^{-11}\,\text{m}\right)$.

The electron wavefunction $\phi(x, t)$ evolution can be calculated solving the TDSE, $p = i\hbar\frac{\partial}{\partial x}$ being the momentum operator:

$$i\hbar\frac{\partial\psi(x, t)}{\partial t} = \frac{p^2}{2m_e}\psi(x, t) + V(x, t)\psi(x, t) \tag{50}$$

The TDSE is solved using the split-step Fourier method (SSFM) [36, 9]:

$$\begin{cases} \phi(x, t + \mathrm{d}t) = & \mathcal{F}\left(\psi(k, t)e^{-\frac{i}{\hbar}V(x,t)dt}\right) \\ \psi(k, t + \mathrm{d}t) = & \mathcal{F}^{-1}\left(\phi(x, t + \mathrm{d}t)e^{-\frac{i\hbar}{2m_e}k^2 dt}\right) \end{cases} \tag{51}$$

To avoid the interferences of the long and short trajectories, we use absorbing boundary condition to decrease the amplitude of the long trajectory (see B.2).

An example of the time evolution of the electron wavefunction in space and momentum domain is ploted Fig.24 , the peak intensity is set high ($I_o = 2 \times 10^{14}\,\text{W/cm}^2$) and pulse length short ($t_p = 20\,\text{fs}$) to make the oscillations from the laser field clearly visible.
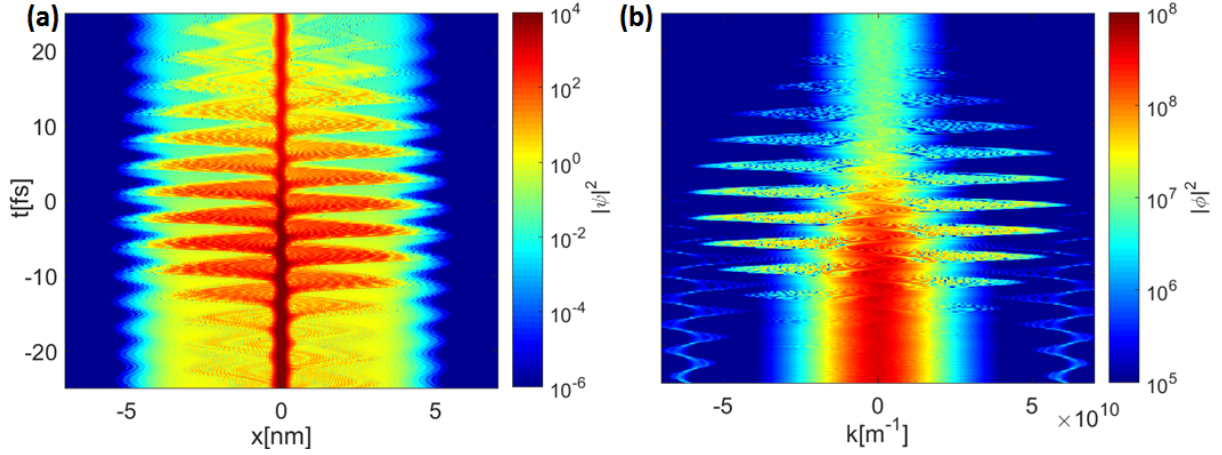

Figure 24: Time evolution of the probability density of the electron in (a) the space domain and (b) the momentum domain. *Krypton*, $\lambda = 1050\,\text{nm}$, $t_p = 46\,\text{fs}$ and $I_o = 2 \times 10^{14}\,\text{W/cm}^2$

Once we have the electron wavefunction, we can calculate the acceleration of the dipole moment via Ehrenfest's theorem [37, 38, 39] (more details in B.1):

$$d_A(t) \propto \left\langle \psi(x,t) \left| -\frac{\partial V(x,t)}{\partial x} \right| \psi(x,t) \right\rangle \tag{52}$$

And the spectrum of the dipole response amplitude is finally obtained by the Fourier transform: $A(\omega) = \omega^{-2} |\mathcal{F}(d_A)(\omega)|$, the dipole response of the qth harmonic is taken as $A_q = A(\omega_q)$.

Pulse length dependence

The dipole response amplitude spectra is plotted for different pulse lengths (Fig.30). Increasing the pulse length doesn't lead to significant higher dipole amplitude, however, it makes the peaks narrower.
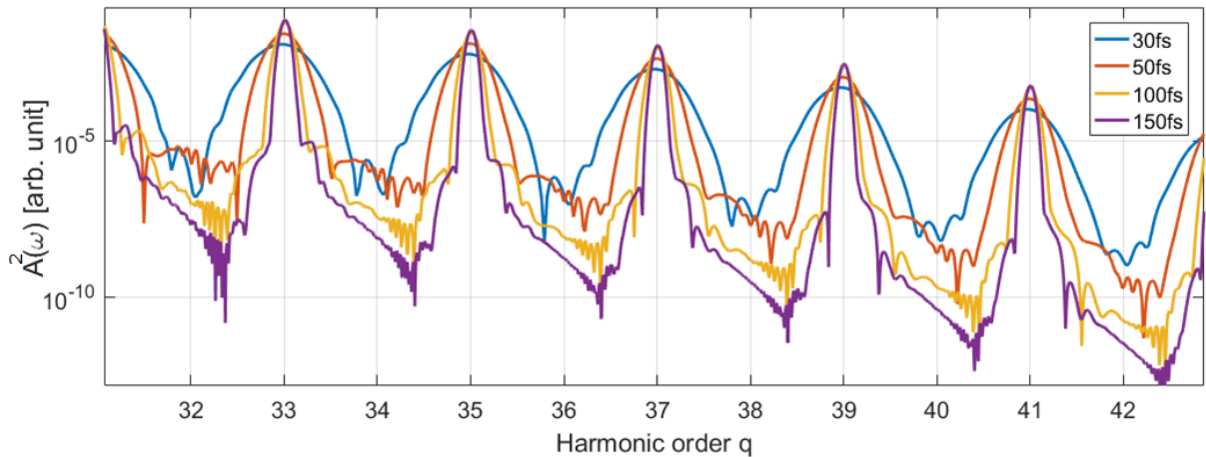

Figure 25: Harmonic spectra for different pulse length with Krypton at $1050\,\text{nm}$, a longer pulse length leads to a narrower peak. The peak intensity is $7 \times 10^{13}\,\text{W/cm}^2$.

Intensity dependence

The harmonic spectra is plotted for different intensities (Fig.26). For a given harmonic, the dipole response shows a strong dependence on the peak intensity, but after a certain value, increasing the peak intensity does not further increase the dipole power, and only leads to the generation of higher harmonics.
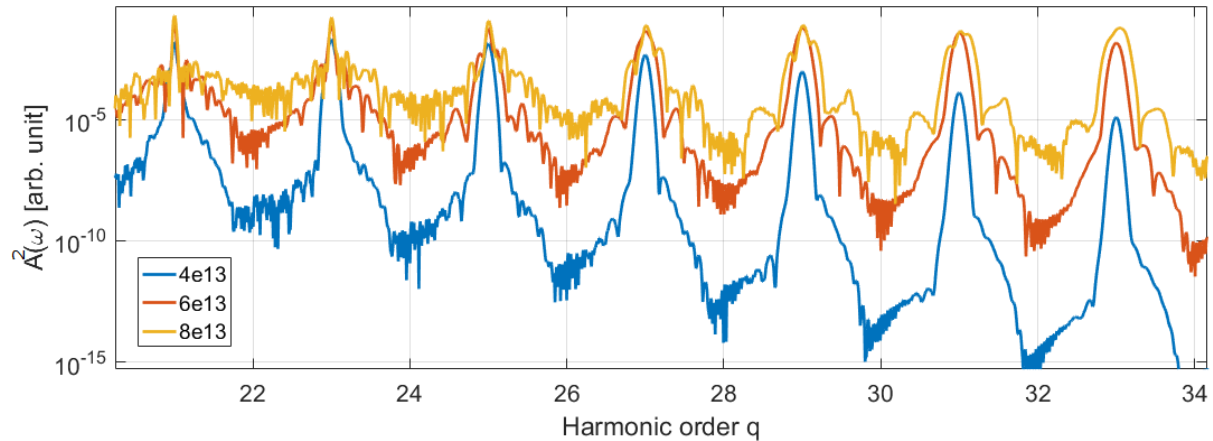
Figure 26: Harmonic spectra for different peak driving field intensities (in W/cm^2). Krypton, $t_p = 100\,fs$, $\lambda = 1050\,nm$.

The dipole response amplitude of the odd harmonics as function of the peak driving field intensity is plotted Fig.27. This figure allows us to have a better understanding of how the dipole response scales with intensity. Indeed, after a fast increasing, all the harmonics seem to "join" the same curve before the dipole response saturate. For a more accurate understanding, we define three scaling regimes as follow :

Figure 27: Dipole response amplitude of the odd harmonics as function of the laser peak intensity. Krypton, $t_p = 100\,fs$, $\lambda = 1050\,nm$.

Regime: "fast" $A_q \approx \left(\frac{I_o}{I_{\text{cut}}}\right)^{10}$, "slow" $A_q \approx \left(\frac{I_o}{I_{\text{sat}}}\right)^4$ and saturated $A_q = cst$.

- *Low harmonic* ($I_{\text{cut}} = 0$):
  A_q "slowly" increase to the saturated dipole response, which is set to 1 in the plot, and then stay constant.

- *Medium harmonic* ($0 < I_{\text{cut}} < I_{\text{sat}}$):
  A_q "rapidly" increase until $I = I_{\text{cut}}$, then "slowly" increase to the saturated dipole response, and then stay constant.

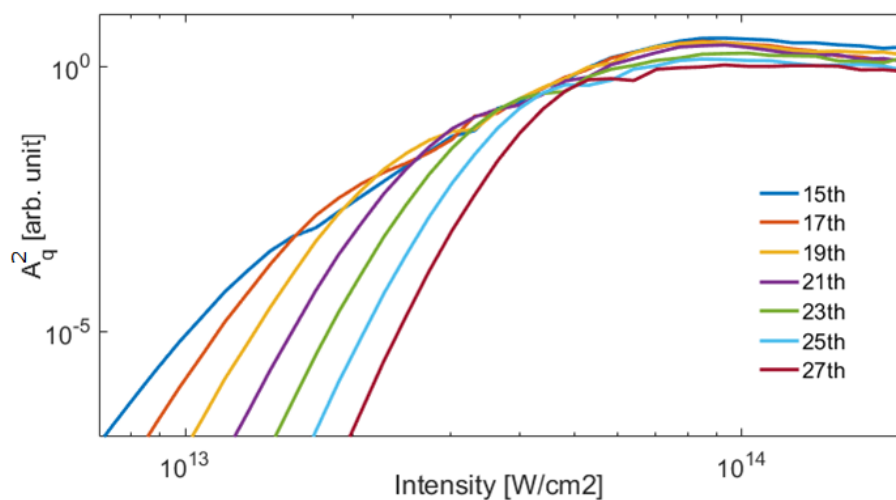- *High harmonic* ($I_{\text{cut}} > I_{\text{sat}}$):
  A_q "rapidly" increase to the saturated dipole response, and then stay constant.

Each harmonic has a different cutoff intensity I_{cut} which is calculated from Eq.1 (see I.1.1), on the other hand I_{sat} seems to be the same for all harmonics, but has no simple theoretical explanation. For krypton $I_{\text{sat}} \approx 5 \times 10^{13}\,\text{W/cm}^2$. The numbers 10 and 4 of the "fast" and "slow" regime are actually slightly different for each harmonic : It increases for higher harmonic order.

Figure 28: Peak intensity dependent dipole response amplitude of the 9th, 19th and 41th harmonic, highlighting the different regimes described on the left.

For $I_o < I_{\text{sat}}$, these results are in good agreement with the study [40], which calculated the dipole moment quantum mechanically and averaged over quantum interferences. However, the method used in our study, first presented in [37], predict a saturation after $I_o > I_{\text{sat}}$.
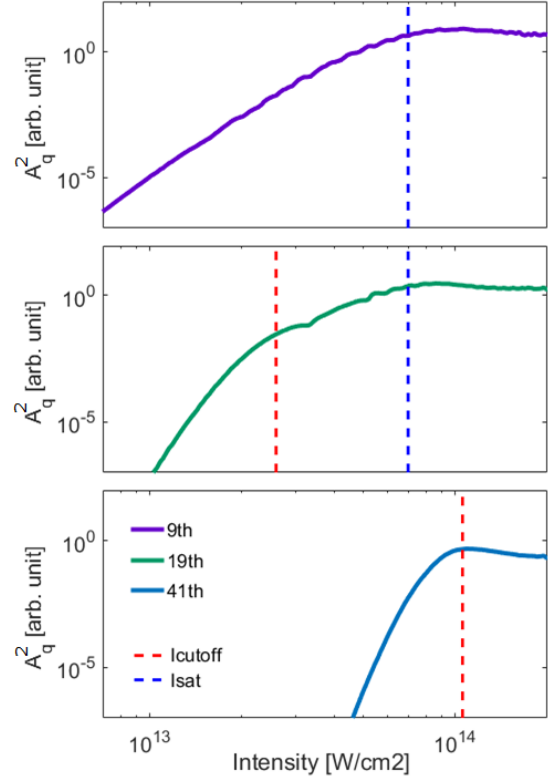
III.2 Phase matching

The harmonic field is created by the fundamental field, but as the two fields propagate, their phases can become mismatched. Because the amplitude of the generated field is maximized when the phase mismatch is zero, the phase mismatch limits the efficiency of harmonic generation. Thus we want the phase of the harmonic field to match that of the fundamental field over the longest possible interaction length, allowing for constructive interference and the maximum harmonic amplitude.

Summary

So far we have discussed all contributions to phase mismatch in the HHG process, and will summarize quickly before proceeding to the next step.

Dipole moment of the electron (I.1.2)

The dipole moment contribution comes from the electron ionization time. Given any photon energy there are two instances in the laser field (the maximum and the minimum) where the tunneling probability is the greatest. These give rise to long and short trajectory electrons respectively. The subsequent phase shift is

$$\Phi_{\text{dipole}}(z, r) = \alpha I(z, r, t) \tag{53}$$

This phase linearly dependent on the intensity profile of the fundamental laser pulse. As we are experimentally interested only in the short trajectory, we will work with $\alpha = 2 \times 10^{-14} \, \text{cm}^2/\text{W}$ for the whole following study.

Tightly focused Gaussian beam (I.3)

To create the high intensities necessary for HHG to take place, a tight-focusing geometry is aligned with the position of the gas jet. The phase of a tight focused Gaussian beam changes dramatically through the focus , and is given in free space by

$$\phi(z, r) = kz + k\frac{r^2}{2R(z)} - \zeta(z) \tag{54}$$

Index modification by neutral atoms and plasma (I.4)

The neutral gas and the plasma modify the index of refraction away from unity, and is dependent on both pressure and the ionization fraction. We use the phenomenological Sellmeir equation to describe the neutral atoms, and obtain

$$n(z, r, t, \omega) = 1 + \frac{P(z, r)}{P_{atm}} \left((1 - \eta(z, r, t)) \, \delta(\omega) - \eta(z, r, t) \frac{N_{atm} e^2}{2\omega^2 m_e \varepsilon_o} \right) \tag{55}$$

The pressure $P(z, r)$ is studied in I.2 and the ionization fraction $\eta(z, r, t)$ in II

III.2.1   Expression

The phase matching $\Delta\phi$ is defined as the phase mismatch between the harmonic and the fundamental:

$$\Delta\phi = q\phi_1 - \phi_q \tag{56}$$

Both the fundamental and the harmonics are Gaussian beams, however they do not necessarily have the same beam radius. The phase shift of a Gaussian beam with a refractive index n is the same as a Gaussian beam in free space but considering a wavelength of λ/n instead of λ. For clarity we define :

$$\phi_{\text{foc}}(\omega) = \frac{\omega}{c}\frac{n(\omega)r^2}{2R(z,\omega)} - \arctan\left(\frac{z}{n(\omega)z_R(\omega)}\right)$$
$$\text{with}\quad R(z,\omega) = z\left(1 + \left(\frac{n(\omega)z_R(\omega)}{z}\right)^2\right) \tag{57}$$

We also have to consider that the harmonics have a phase shift from the atomic response Φ_{dipole}. The phase of the fundamental and the harmonic are:

$$q\phi_1 = qk_1n(\omega_1)z + q\phi_{\text{foc}}(\omega_1) + \Phi_{\text{dipole}} - q\omega_1 t$$
$$\phi_q = k_q n(\omega_q)z + \phi_{\text{foc}}(\omega_q) - \omega_q t \tag{58}$$

The phase mismatch can then be written (note that the time phase shift cancel each other):

$$\Delta\phi = \Delta\phi_{\text{Disp}} + \Delta\phi_{\text{foc}} + \Phi_{\text{dipole}}$$
$$\text{with}\quad \Delta\phi_{\text{foc}} = q\phi_{\text{foc}}(\omega_1) - \phi_{\text{foc}}(\omega_q) \tag{59}$$
$$\text{and}\quad \Delta\phi_{\text{Disp}} = k_q z[n(\omega_1) - n(\omega_q)]$$

When we are close to the axis ($r \approx 0$), we have $q\phi_{\text{foc}}(\omega_1) \gg \phi_{\text{foc}}(\omega_q)$, that is why the phase from the harmonic focusing is always neglected in literature [17, 5, 41, 42]. Using the refractive index expression in Eq.55. We can write the phase mismatch due to dispersion:

$$\Delta\phi_{\text{Disp}} = k_q z\frac{P(r,z)}{P_{\text{atm}}}\left((1 - \eta(z,r,t))[\delta(\omega_1) - \delta(\omega_q)] - \eta(z,r,t)\frac{N_{\text{atm}}e^2}{2m_e\varepsilon_o}\left[\frac{1}{\omega_1^2} - \frac{1}{\omega_q^2}\right]\right) \tag{60}$$

For high harmonic order, we can simplify, defining $\Delta\delta = \delta(\omega_1) - \delta(\omega_q)$:

$$\Delta\phi_{\text{Disp}} = k_q z\frac{P(r,z)}{P_{\text{atm}}}\left((1 - \eta(z,r,t))\Delta\delta - \eta(z,r,t)\frac{N_{\text{atm}}e^2}{2m_e\varepsilon_o}\frac{1}{\omega_1^2}\right) \tag{61}$$

It is also useful to introduce the norm wavevector mismatch [17] $\Delta k = |\vec{k_q}| - q|\vec{k_1}|$, where $\vec{k} = \vec{\nabla}\phi$ (Note that $\vec{k_q}$ and $\vec{k_1}$ are not necessarily co-linear). A small Δk indicate a small phase mismatch change as the beam propagates, which usually lead to an efficient harmonic generation. In literature the norm Δk and the coherence length $L_{\text{coh}} = \frac{\pi}{\Delta k}$ are commonly used to talk about phase matching in HHG. The Figure 29 plot the coherence length for different intensities and pressure, it gives a first understanding on how these parameters affect the phase matching, more details are discussed below.
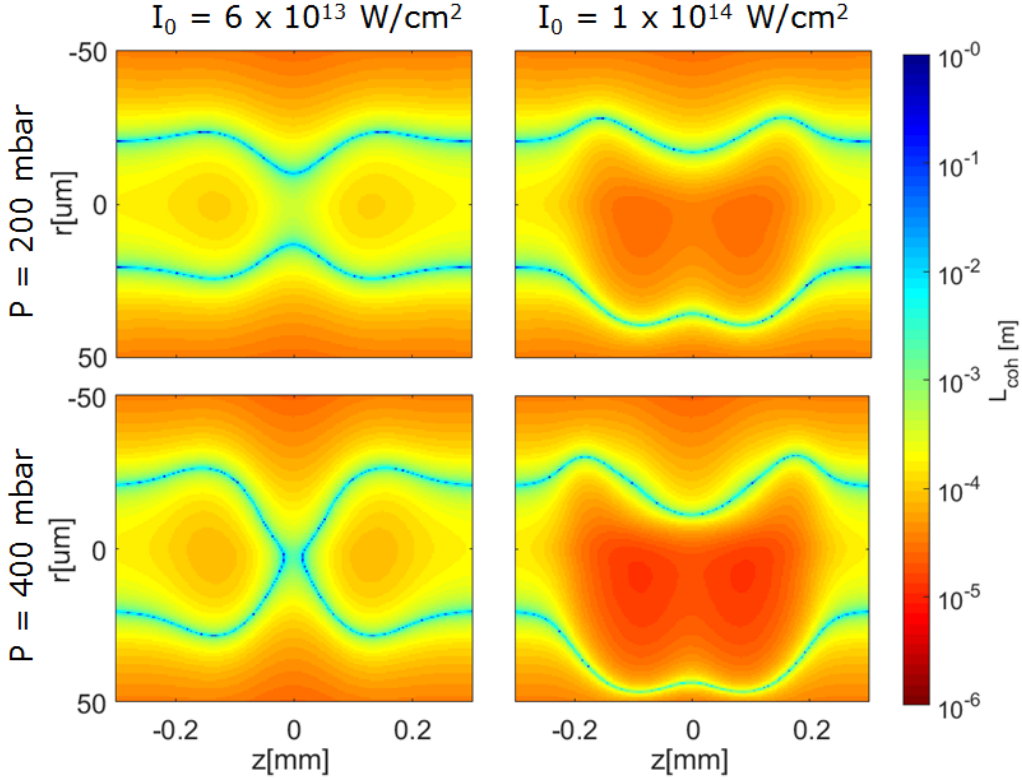
Figure 29: The Coherence length L_{coh} is plotted along axis z and r for different intensities and pressure. For $I = 6 \times 10^{13} \, \text{W/cm}^2$, increasing the pressure improve the phase matching near the focus, but for $I = 1 \times 10^{14} \, \text{W/cm}^2$, increasing the pressure makes it worse. 21st, Krypton, $\lambda = 1050 \, \text{nm}$, $\omega_o = 19.6 \, \mu\text{m}$, $t_p = 130 \, \text{fs}$, $l_p = 200 \, \mu\text{m}$.

III.2.2 Phase matching pressure and critical ionization

We study in this section how the phase matching is affected by the pressure and the ionization fraction (the ionization fraction being strongly correlated to intensity).

Critical ionization fraction

For a better understanding of Eq.61 we define the "critical ionization fraction" η_c [43], which is the ionization fraction such that $\Delta\phi_{\text{Disp}} = 0$.

$$\eta_c = \left(1 + \frac{N_{\text{atm}}e^2}{2m_e\varepsilon_o\omega_1^2\Delta\delta}\right)^{-1} \tag{62}$$

It is important to note that η_c depends on the gas and the harmonic order (Table 6).
We can now write:

$$\Delta\phi_{\text{Disp}} = k_q z \frac{P(r,z)}{P_{\text{atm}}}\Delta\delta\left(1 - \frac{\eta(z,r,t)}{\eta_c}\right) \tag{63}$$

Table 6 gives the calculated critical ionization fraction for different gas and harmonics

	Argon	Krypton	Xenon
21st	4.1	5.1	6.4
23th	3.5	4.6	6.1

Table 6: Calculated critical ionization fraction $\eta_c[\%]$ of Argon, Krypton and Xenon for the 21st and the 23th harmonic.

Phase matching at the focus

On the z axis ($r = 0$), $\vec{k}_q$ and $\vec{k}_1$ are colinear, so we can write [5]:

$$\Delta k = |\vec{k}_q - q\vec{k}_1|$$
$$\Delta k = \Delta k_{\text{Disp}} + \Delta k_{\text{foc}} + \Delta k_{\text{dipole}} \tag{64}$$

With $\quad \Delta k_{\text{Disp}} = \dfrac{\partial}{\partial z}\Delta\phi_{\text{Disp}}, \quad \Delta k_{\text{foc}} = \dfrac{\partial}{\partial z}\Delta\phi_{\text{foc}}, \quad \Delta k_{\text{dipole}} = \dfrac{\partial}{\partial z}\Phi_{\text{dipole}}$

At the focus ($r = z = 0$), we have $\Delta k_{\text{foc}} = -\frac{q}{z_R}$ and $\Delta k_{\text{dipole}} = 0$.
Also if we consider that $\vec{\nabla}\eta(0,0) \approx \vec{0}$, then we can right:

$$\Delta k(0,0) = k_q \frac{P}{P_{\text{atm}}}\Delta\delta\left(1 - \frac{\eta}{\eta_c}\right) - \frac{q}{z_R} \tag{65}$$

P and η are the pressure and ionization fraction at the focus.
$\Delta\delta$ being positive, from this last relation it is now clear that a "perfect phase matching pressure" P_{opt} (such that $\Delta k = 0$ at the focus) will exist only if $\eta < \eta_c$:

$$P_{\text{opt}} = \frac{P_{\text{atm}}}{k_1 z_R \Delta\delta\left(1 - \frac{\eta}{\eta_c}\right)} \tag{66}$$

η_c is the ionization fraction where P_{opt} reach infinity, hence its name. For a ionization higher than the critical ionization, increasing the pressure only makes the phase matching worse at the focus.
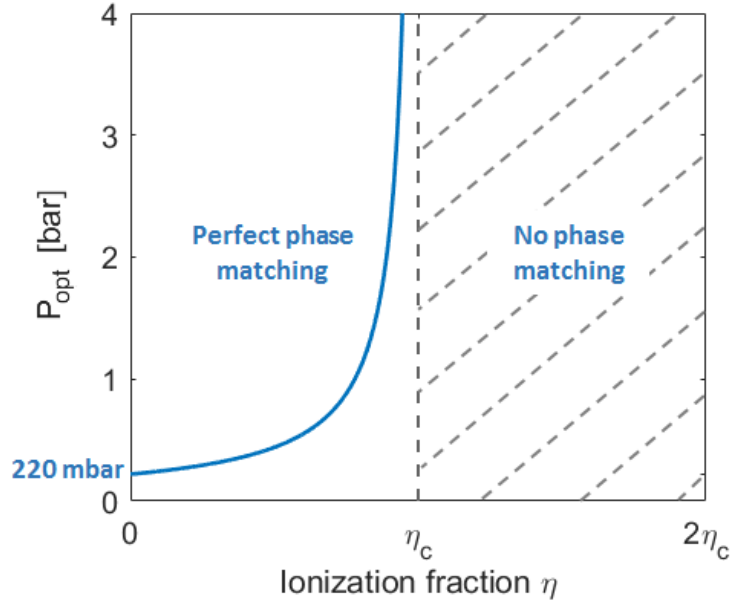

Figure 30: Calculated perfect phase matching pressure for the 21st harmonic in Krypton at $\lambda = 1050\,\text{nm}$.

Phase matching plateau

It is important to consider that Harmonics are not generated in a single point, but along the interaction region, which is determined by the nozzle diameter (see I.2). If the phase matching is good at the focus but bad 30 μm after the focus, it eventually leads to a bad harmonic amplitude output. The Fig.31 highlight the different phase matching plateaus that we can find depending on the intensity. We notice that even though there is a perfect phase matching pressure for higher intensity, the phase matching plateau is smaller, which lead to a less efficient HHG.
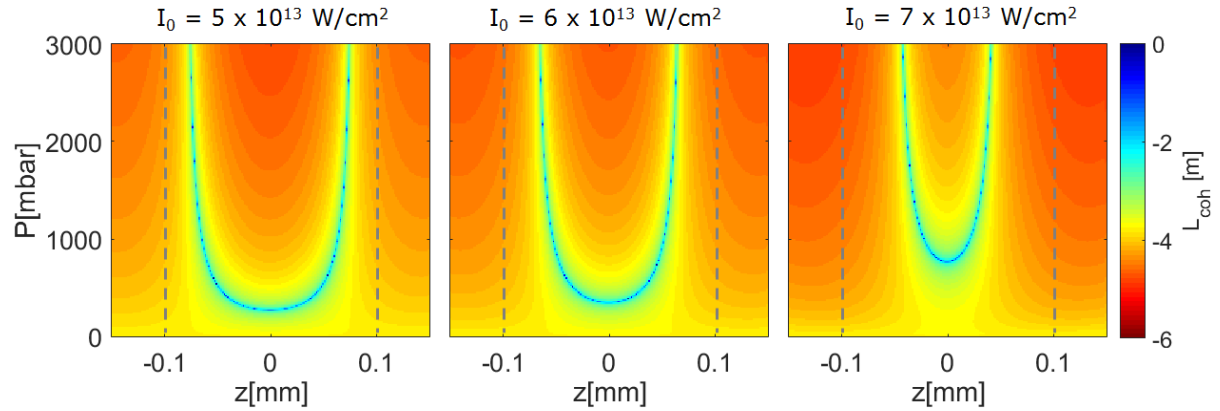

Figure 31: On axis pressure dependent phasematching for different peak intensities, the interaction region is delimited by the dashed lines ($l_p = 200\,\mu\mathrm{m}$). The phase matching plateau is getting smaller for higher intensities. Krypton, $\lambda = 1050\,\mathrm{nm}$, $\omega_o = 19.6\,\mu\mathrm{m}$, $t_p = 130\,\mathrm{fs}$, $q = 21$.

III.3 Results of the simulation

Now that we have understood the microscopic (dipole response) and the macroscopic (phase matching) phenomenons involved in the High Harmonic Generation process, we are able to calculate the on-axis generated harmonic amplitude using Eq.48.

III.3.1 Phase-matching and absorption impacts on HHG

The importance of phase-matching

The figure below shows the harmonic amplitude growth on z axis for different phase matching configurations. It is now clear how a bad phase matching can lead to an inefficient harmonic generation.
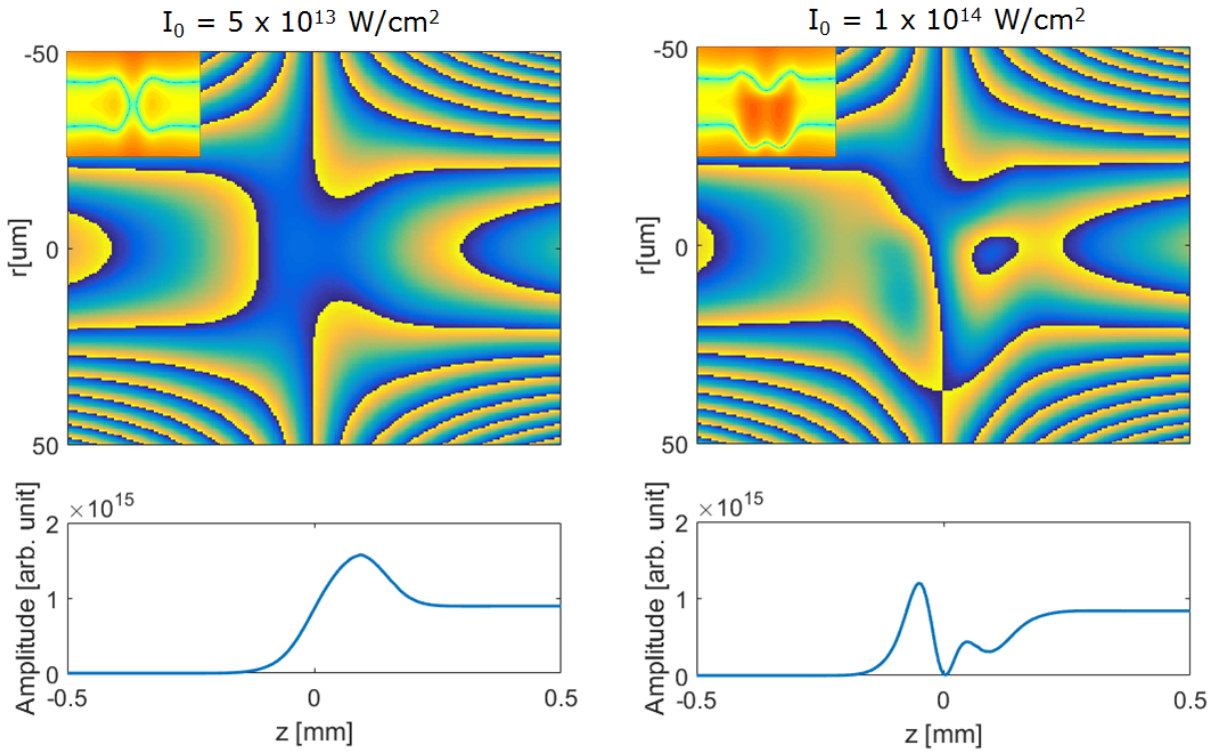
Figure 32: Phase matching and harmonic amplitude growth on axis for two different intensities. Krypton, $V = 300\,\text{m/s}$, $P = 300\,\text{mbar}$, $\lambda = 1050\,\text{nm}$, $\omega_o = 19.6\,\mu\text{m}$, $t_p = 130\,\text{fs}$, $l_p = 200\,\mu\text{m}$, $q = 21$.

The final amplitude is around 1×10^{15} in both case, however the dipole response is around 5 times higher for $I = 1 \times 10^{14}\,\text{W/cm}^2$ than $I = 5 \times 10^{13}\,\text{W/cm}^2$. So if the phase matching conditions were the same for both cases, the output would have been much higher for $I = 1 \times 10^{14}\,\text{W/cm}^2$, but the bad phase-matching in the second case create destructive interferences and leads to a smaller output.

The decreasing in the first case is caused by absorption, the harmonics created near the focus are absorbed by the medium, and because the phase matching is worse on the side, less harmonic power is generated.

The importance of absorption

To understand how important the role of absorption is in the High harmonic generation, we compare the medium length $L_{\text{med}} = l_p$ with the absorption length L_{abs} (see I.2.2). As highlighted in the Fig.33, if the absorption length is too small, Harmonic created at the beginning of the interaction region will be fully absorbed by the medium and will not participate to the harmonic output.
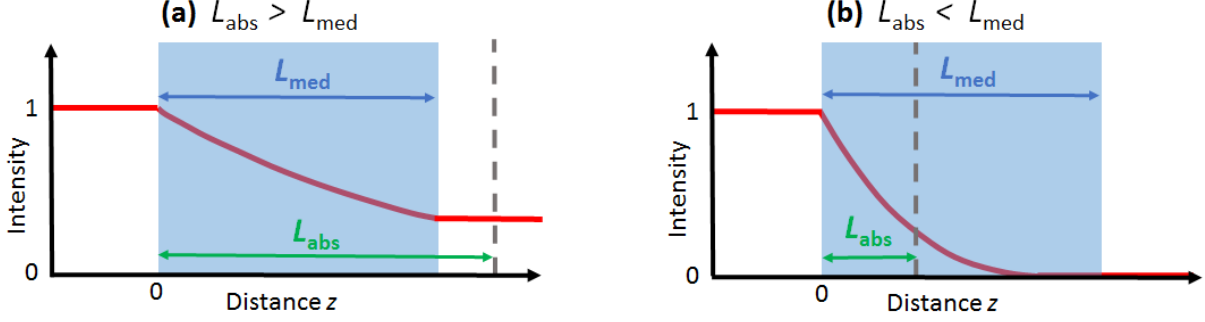

Figure 33: Absorption through a medium (blue) for different absorption length (square density profile).

It is now clear that only the harmonics created after $z = L_{\text{med}} - L_{\text{abs}}$ will cross the interaction region with less than 63 % loss. It means that, for $L_{\text{abs}} << L_{\text{med}}$, only the phase matching in the last part of the medium will actually matters. It is a problem because, due to the high pressure gradient near the gaussian tail, the phase matching is usually bad on the sides of the interaction medium (Fig.31).

III.3.2 Harmonic amplitude scaling

Scaling in ideal cases

The ideal case for most efficient frequency conversion occurs when there is no absorption ($\sigma = 0$) and a perfect phasematching ($\Delta k = 0$). In this case, the harmonic signal increases quadratically with the medium length and pressure [44]:

$$I_q \propto A_q^2 \left(P \, l_p \right)^2 \tag{67}$$

For a high absorption ($L_{\text{abs}} << l_p$), harmonics are created only in the last part of the interaction region. with a perfect phase-matching, we have:

$$I_q \propto A_q^2 \left(P \, L_{\text{abs}} \right)^2 \propto A_q^2 \tag{68}$$

If we consider that the absorption is negligible ($L_{\text{abs}} >> l_p$), which is the case for higher harmonic and low pressure, we have [5]:

$$I_q \propto A_q^2 \, \text{sinc}^2 \left(\frac{\Delta k \, l_p}{2} \right) \tag{69}$$

While it is impossible to modify the value of σ unless we change gas or harmonic, we can on the other hand adjust experimental parameters (pressure, intensity, interaction length, etc..) to try getting perfect phase-matching.

Scaling with the peak intensity

Increasing intensity leads to a higher dipole response but also eventually to a worse phase matching (because of the ionization fraction). The Fig.34 plot the harmonic amplitude in function of the peak intensity for different pressure.
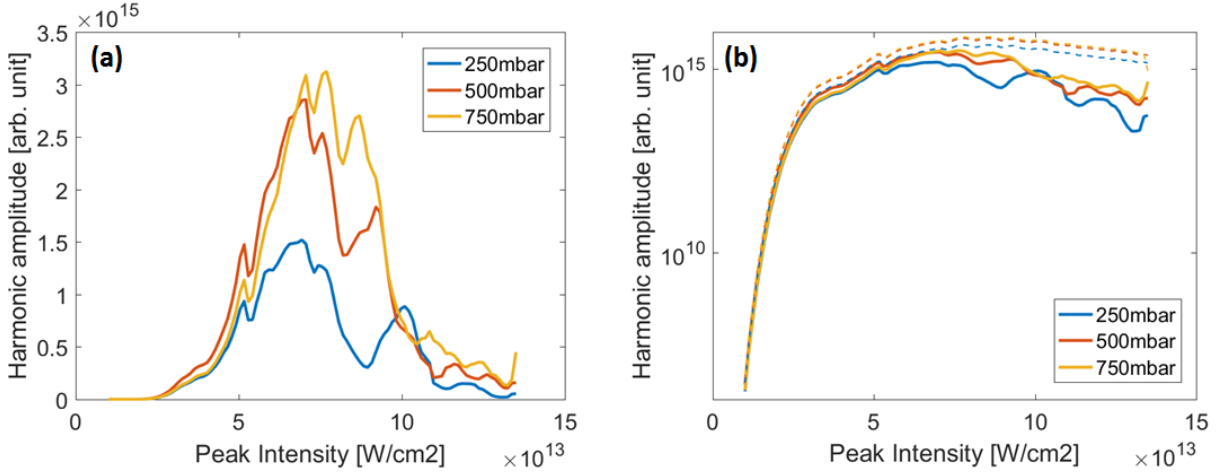

Figure 34: Harmonic output amplitude as a function of intensity for different pressure in (a) linear and (b) log scale. The dashed lines represent the harmonic output for a perfect phase-matching to highlight the limitations due to absorption. $V = 200\,\mathrm{m/s}$, $t_p = 130\,\mathrm{fs}$, $l_p = 150\,\mu\mathrm{m}$, $q = 21$, Krypton.

For low intensities, the dipole response is very sensitive to the intensity, which explain the fast increasing of the harmonic amplitude until $I_o = 5\,\mathrm{W/cm^2}$; for higher peak intensities, the dipole response saturate and the harmonic amplitude only depends on phase matching conditions. These calculation suggest that a maximum amplitude output is obtained for an optimum intensity, around $I_o = 7\,\mathrm{W/cm^2}$ in our experiment. It is in good agreement with measurement from [45]. The Fig.35 plot the harmonic amplitude for different harmonic order.

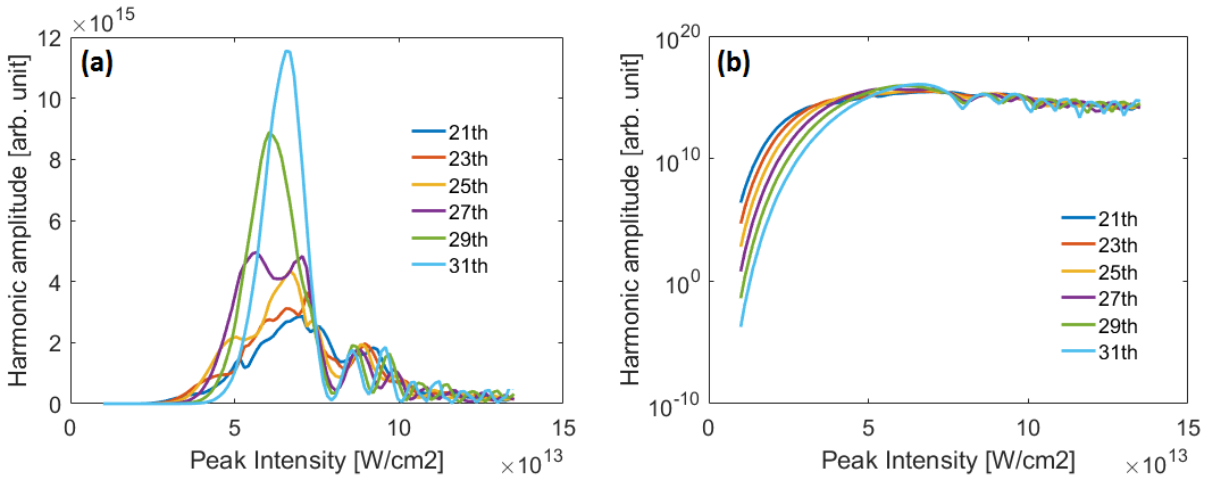**Figure 35:** Harmonic output amplitude as a function of intensity for different harmonic in (a) linear and (b) log scale. . $V = 250\,\mathrm{m/s}$, $t_p = 130\,\mathrm{fs}$, $l_p = 150\,\mu\mathrm{m}$, $P = 500\,\mathrm{mbar}$, Krypton.

Scaling with pressure

Increasing the pressure leads to an increasing in the harmonic growth as well as a decreasing due to absorption (Eq. 48), and also leads to significant changes in the phase matching. Therefore, it is not obvious what is the optimum pressure for our system. The Fig.36 plot the harmonic amplitude as a function of pressure for different peak intensity and harmonics.
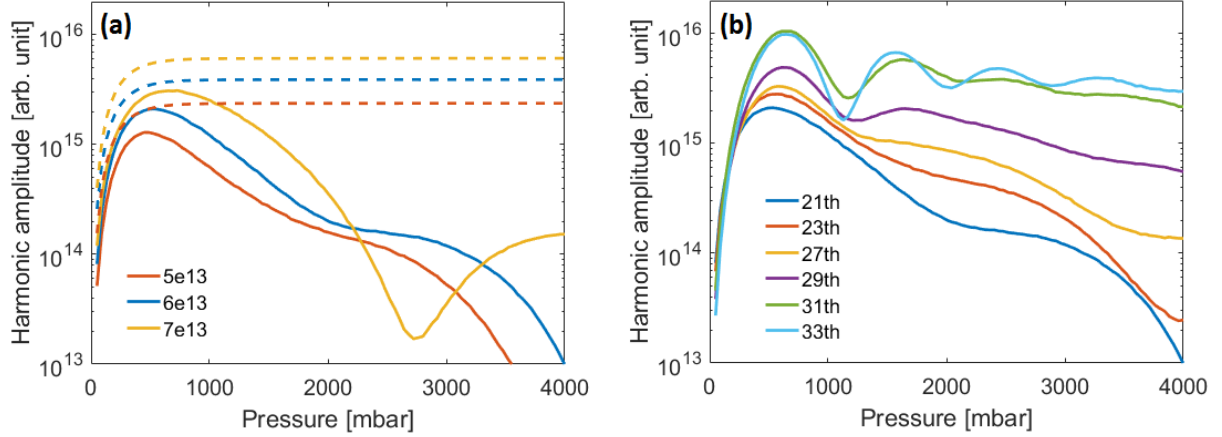

Figure 36: Harmonic output amplitude as a function of pressure for (a) different intensities and (b) different harmonics. The dashed lines represent the harmonic output for a perfect phase-matching to highlight the limitations due to absorption. $V = 250\,\mathrm{m/s}$, $t_p = 130\,\mathrm{fs}$, $l_p = 150\,\mathrm{\mu m}$, Krypton, (a) $q = 21$, (b) $I_o = 6 \times 10^{13}\,\mathrm{W/cm^2}$.

As the pressure increase, the absorption length $L_{abs} \propto {}^1/_P$ decrease and when $L_{abs} << l_p$, harmonics are created only in the last part of the interaction region. But in the same time the harmonic intensity also grows faster ($I_q \propto (P\,L_{abs})^2$), in the end these two phenomenon cancel each other and the harmonic amplitude only depends on phase-matching. The decreasing after $P \approx 500\,\mathrm{mbar}$ is due to bad phase-matching on the tail of the gaussian density profile.

On Fig.36b, we notice oscillations for lower harmonics. It is because the absorption length is longer for lower harmonic (I.2.2), and as discussed in III.3.2, harmonics grow following $I_q \propto A_q^2 \operatorname{sinc}^2\left(\dfrac{\Delta k\, l_p}{2}\right)$ for negligible absorption. It is in good agreement with measurement in [5]. Note that Δk is proportional to pressure and ionization fraction, so there is changes in the oscillations period as we ramp up the pressure or the intensity.

Scaling with the interaction length

Increasing the interaction length will generate more harmonics but a part of it will be absorbed and it will also make the phase matching less homogeneous along the medium. The Fig.37 plot the harmonic amplitude as a function of the interaction length for different pressures, a pressure dependence plot for different interaction length is also shown. The dashed lines represent the harmonic output for a perfect phase-matching to highlight absorption limitations.
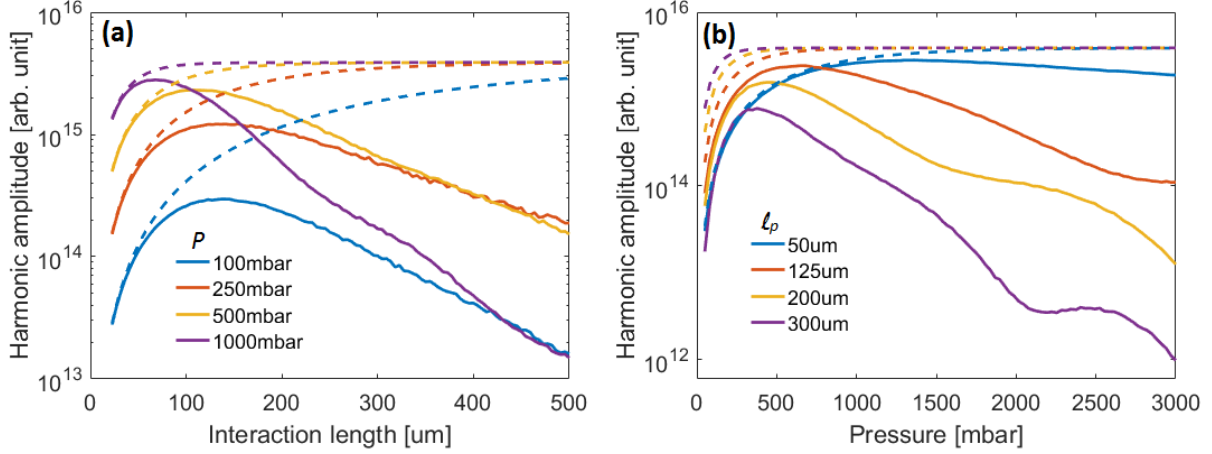

Figure 37: Harmonic output amplitude as a function of (a) interaction length and (b) pressure for different (a) pressure and (b) interaction length. The dashed lines represent the harmonic output for a perfect phase-matching. $V = 250\,\text{m/s}$, $t_p = 130\,\text{fs}$, $q = 21$, $I_o = 6 \times 10^{13}\,\text{W/cm}^2$, Krypton.

Nozzle position dependence

It may be worth to move the nozzle to a place where phase matching is better, but the dipole response will decrease, Fig.38 demonstrate how the nozzle position can influence the harmonic amplitude. The gas velocity is considered constant along the optical axis.
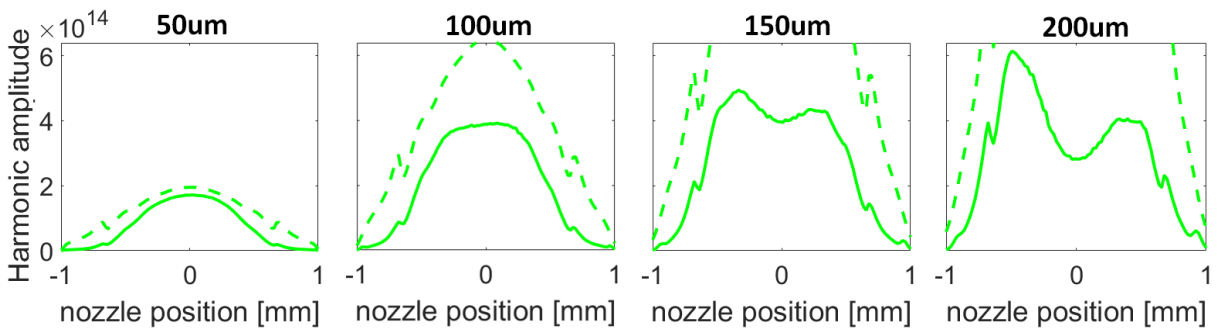
Figure 38: Harmonic output amplitude as a function of nozzle position for different interaction length, the dashed lines is the harmonic amplitude with perfect phasematching to highlight the limitations due to absorption. $V = 250\,\text{m/s}$, $P = 100\,\text{mbar}$, $t_p = 130\,\text{fs}$, $l_p = 150\,\mu\text{m}$, $q = 21$, $I_o = 6 \times 10^{13}\,\text{W/cm}^2$, Krypton.

We can see that for small interaction length, the optimum nozzle position is always $z = 0$, and on the other hand, long interaction region leads to a better phasematching in the sides than at the center.

Harmonic generation within a pulse

Harmonics are not all created at exactly $t = 0$ fs but are actually generated during the whole pulse. As the intensity varies along time (gaussian pulse), two phenomenon occurs:

- The dipole response is directly related to the intensity, so it varies through time

- The phase-matching may change dramatically during the pulse because of the ionization fraction

It has been demonstrated for single pass HHG in [46] that, because of bad phase matching, the maximum generated harmonics is not necessary at $t = 0$ (when the dipole response is the highest) and can be before or after the peak intensity. Fig.39 is an example of an harmonic pulse limited by the phase matching.
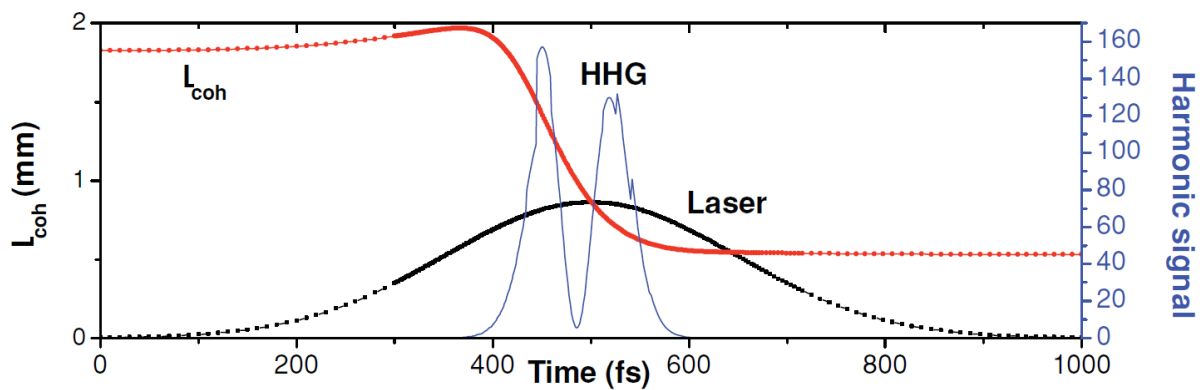

Figure 39: Computation of temporal evolution of both the coherence length and the harmonic signal (in arbitrary units). Single pulsed, $P = 85$ mbar, $t_p = 350$ fs, , $q = 55$, $I_o = 1 \times 10^{14}$ W/cm^2, $l_p = 2$ mm, Argon, from [46].

However, while the ionization fraction within a pulse will go from 0 to η in single pass HHG, it doesn't change much ($< 1\%$) in high repetition rate systems as the medium is already ionized before the incoming pulse. Therefore, the changes in the phase matching during the pulse are most of the time negligible and the harmonic amplitude temporal evolution will mostly follow the dipole response evolution (Fig.40).

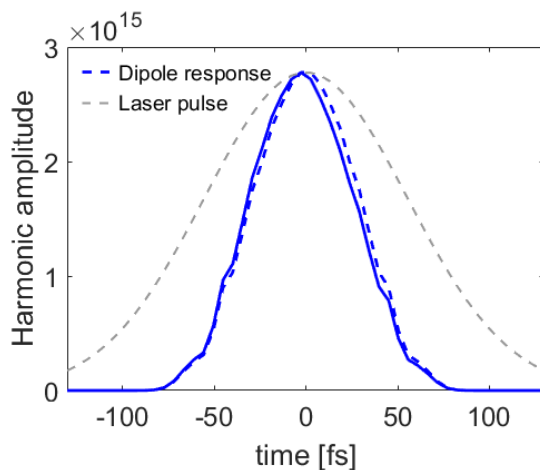**Figure 40:** Time evolution of the harmonic amplitude during the pulse, the dipole response is plotted in blue dashed line and the laser pulse in grey dashed line. We notice that the harmonic pulse has a very similar shape to the dipole response, which indicate a small change in the phase matching during the pulse. $V = 250$ m/s, $P = 500$ mbar, $t_p = 130$ fs, $l_p = 150$ µm, $q = 21$, $I_o = 7 \times 10^{13}$ W/cm^2, Krypton.

Summary of the simulations

We have calculated the harmonic amplitude as a function of different parameters, this table summarize how to optimize the harmonic output power in each case.

Parameter	How to optimize
Peak intensity I_o	For any configuration, the optimum peak intensity is roughly $7 \, \mathrm{W/cm^2}$, which correspond to the intensity when the increasing of the dipole response does not compensate the destructive effects of the bad phasematching anymore (due to ions). Changing the gas, the beam radius or the laser frequency would modify this value.
Pressure P	Increasing the pressure indefinitely does not work because it degrades the phasematching, and also increase the absorption effects. The optimum pressure varies between each configurations ($500 \, \mathrm{mbar} - 1000 \, \mathrm{mbar}$), and it is most of the time limited by the absorption rather than phasematching.
Interaction length l_p	For our range of optimal pressure, the best interaction length is in the range of $50 \, \mathrm{\mu m}$ - $120 \, \mathrm{\mu m}$ which is smaller than what we can do experimentally.
Nozzle position z_{noz}	For low interaction length, $z_{\mathrm{noz}} = 0 \, \mathrm{mm}$ is optimum, but as we increase l_p, moving the nozzle away from the focus would improve the harmonic output,
Time t	For high repetition rate systems, the highest harmonic power is always produced close to $t = 0 \, \mathrm{fs}$

It is important to note that these simulations does not compute the full process, indeed they are performed only with the on-axis contributions. A full 3D calculation of dipoles and propagating them into the far field to calculate beam profiles would require much more time and is nowadays an ongoing research field. However the on-axis calculation is a good approach to understand the HHG process and still gives accurate results.

IV Experimental setup & Measurement

IV.1 The femtosecond Enhancement Cavity (fsEC)

The fsEC is used to obtain the required high peak intensity for the HHG process ($\approx$ $1 \times 10^{14}\,\mathrm{W/cm^2}$) while at the same time maintaining the desired high repetition rate (Fig.41). Every photons has to do a complete cavity round between each pulse, and go back to the starting point exactly at the same time as the arrival of the next pulse. Because of the extreme precision required on the cavity length, effects such as vibrations or thermal expansion are non-negligible, and we actively stabilize the cavity length using a control loop with one mirror mounted on a PZT to continuously adjust the cavity length.

As we studied in II.2, working with a lower frequency would lead to a lower ionization fraction, however, with a frequency $f = 60\,\mathrm{MHz}$, the cavity length has to be $L = c/f = 5\,\mathrm{m}$, which is already experimentally challenging. Reducing the laser frequency would result in an increasing of the cavity length, that is why $f = 60\,\mathrm{MHz}$ seems to be a good compromise between ionization fraction and cavity length.
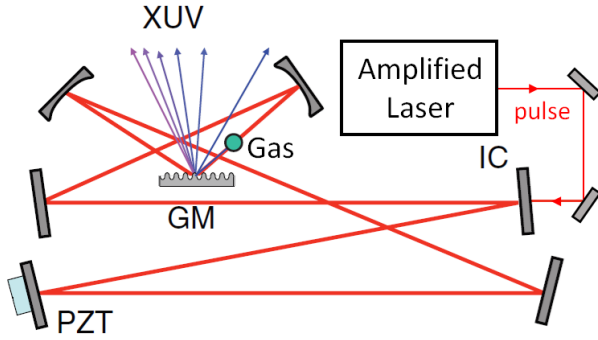

Figure 41: Schematic of a fsEC-based XUV source using a diffraction grating mirror (GM) XUV output coupler, a fsEC input coupler (IC) and a piezo transducer (PZT) used to control the cavity length [13].

Because residual plasma leads to imperfect mode matching and nonlinear dispersion, the intracavity average power is limited to few kilowatts (as a too high intensity creates plasma in the focus area); the enhancement is also limited by the mirrors loss. More details on the fsEC setup can be found in [12, 47].

The frequency comb mode-locked laser

Ti:Sapphire mode-locked laser oscillator are nowadays widely used in HHG experiment for their tunability and their ability to generate ultrashort pulses. However, because the average power of such systems is in the range of 1 W at the full rep-rate of the oscillator, it needs to be amplified while maintaining the high frequency to correctly seed the fsEC [2].

In our case, the mode-locked laser is realized with a with a low power (30 mW) Ytterbium-doped fiber ring oscillator amplified in a two stage amplifier system comprised of a single-mode fiber preamp and a Yb-doped photonic crystal fiber power amplifier, providing more than 20 W of output power. It enables to deliver a higher power than a system based on a Ti:Sapphire laser, more details can be found in [47, 2].

The output coupler

Once we are able to generate harmonics in the fsEC, the next step is to extract them from the cavity. To do so, we use an output coupler [13] which must efficiently couple the XUV out of the cavity while withstanding the high average power and peak intensity in the fsEC, and at the same time it must contribute negligible loss and dispersion in the circulating cavity field. The two output couplers that have been used most successfully in fsECs are the Brewster plate (BP) and the grating mirror (GM) output coupler (illustrated in Fig.42).
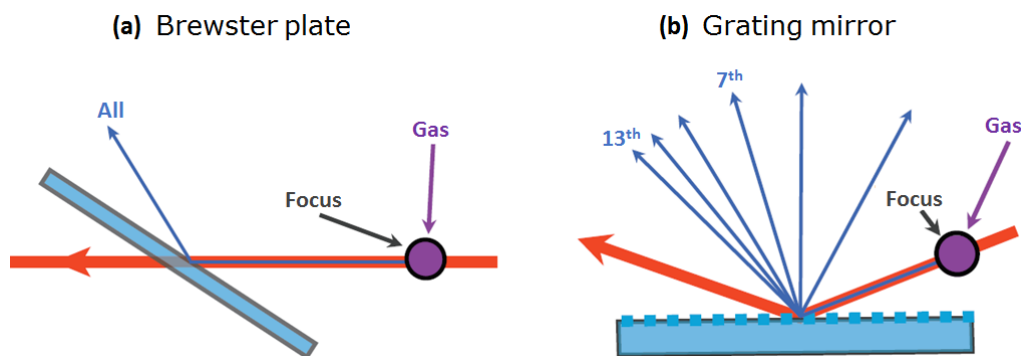

Figure 42: Illustration of (a) Brewster plate and (b) grating mirror XUV output coupler designs. The out-coupled harmonics are collinear in the BP output whereas they are spectrally dispersed in the case of the GM [13].

To separate the harmonics from the fundamental, both output couplers rely on the wavelength difference between the fundamental and the harmonics. The Brewster plate leans on the wavelength dependence of the reflection coefficient while on the other hand, the grating mirror is using the differences in the diffracted angle.

The out-coupled harmonics are collinear in the BP output whereas they are spatially separated in the case of the GM. However, the Brewster plate leads to nonlinear phase shift and has a reflection of about only 15 % in the XUV range, moreover a diffraction grating has to be used after the Brewster plate to separate the harmonics, which imply even more loss. However if the GM is used in the cavity, it has to be a highly reflecting mirror for the fundamental wavelength, which is particularly bad as a diffraction grating. The use of a BP in the cavity gives more freedom on the choice of the GM (which can be more efficient than if used in the cavity), and we generally end up having a similar photon flux in both cases.

The harmonic spectra

In our experiment, a grating mirror is used, and we can directly get the harmonic spectra, projected on a metal plate, coated with a UV phosphor powder (P22) which emits blue light when exposed to the XUV. However, the grating mirror also create second order diffracted modes, which can be sometimes as bright as the 1st order (29th harmonic). The harmonic output intensities are then measured by integrating the color over the height as shown Fig.43 while removing the background signal.
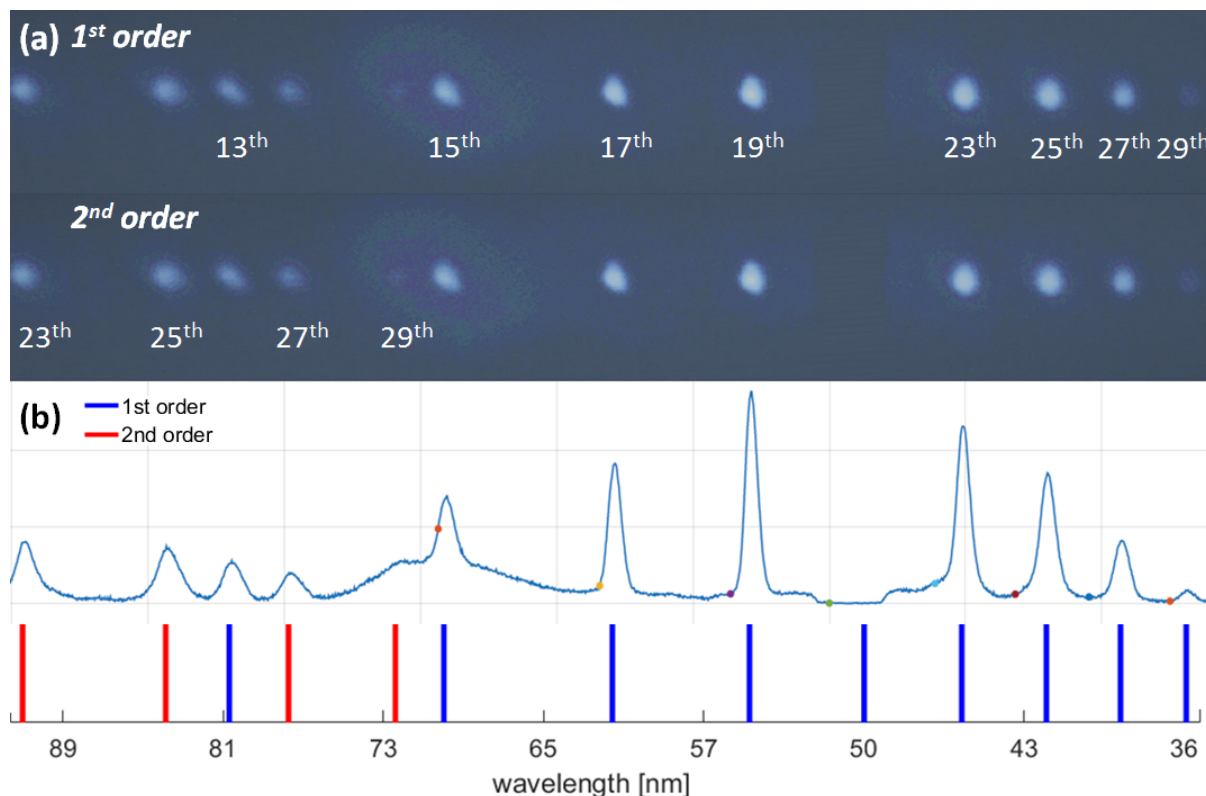

Figure 43: (a) Photo of sodium salicylate phosphor illuminated by 1st and 2nd order harmonics 13–29 and (b) measured harmonic spectra by integrating the color and removing the noise background, the corresponding theoretical harmonic positions is also plotted (explained in A.1). The 21st harmonic is missing because it is used for a photoemission spectroscopy experiment.

The cut-off is clearly visible for harmonics 23th to 29th, the plateau however is not flat, it is probably caused by the differences in the phase matching and absorption between the harmonics.

As there are two electron trajectories in the atomic response of the HHG process, interferences between the two sources can occur; however the short and the long trajectories have different dipole response amplitude [10] and phasematching conditions (I.1.2), thus the long trajectory may also be negligible compared to the short trajectory. This could explain why most of the peaks are "normal" when the 15th peak has a strange shape. The irregular 15th harmonic peak shape could be explained by interferences between the long and the short trajectory, which might be caused by an enhanced atomic response affecting the long trajectory only associated with krypton that plays a role in this range (it has not be observed with Xenon).

IV.2   Intracavity ionization

Because the process of ionizing the gas target is highly nonlinear, relatively small changes in the laser intensity can lead to large and very rapid changes in the plasma, and hence cavity phase, which changes the cavity resonance condition much faster than the control loop can compensate for ; this leads to instabilities if the feedback loop cannot adequately follow these resonance shifts. A numerical model has been developed to understand in detail how the intracavity ionization affects the dynamics of the circulating intracavity pulse [2, 48].

Cavity round trip

Within each round, the electric field is modified by propagation through the interaction region (temporal dispersion, Kerr loss and plasma response) and the seed pulse is then added to the circulating field, the model also consider the mirrors loss (details in [2]). The amplification factor and the intracavity plasma as a function of round trip number is plotted Fig.44.
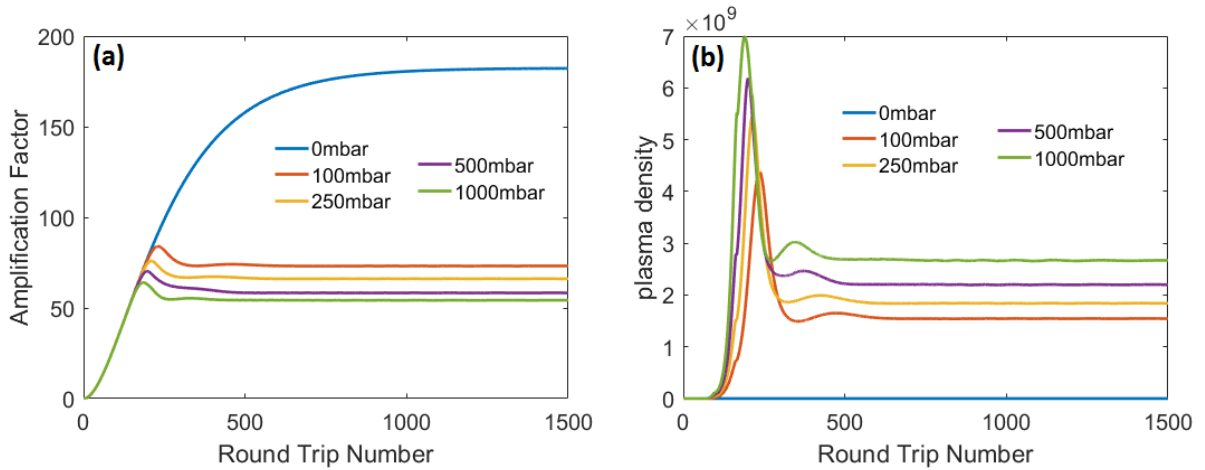

Figure 44: (a) Amplification factor and (b) plasma density as a function of cavity roundtrip for different pressure. As the pressure increase, the plasma density increase and limit the amplification factor. Seed pulse $= 500\,\text{nJ}$, $\omega_o = 19.6\,\mu\text{m}$, $\lambda = 800\,\text{nm}$, $f = 60\,\text{MHz}$, $l_p = 150\,\mu\text{m}$, Krypton.

This figure clearly highlights how the intracavity power is limited by the plasma. Since a higher pressure leads to a higher plasma density, the steady state intracavity power decreases with pressure.

Blue shift

A blue shift in the cavity spectrum has also been measured, and it can be explained by the plasma. A higher plasma density induce more nonlinear phase shift which result in a blue shift on the cavity wavelength. As studied before, a higher pressure creates more plasma, which explain why the blue shift is increasing with pressure (Fig.45).
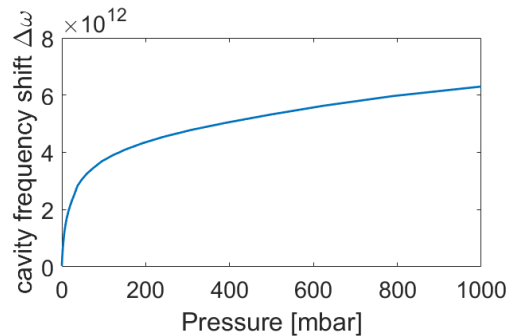

Figure 45: Pressure dependence of the blue shift in the cavity. Seed pulse $300\,\text{nJ}$

Cavity line shapes

It has also been observed that we can optimize the pulse energy by adjusting the detuning $\Delta\nu$, defined as:

$$\Delta\nu = f_{\text{laser}} - f_{\text{cavity}} \tag{70}$$

While the laser frequency is not easy to adjust, the cavity frequency can be easily controlled with a PZT by modifying the cavity length : $f_{\text{cavity}} = c/L$. As emphasized in Fig.46, a non zero detuning can leads to a better pule energy.
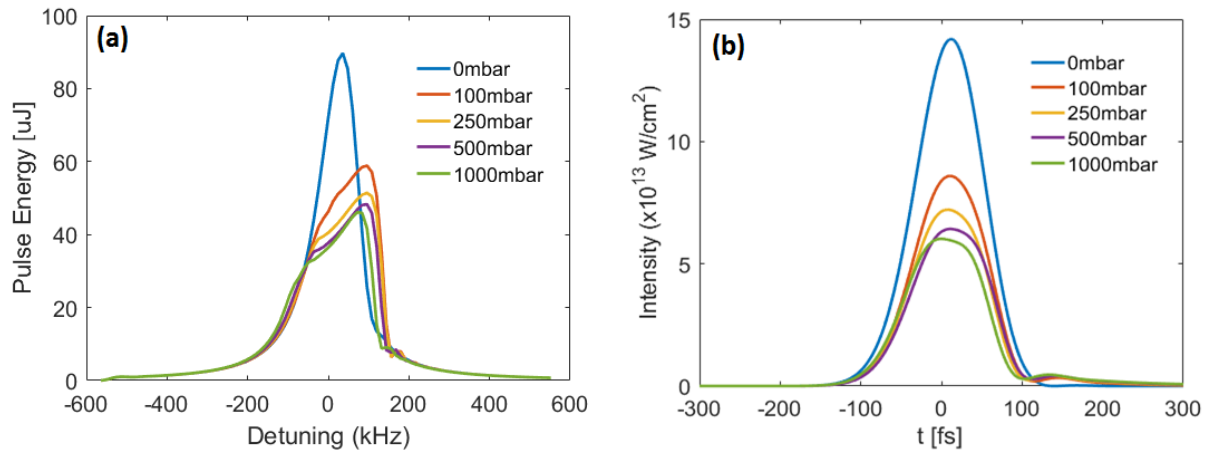
Figure 46: (a) Pulse Energy as a function of detuning and (b) pulse temporal shape at optimum detuning for different pressure. Seed pulse $= 500\,\text{nJ}$, $\omega_o = 19.6\,\mu\text{m}$, $\lambda = 800\,\text{nm}$, $f = 60\,\text{MHz}$, $l_p = 150\,\mu\text{m}$, Krypton.

When gas is introduced at the cavity focus, the lineshape becomes strongly distorted depending on the degree of ionization and the fsEC parameters, a change in the pulse shape is also noticed. We use in the experiment a method of active stabilization which lead to a locking at the peak of the line shapes, and no further manual shift is necessary to adjust the optimum detuning.

IV.3   Measurements & Simulations

Intensity dependence

Measurements of the harmonic power have been performed as a function of cavity transmission. The intracavity power is given from the calibrated cavity transmission: $P_{\text{Cav}} = K \times P_{\text{trans}}$, where the calibration constant was measured to be $K \approx 1.1 \times 10^5$. The corresponding peak intensity can then be calculated with $I_o = 2.0 \times 10^{13} P_{\text{Cav}}$ (details explained in A.2).
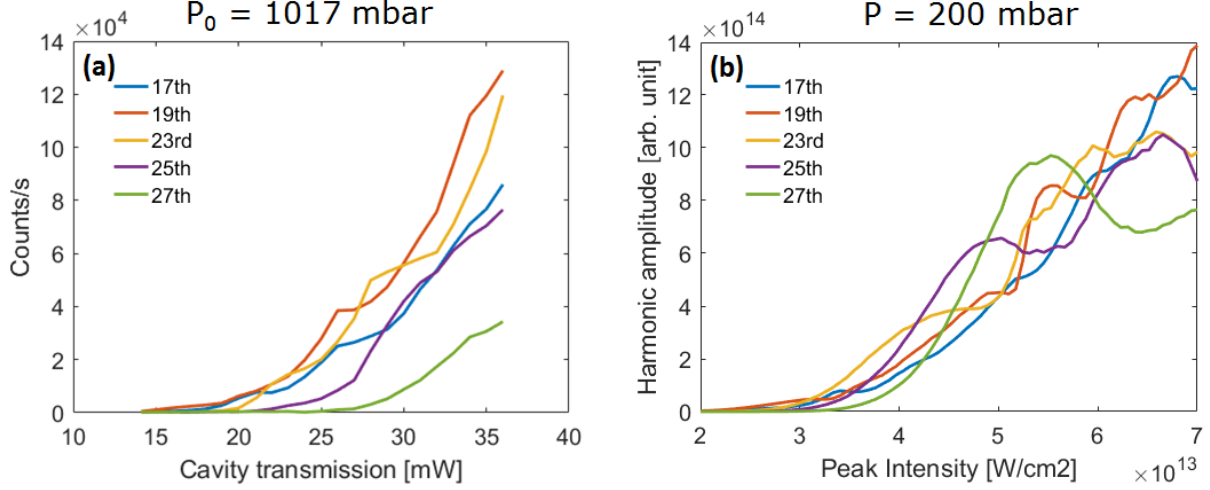

Figure 47: (a) Measured harmonic power as a function of cavity transmission with Krypton (backing pressure $P_0 = 1017\,\text{mbar}$) and (b) simulated Harmonic amplitude as a function of intensity. The simulation is computed with $P = 200\,\text{mbar}$, $t_p = 130\,\text{fs}$, $\lambda = 1050\,\text{nm}$, $\omega_o = 19.6\,\mu\text{m}$, $l_p = 150\,\text{nm}$, $f = 60\,\text{MHz}$, $V = 250\,\text{m/s}$, Krypton.

The simulation is run with a pressure P around 5 times smaller than the backing pressure P_0 because there is a pressure drop at the nozzle outlet (explained in II.3.1). Both simulations and measurements show a general increasing of the harmonic power as we ramp up the intensity, and also strong oscillations in the relative amplitude of the harmonics. However oscillations are very different between simulations and measurements, it can be explained by the instability of the phasematching and absorption, that can significantly change for a small change in the pressure (which can not be precisely determined).

However the 27th harmonic has a lower power than other harmonics in the measurements whereas it is in the same range of power in the simulation results. This is not understood and it may come from a mistake in the atomic response code.

Pressure dependence

Because of experimental problems, we haven't been able to measure the harmonic amplitude as a function of pressure, thus we will use instead measurement from [5] to compare with our simulations.
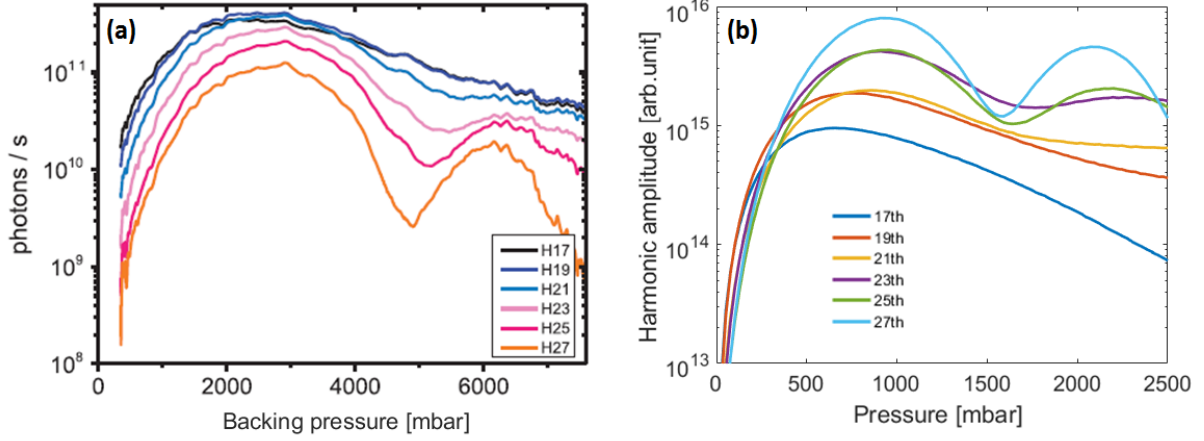

Figure 48: (a) Measured harmonic power as a function of backing pressure [5]. (b) Simulated Harmonic amplitude as a function of pressure, $I_o = 1.4 \times 10^{14}\,\mathrm{W/cm^2}$, $t_p = 8\,\mathrm{fs}$, $\lambda = 820\,\mathrm{nm}$, $l_p = 150\,\mathrm{nm}$, $\omega_o = 15\,\mathrm{\mu m}$, $f = 150\,\mathrm{kHz}$, Krypton.

As discussed in II.3.1, to have a good match with the measurements, we take a pressure 3 times smaller than the backing pressure. The simulations are overall in good agreements with the measurements, particularly concerning the oscillations of the curves, which depends on each harmonic. However, the differences in the relative harmonic amplitude is not understood, indeed according to the dipole code, at $I_o = 1.4 \times 10^{14}\,\mathrm{W/cm^2}$, the dipole response should be saturated and therefore nearly the same for all harmonics, and as emphasized in the simulations, the low absorption of the highest harmonics should makes them brighter than lower harmonics.

IV.4 Optimazing the outpout

IV.4.1 Mixing with helium

Mixing with helium

As described in II.3.2, the gas velocity can play a key role in the phase matching. So it has been suggested to mix the noble gas with Helium to increase the gas velocity [13, 49] (it has been reported in [49] that a mixture of helium and xenon can lead to an increase in harmonic yield of 30% over a pure xenon target). This paragraph investigate how to optimize the harmonic output by mixing the noble gas with Helium.

Given a mixture of pressure P_{tot} composed of a fraction x of Helium and $(1-x)$ of Krypton, we can calculated the mixture velocity and partial pressure with a linear law:

$$P_{\text{Kr}} = P_{\text{tot}}(1-x) \quad \text{and} \quad P_{\text{He}} = P_{\text{tot}}x$$
$$V_{\text{mix}} = xV_{\text{He}} + (1-x)V_{\text{Kr}} \tag{71}$$

Once we know the velocity of our mixture, we can determine the ionization fraction using the graph Fig.23 in II.3.2. However, besides the benefits of the gas velocity increasing, mixing with helium will have other impacts on the HHG process. Indeed the first thing to consider is that while Helium doesn't participate to the harmonic generation process, it can still absorb the generated harmonics. Fig.49 plot the absorption coefficient of Krypton and Helium. For the 21st harmonic, absorption is 4 times lower for Helium than Krypton, which means that the impact of Helium on the absorption is not negligible.
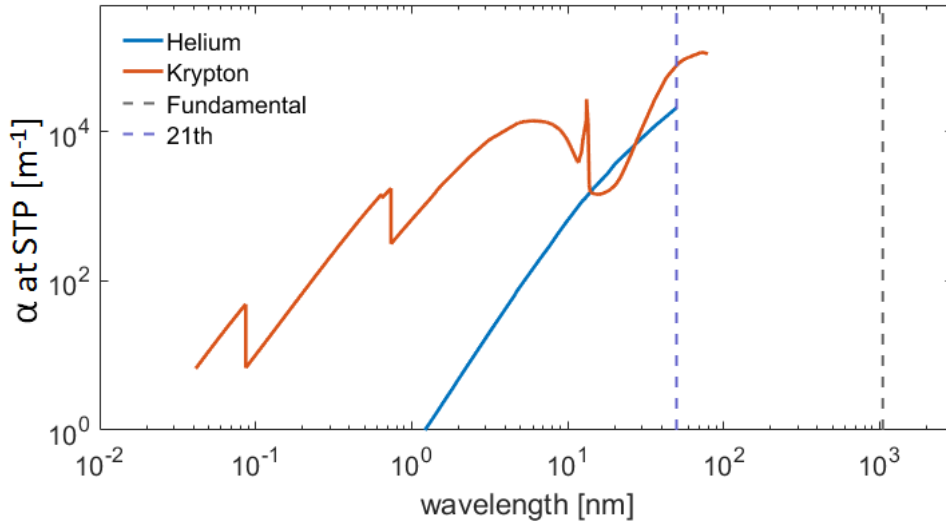
Figure 49: Absorption coefficient of Helium and Krypton at STP [15]. For the 21st harmonic, the absorption is around 4 times lower for Helium than Krypton.

The second thing to consider is the refractive index modification by Helium, with the same reasoning as in I.4.1, the refractive index is deviated from unity by He atoms following:

$$\delta(z,r,\omega) \approx \frac{P_{\text{tot}}(z,r)}{P_{atm}} \, x \, \delta_{\text{He}}(\omega) \tag{72}$$

The last thing to consider is that Helium atoms can also be ionized by the driving field and therefore modify the phasematching. However, as the ionization potential of Helium $(24.6\,\mathrm{eV})$ is much higher than Krypton $(14.0\,\mathrm{eV})$, the required intensity to ionize He atoms is above the intensities we are working with. Thus we can consider that Helium will not have any influence on the ionization fraction.

Given these considerations, we can plot the harmonic amplitude at optimum pressure as a function of helium fraction (Fig.50).
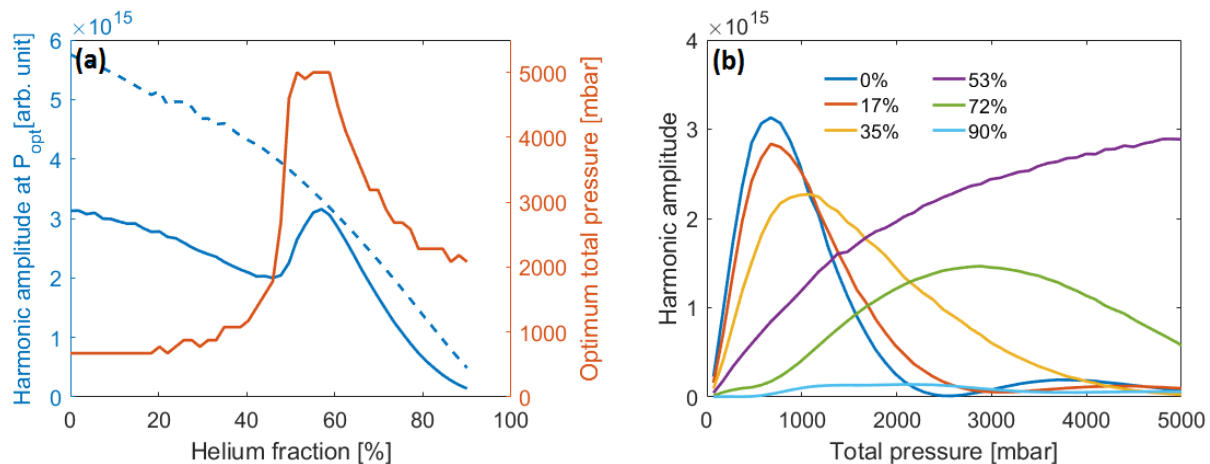

Figure 50:   (a) Optimum harmonic amplitude as a function of helium fraction and (b) Harmonic amplitude as a function of pressure for different helium fraction.   The dashed line plot the harmonic amplitude for perfect phase matching. $I_o = 7 \times 10^{13}\,\mathrm{W/cm^2}, t_p = 130\,\mathrm{fs}, l_p = 150\,\mathrm{nm}$, Krypton.

From the figure we notice that even though the gas velocity is increasing, the phase matching does not significantly change as we increase the helium fraction (as the ratio between dashed line and solid line is roughly constant for low helium fraction), the improvements in the phase matching around $x_{\mathrm{He}} = 50\,\%$ is caused by the refractive index modification by helium atoms, but require very high pressure (up to 5 bar), the absorption of helium also considerably reduce the harmonic output amplitude. However the simulation has been run with a constant intensity, and the increasing in the gas velocity would lead to a reducing of the plasma density and thus increase the cavity steady intensity. Therefore it is not possible at the moment to claim if the helium fraction would improve the maximum harmonic power or not.

IV.4.2   Changing the nozzle

Square vs. Gaussian density profile

For a gaussian density profile, the pressure is changing along the axis, which creates significant variation in the phase matching through the interaction region. On the other hand, for the square profile, the pressure is constant along the axis, and so the phase matching varies much less. In the end, we notice that the phase matching plateau (see III.2.2) is much longer for the square density profile.
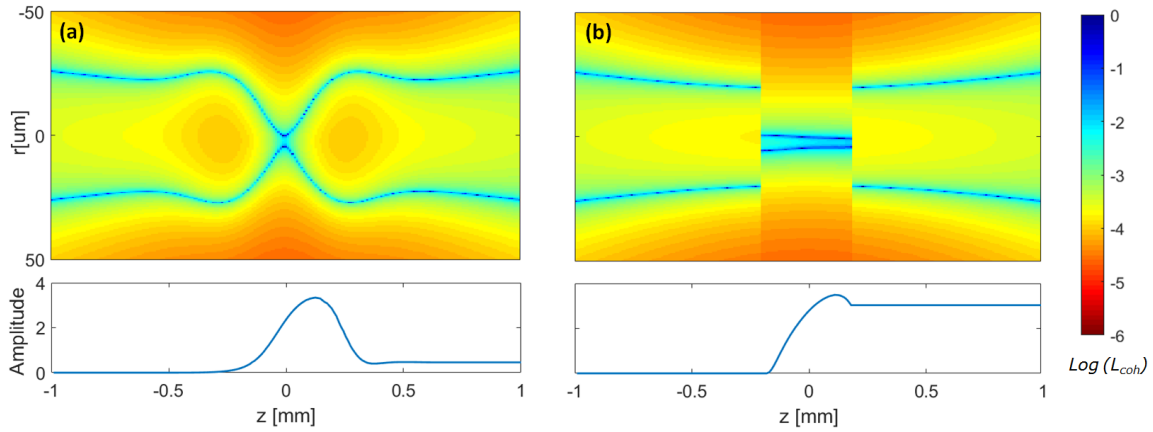

Figure 51: Phase-matching configuration (coherence length) for a (a)gaussian and (b)square density profile. The phase matching at the focus is the same but as we move away from the focus, the phase matching is getting bad for the gaussian profile whereas it remains good for the square profile. $I_o = 6 \times 10^{13}\,\mathrm{W/cm^2}$, $t_p = 130\,\mathrm{fs}$, $P = 320\,\mathrm{mbar}$, $l_p = 400\,\mathrm{\mu m}$, $V = 250\,\mathrm{m/s}$, Krypton.

From the last figure we can tell that an increasing of the interaction length will not have the same consequences on the harmonic output. The Fig.52 plot the harmonic amplitude at optimum pressure as a function of the interaction length for square and gaussian profile. While having the shortest possible interaction length is the best solution for gaussian profile, having the largest interaction length is the best for the square profile.
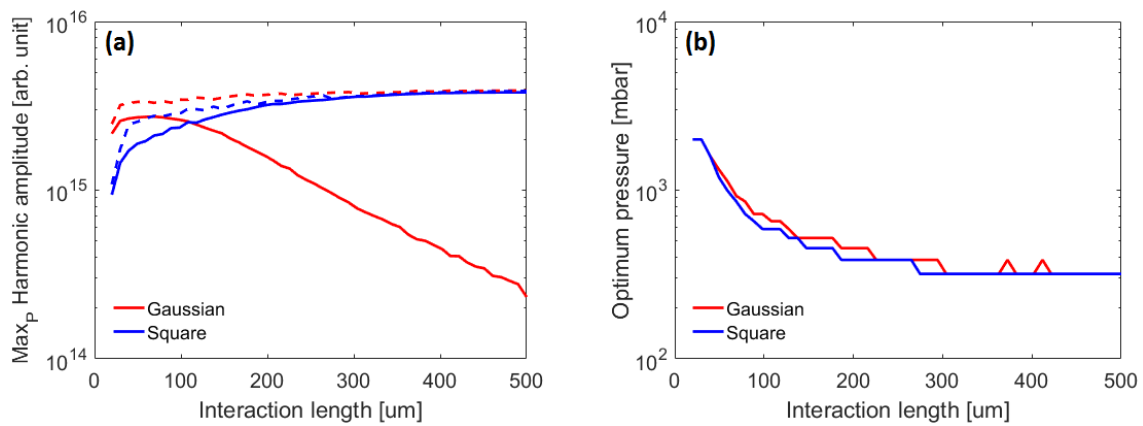

Figure 52: (a) Maximum Harnonic amplitude and (b) optimum pressure as a function of the interaction length for square and gaussian density profile. The dashed lines represent the harmonic output for a perfect phase-matching to highlight the limitations due to absorption. $I_o = 6 \times 10^{13}\,\mathrm{W/cm^2}$, $t_p = 130\,\mathrm{fs}$, $V = 250\,\mathrm{m/s}$, Krypton.

A longer interaction length involve a lower optimum pressure which is good because higher pressure cause more experimental challenges. More detailed studies showed that the square density profile would generally improve the harmonic amplitude in most of the configurations, and also increase the maximum reachable harmonic output by a factor of 2.

The dynamic nozzle

Since it has been demonstrated that the interaction length can play a key role in the high harmonic generation process, a new nozzle design has been suggested using a buffer gas to confine the noble gas in a precisely tunable interaction region (inspired from [50]). This nozzle would enable interaction region smaller than $100\,\mu m$, which cannot be achievable with a basic endfire nozzle, and also deliver a square density profile.
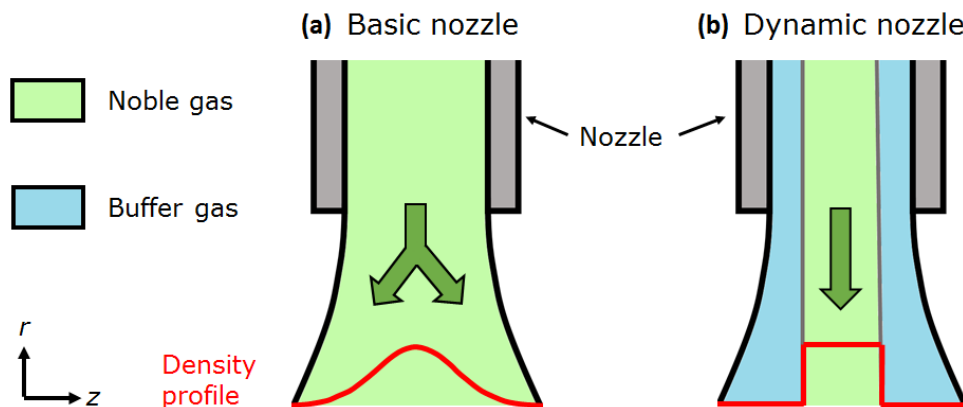
Figure 53: Design of a (a) basic end fire nozzle and (b) dynamic nozzle. The buffer gas has to be lighter and faster than the noble gas, typically helium. The basic nozzle leads to a gaussian density profile because of the spreading whereas the dynamic nozzle deliver a square profile thanks to the buffer gas confinement.

The dynamic nozzle relies on a buffer gas on the periphery, which confine the noble gas in a smaller interaction region. This nozzle can work only if the buffer gas has a negligible absorption so it wont absorb the harmonics. The resulting density profile is square because two different supersonic gas don't mix. A detailed study of the dynamic nozzle with *COMSOL* is presented in C.1.

V   Conclusion & Perspectives

In this thesis, a complete study of the HHG process is presented. The plasma cloud behavior between each pulse as well as the atomic response have been successfully simulated, and the consequences of the phase matching effects and absorption have also been demonstrated. The Harmonics amplitude has been calculated as a function of intensity, pressure, interaction length and nozzle position, and the optimum parameters have been highlighted considering absorption and phasematching limitation (III.3.2). The accuracy of the numerical simulations has been confirmed with measurements and scientific publications.

It has been simulated that the improvements that we can make in the cavity power by mixing the gas with helium is counterbalanced by a reducing in the harmonic output due to the helium absorption. It may be possible to reduce absorption effects by using a different gas, however all the gases have too high absorption except Hydrogen, which is experimentally challenging and dangerous to use for its flammability.
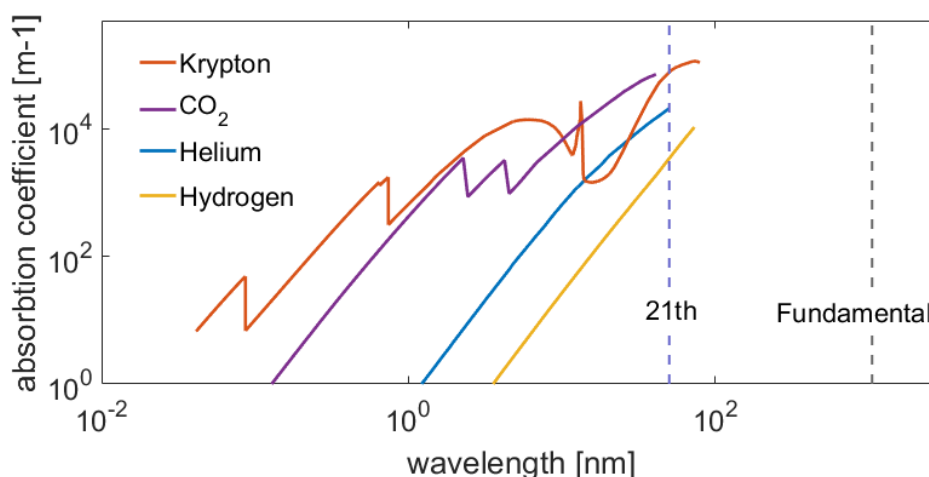
Figure 54: Absorption coefficient at STP as a function of wavelength for Krypton, Helium, Hydrogen and CO_2, calculated from Xray data base [15]. For the 21st harmonic, the absorption of Helium is 4 times smaller than Krypton whereas the one of hydrogen is 25 times smaller.

However, the construction of a dynamic nozzle would significantly improve the phase matching at the laser focus and thus improve the harmonic amplitude output, it would also enable a precise tuning of the interaction length, which nowadays requires to change the nozzle diameter. This new nozzle would improve the HHG source for photoemisson spectroscopy and would make it a better alternative to the synchrotron light sources.

A   Complements on the experiments

A.1   Harmonic diffraction on the grating mirror

When the laser light is reflected on the grating mirror (GM), all the harmonics are diffracted with a different angle following the relation:

$$\sin\theta_i + \sin\theta_d = \frac{m\lambda_q}{d} \tag{73}$$

θ_d is the incidence angle, 70° in our setup

d is the grating period, 200 nm in our setup

θ_d is the diffracted angle

m is the diffraction order

$\lambda_q = \frac{\lambda_1}{q}$ is the harmonic wavelength

We can calculate the mth order diffraction angle of all harmonics with:

$$\theta_d = \arcsin\left(\frac{m\lambda_1}{qd} - \sin\theta_i\right) \tag{74}$$

Each harmonics are projected on a metal plate placed perpendicular to a reference harmonic q_{ref} at a distance of $L = 10\,\text{cm}$ of the GM. The diffraction angle of the $q_{\text{ref}}^{\text{th}}$ harmonic being θ_{ref}, the position x of each harmonic on the plate can be calculated ($x = 0$ being the position of the $q_{\text{ref}}^{\text{th}}$ harmonic):

$$x_q = L\tan(\theta_{\text{ref}} - |\theta_q|) \tag{75}$$

We can now plot the position of each dot as a function of wavelength and harmonic, the position on the plate is not linear with the wavelength:
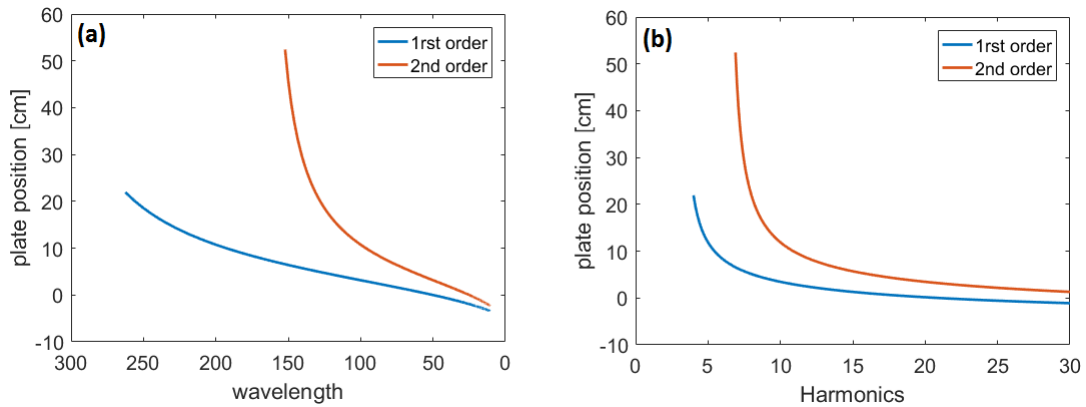
Figure 55: Dot position on the plate as a function of (a) wavelength and (b) harmonic order. The plate is placed perpendicular to the 21st harmonic. $\lambda = 1050\,\text{nm}$, Krypton.

Fig.56 clearly emphasize the diffracted harmonics H5 to H29 up to the 6th order. The harmonics H5 and H7 are the brightest because they are superposed with 3rd and 5th order of higher harmonics (H5 : 3rd order H15 and 5th order H25, H7: 3rd order H21). The harmonic H29 being too weak, its 5th and 6th diffracted order are not visible on the plate.

Figure 56: Photo of sodium salicylate phosphor illuminated by harmonics 5th-29th and the corresponding diffraction order for each dot on the plate. The plate is placed perpendicular to the 9th harmonic ($\theta_{9th} = 21°$). $\lambda = 1050\,\text{nm}$, Krypton.
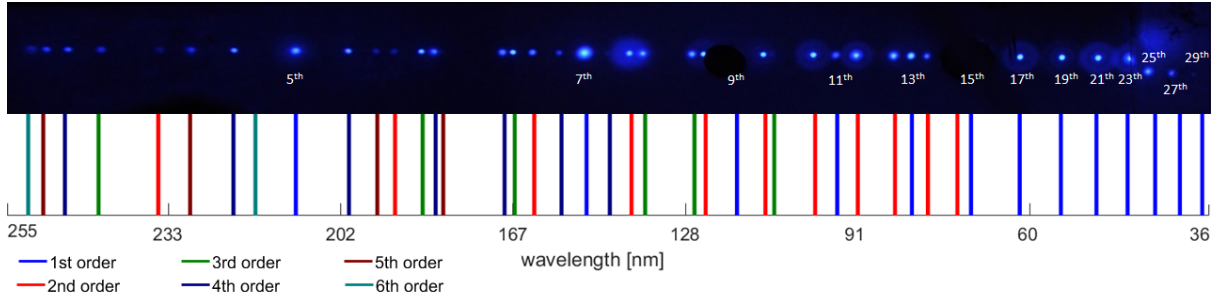
A.2   Av. power to Intensity

We calculate in this section the relation between the peak intensity I_o and the average power P_L of a pulsed laser. Let's consider a laser of frequency f, pulse length t_p and beam radius ω_o.

To do that, we look into a single laser pulse, define the energy of a pulse $E_{\text{pulse}} = P_L/f$ and calculate the peak power P_{peak} by:

- Integration of the pulse power envelope over time:

$$E_{\text{pulse}} = P_{\text{peak}} \int_{-\infty}^{\infty} f(t)\, dt \tag{76}$$

- Integration of the beam intensity over a section perpendicular to the propagation direction:

$$P_{\text{peak}} = \iint_{-\infty}^{\infty} I(r,0)\, dr^2 \tag{77}$$

For a gaussian beam with a gaussian envelope, we get:

$$P_{\text{peak}} = E_{\text{pulse}} \frac{2\sqrt{\ln(2)}}{t_p\sqrt{\pi}} = I_o \frac{\omega_o^2 \pi}{2} \tag{78}$$

We can finally write:

$$\boxed{I_o = P_L \frac{\sqrt{\ln(2)}}{\omega_o^2 t_p f} 4\pi^{-3/2}} \tag{79}$$

In our experiment, $f = 60\,\text{MHz}$, $t_p = 130\,\text{fs}$, $\omega_o = 19.6\,\text{µm}$, which gives in SI units:

$$I_o = 2.0 \times 10^{14} P_L \tag{80}$$

We usually work with P in kW and I_o in W/cm^2, so the relation becomes:

$$\boxed{I_o = 2.0 \times 10^{13} P_L} \tag{81}$$

B Complements on High Harmonic Generation

B.1 Dipole moment and Ehrenfest's theorem

Having the TDSE solved, in this section we describe the harmonic amplitude calculation using the dipole moment, more details in [37, 38, 39]. The easiest way to calculate the dipole response is to use the length dipole moment:

$$d(t) \propto \langle \psi(x,t) \, |x| \, \psi(x,t) \rangle \tag{82}$$

The corresponding power spectrum can be obtained by the Fourier transformation of the time dependent dipole moment:

$$P(\omega) = \left| \frac{1}{T_f - T_i} \int_{T_i}^{T_f} d(t) e^{-i\omega t} \, dt \right|^2 \tag{83}$$

However there is a different way to calculate the dipole power spectrum using the acceleration of the dipole moment:

$$d_A(t) \propto \left\langle \psi(x,t) \left| -\frac{\mathrm{d}^2 x}{\mathrm{d}t^2} \right| \psi(x,t) \right\rangle \tag{84}$$

According to Ehrenfest's theorem, it can also be written as:

$$d_A(t) \propto \left\langle \psi(x,t) \left| -\frac{\partial V(x,t)}{\partial x} \right| \psi(x,t) \right\rangle \tag{85}$$

The acceleration power spectrum is then calculated with:

$$P_A(\omega) = \left| \frac{1}{T_f - T_i} \frac{1}{\omega^2} \int_{T_i}^{T_f} d_A(t) e^{-i\omega t} \, dt \right|^2 \tag{86}$$

The power spectra $P(\omega)$ and $P_A(\omega)$ should be the same if the wavefunction $\psi(x,t)$ is fully converged. However, as shown in Fig.57, it has been demonstrated that calculation with the acceleration dipole moment gives better result [9], which is why we use it in our work (III.1).
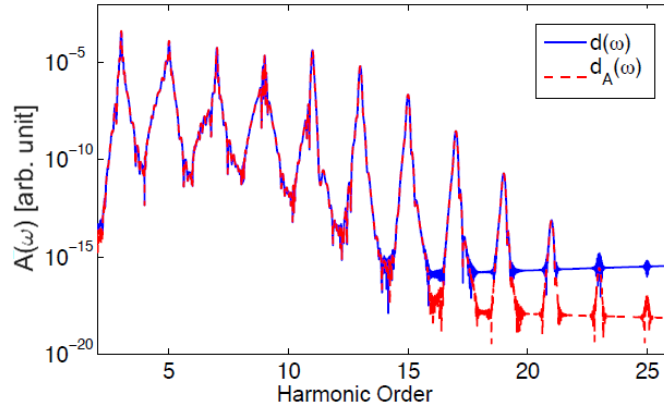

Figure 57: Comparison of the length (blue) and acceleration (red, dashed) form for calculating the dipole response ($I = 3 \times 10^{13} \, \mathrm{W/cm^2}$, $t_p = 70 \, \mathrm{fs}$, Xenon). Both forms give nearly identical results until well above the cutoff harmonic, from [9].

B.2   Boundary conditions in the TDSE code

The absorption potential

To ensure that the electrons do not reflect from the boundary, we use absorbing boundary conditions to remove energetic electrons that never return to the parent atom. Quantum absorption can be reasonable modeled by adding a negative imaginary absorbing potential [51, 52]: $-iV_a(x)$ to the Hamiltonian.

In our work we use the following absorption potential (only after the boundaries):

$$\begin{aligned} \text{for } |x| \leq x_{\text{cut}} \qquad & V_a(x) = 0 \\ \text{for } |x| > x_{\text{cut}} \qquad & V_a(x) = k \times (|x| + x_{\text{cut}})^2 \end{aligned} \qquad (87)$$

- x_{cut} is the boundary of our system, taken as: $x_{\text{cut}} = \frac{E_o}{\omega_1^2}$ (in a.u.)

- k (taken as 5×10^{-4} in our work) is the strength of the potential, a higher k will lead to a faster absorption but more reflection.

The influence of x_{cut}

In Fig.58 we plot the harmonic spectra and the dipole amplitude as a function of intensity for different values of x_{cut}.
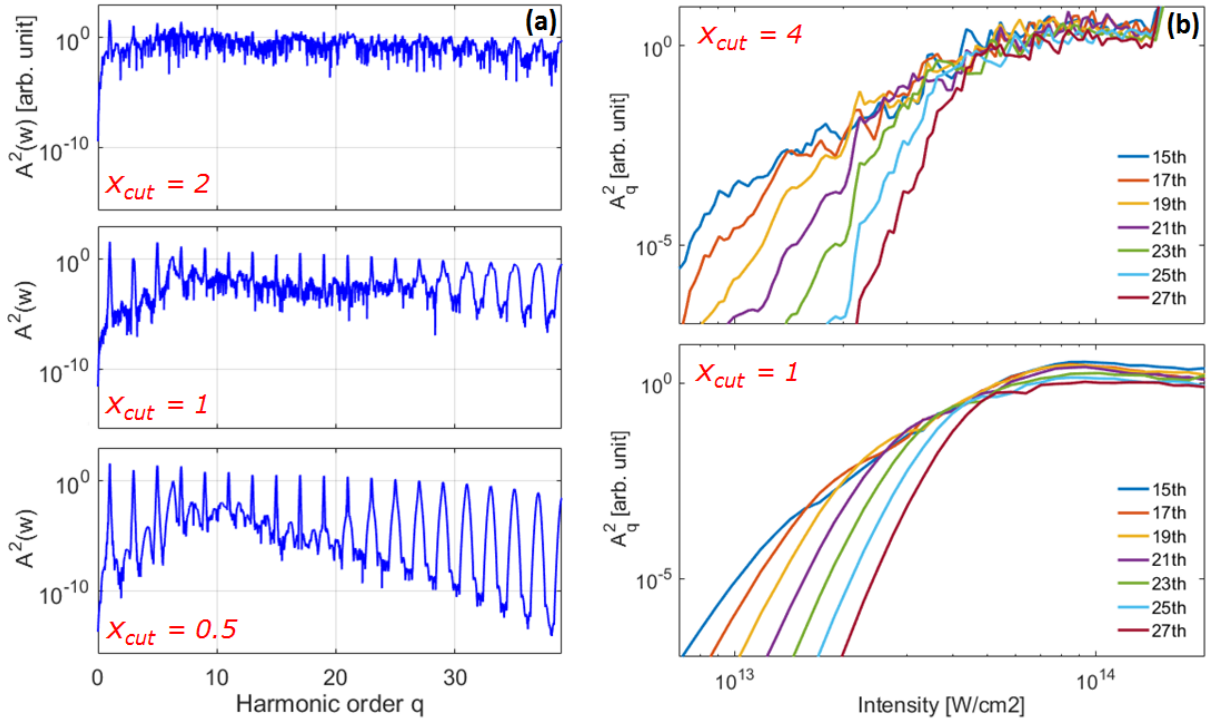

Figure 58: (a) Harmonic spectra and (b) dipole amplitude as a function of intensity for different x_{cut} (in unit of E_o/ω_1^2). $I_o = 1 \times 10^{14}\,\text{W/cm}^2$, $t_p = 130\,\text{fs}$, Krypton.

From the figure we notice that a high value of x_{cut} creates a bad harmonic spectrum and an irrelevant intensity dependence plot. It is because the long and short trajectories have different phase coefficients (I.1.2), and as we ramp up the intensity, they interfere. This would explain why there is strong oscillations with a periodicity about $8 \times 10^{12}\,\text{W/cm}^2$ in the intensity dependence plot. However, because the interferences are visible only for high x_{cut}, it seems that decreasing x_{cut} decreases the amplitude of one of the trajectories.

Short-time Fourier transform

The short-time Fourier transform (STFT) is useful to determine the sinusoidal frequency and phase content of local sections of a signal, it is generally defined as:

$$\mathbf{STFT}\{s(t)\}(\tau, \omega) = \int_{-\infty}^{\infty} s(t)w(t-\tau)e^{-i\omega t}\,dt \tag{88}$$

Where $s(t)$ is the signal to be transformed and $w(t)$ is the window function, commonly a Hamming window. In our case, we are interrested in the short time fourier transform of a specific window of the spectrum [10], to deduce the time dependant dipole moment from a spectrum window centered in Ω, we use:

$$d_w(t) = \int_{-\infty}^{\infty} A(\omega)w(\omega - \Omega)e^{i\omega t}\,d\omega \tag{89}$$

The Fig.59 plot the STFT of the harmonic spectrum in the window $[q = 19 : q = 25]$ for different values of x_{cut}
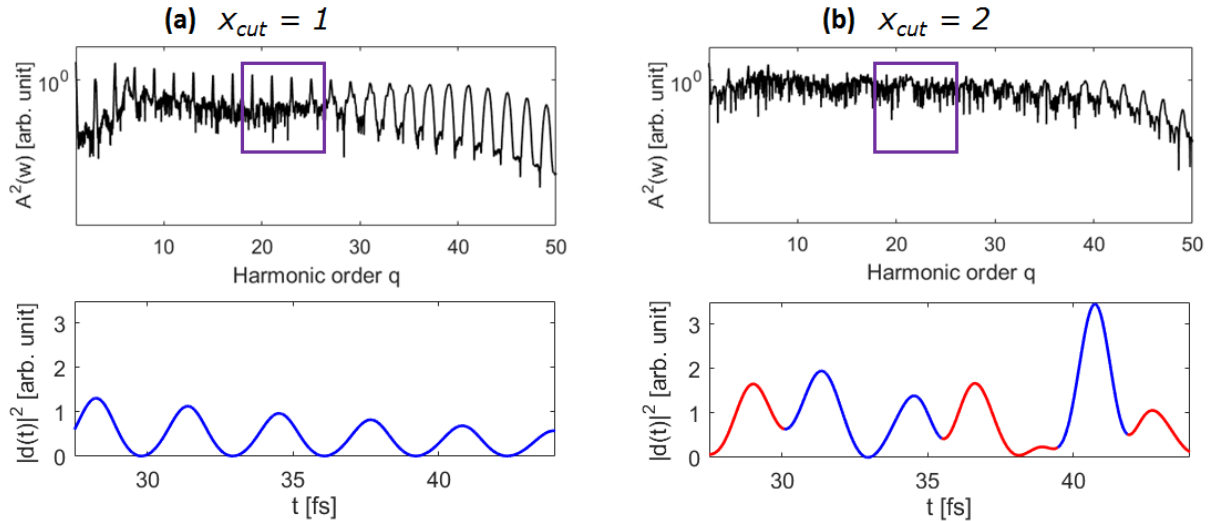
Figure 59: STFT of the harmonic spectra in the window [19th 25th] for (a) $x_{\text{cut}} = 1$ and (b) $x_{\text{cut}} = 2$ (in unit of E_o/ω_1^2). In the STFT Fig.b, The radiation consists of two trains of overlapping pulses, one each from the short (blue) and long (red) quantum paths, which are shown in different shades for clarity. In Fig.a, only the short trajectory is visible, the overall amplitude is decreasing because the driving field intensity (gaussian) is decreasing. $I_o = 1 \times 10^{14}\,\text{W/cm}^2$, $t_p = 130\,\text{fs}$, Krypton.

For $x_{\text{cut}} = 2E_o/\omega_1^2$, when we look at the STFT of the harmonic spectrum, we see that the short and long trajectories have about the same amplitude. As we decrease x_{cut}, we notice that the order of magnitude of the short trajectory remain unchanged, but the long amplitude trajectory decrease and eventually become negligible. Decreasing x_{cut} enables to delete interference between the two quantum path.

If we look into Eq. 4, and try it for different ionization time t_0, we will notice that the farthest trajectories are born before 18 degrees. So the long quantum path has a longer trajectory (in time) than the short one, but it goes farther away from the atom (travels a longer distance). Which means that long trajectories electron will be more likely to reach above the absorption boundaries, and will stay there longer. This classical model explain well why the the long trajectory electrons are absorbed while the short quantum paths remain unchanged.

B.3   HHG described by the TDSE

In this section we use the TDSE to take a closer look into the HHG process. After having the electron wavefunction $\psi(x,t)$ calculated in III.1, we can project it to the ground state electron wavefunction $\psi_o = \psi(x,0)$. The probability that a given electron is in the ground state at time t is then given by $p(t) = |\langle \psi_o | \psi(x,t) \rangle|^2$.

Fig.60 plot the electron wavefunction and the ground state probability as a function of time, the pulse length is taken low (10 fs) to make laser cycles clearly visible. From the figure we notice strong oscillations in the probability evolution, a decreasing in the probability $p(t)$ indicates an increasing of the freed electron number whereas an increasing in the probability means that some electrons recombined with their parents atoms.
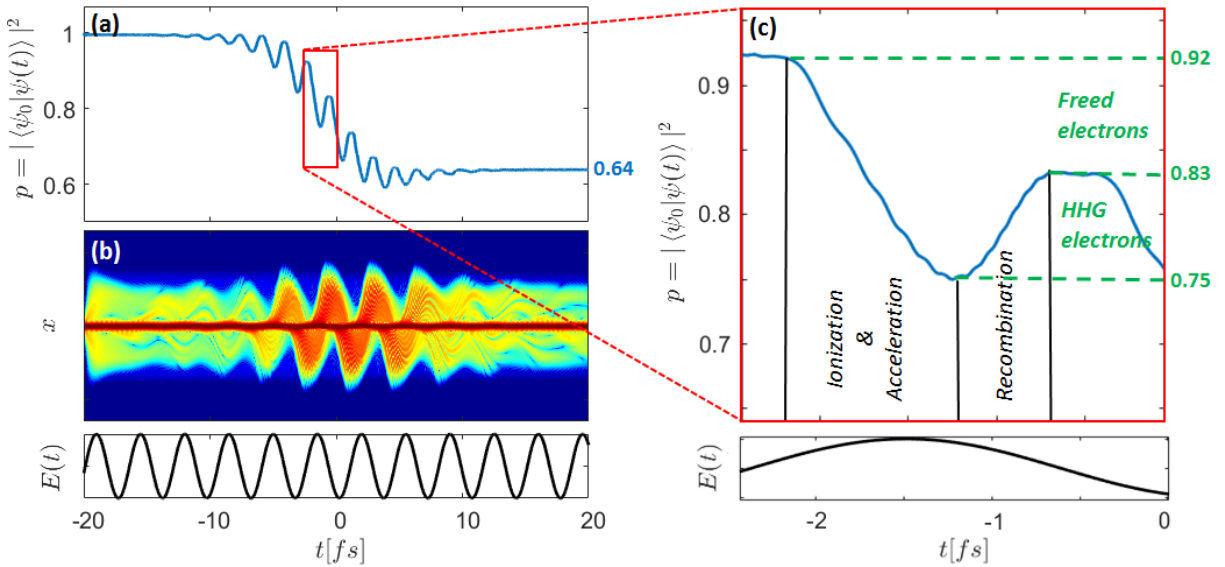

Figure 60: TDSE solution for a driving field peak intensity of $I_o = 1.3 \times 10^{14}\,\mathrm{W/cm^2}$ and a pulse length $t_p = 24\,\mathrm{fs}$. The electron wavefunction $\psi(x,t)$ is (b)plotted along t and x and (a)projected to the ground state electron wavefunction $\psi_o = \psi(x,0)$ to obtain the probability $p = |\langle \psi_o | \psi(x,t) \rangle|^2$. A (c)detailed laser half cycle is plotted to emphasize the 3 steps involved in the HHG process. The electric field $E(t)$ is also plotted for a better understanding.

To explain what happens during a laser cycle, we have to come back to the three step models described in I.1.1. When $|E(t)| > 0$, two phenomenon occurs:

- Some electron escape via quantum tunneling.

- Electrons which has escaped during the previous half laser cycle accelerate back toward their parent ions and some of them recombine (because the electric field has an opposite sign).
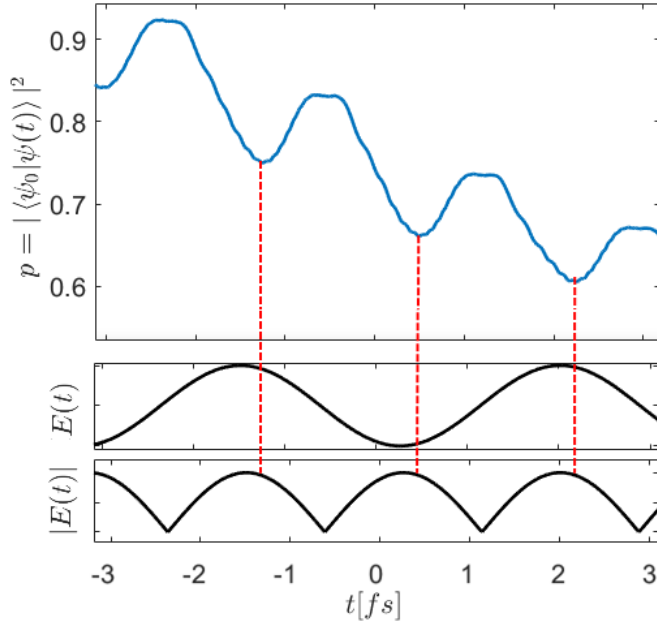
Figure 61: Time evolution of the probability p for two laser cycles. The driving field $E(t)$ is also plotted for a comparison tool. A wavefunction period correspond to a half laser cycle. The parameters are the same as the figure 60.

From the Fig.61 we can notice that a TDSE period correspond to a half laser cycle. Moreover, the Fig.61 and Fig.60(c) emphasize 3 regimes in the wavefunction evolution during a half laser cycle:

- $\frac{d|E(t)|}{dt} > 0$, ionization is the dominant process.

- $\frac{d|E(t)|}{dt} < 0$ and $|E(t)| < \frac{E_o}{2}$, recombination is the dominant process.

- $\frac{d|E(t)|}{dt} < 0$ and $|E(t)| > \frac{E_o}{2}$, there is as much ionization as recombination, so the probability remains the same.

It is now clear that after each half laser cycle, not all electrons recombine, and at the end of the pulse we are left with a plasma cloud. The ionization fraction in the end of the pulse can be majored from the TDES with $\eta \leq 1 - p(t_p)$, it depends on the pulse length and the driving field peak intensity. Note that it is not necessary equal since some electron will be excited but not freed by the drinving field. The Fig.62 plot the ionization fraction as a function of intensity and pulse length and compare it to the Ionization fraction obtained with the Yudin rate. The difference between the TDSE and Yudin rate comes from the excited electrons.
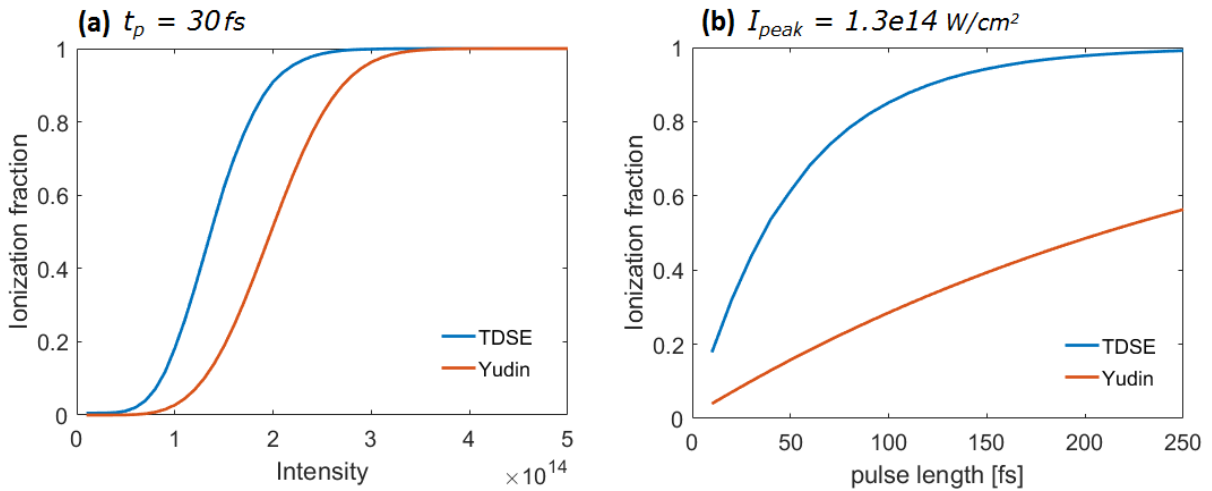

Figure 62: Ionization fraction calculated from Yudin and from the TDSE as a function of (a) intensity and (b) pulse length.

C   Complements on Gas dynamic

C.1   COMSOL simulation

Endfire nozzle

To have a good understanding of what happen at the nozzle outlet, numerical solvers are required. The computational fluid dynamics (CFD) module of *COMSOL Multiphysics* is used, it can accurately simulate the fluid mechanics in turbulent and compressible flow.

The nozzle design is shown Fig.63, a Krypton gas jet is injected at the inlet at backing pressure $P_0 \approx 1$ bar and temperature $T = 293K$, and the gas is then ejected in the vacuum chamber at pressure $P_{\text{vac}} \approx 1 \times 10^{-2}$ mbar. A "no slip" and thermal insulation boundaries condition are added on the internal walls of the nozzle.
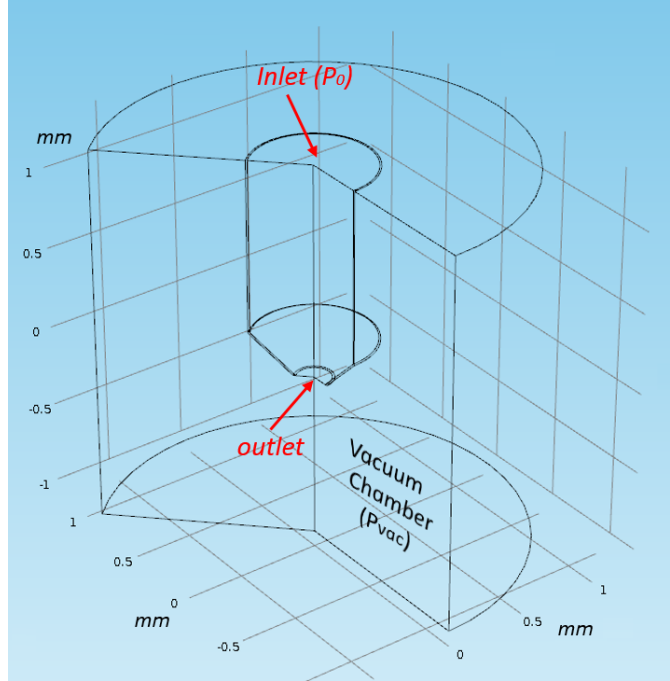
Figure 63: Endfire nozzle design, *COMSOL*.

Given the big difference in the order of magnitude between the backing and vacuum pressure, The theory predict that the gas will be supersonic and create of shock wave. The distance from the nozzle end to the shock wave is given by the mach disk, with d the outlet diameter [53]:

$$d_M \propto d \sqrt{\frac{P_0}{P_{\text{vac}}}} \tag{90}$$

Figure 64: Surface plot of the gas velocity $V[m/s]$, highlighting the supersonic gas shock wave propagation, *COMSOL*.

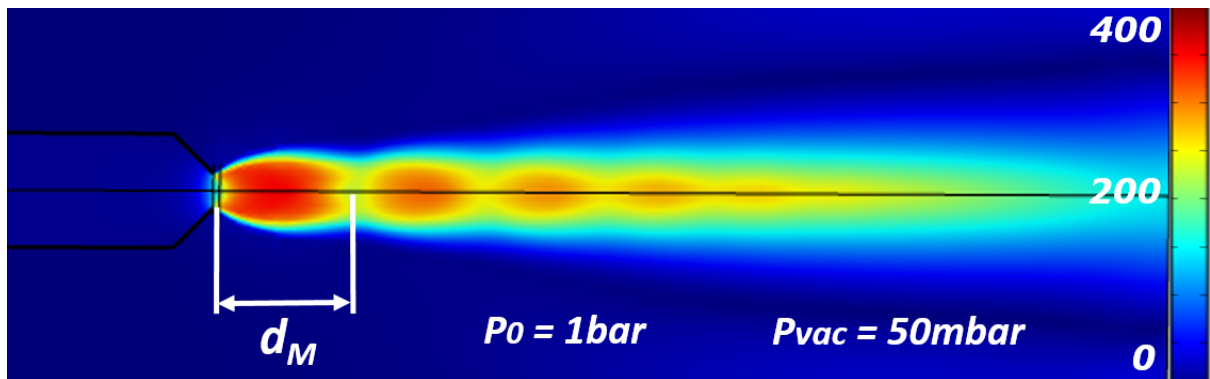If the difference in the order of magnitude of the pressures is too high, the CFD solver encounter convergence problems because the mach disk is too large, for this reason the following simulations will be done with $P_{\text{vac}} = 1\,\text{mbar}$. The computation is run for $d = 300\,\text{µm}$ and the results are plotted Fig.65.
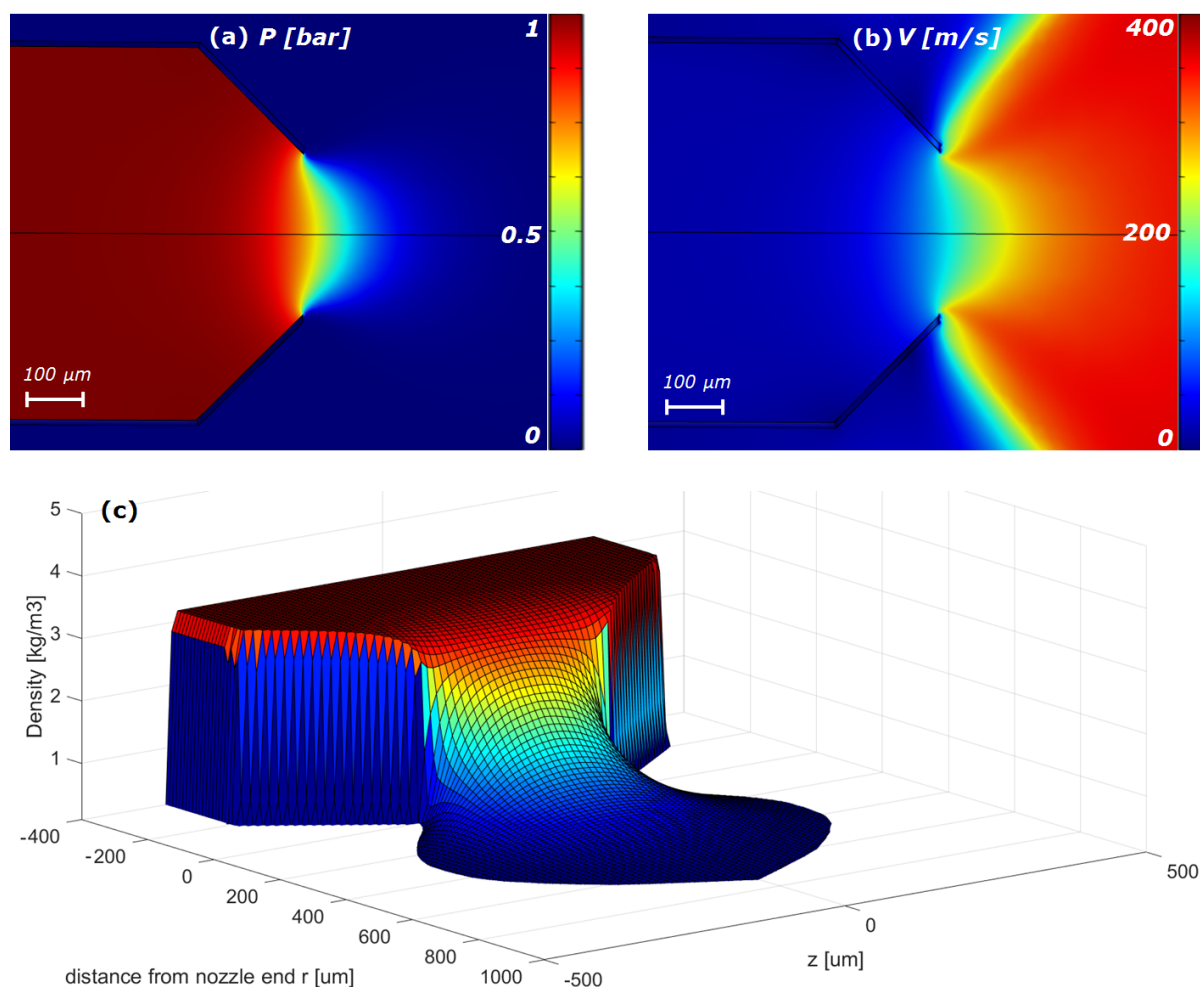
Figure 65: Surface plot of (a) the pressure, (b) the gas velocity and (c) the density near the nozzle outlet. $P_0 = 1\,\text{bar}$, $P_{\text{vac}} = 1\,\text{mbar}$, $d = 300\,\text{µm}$.

The simulations emphasise a fast pressure drop after the outlet, The density profile start from being square and tend to become gaussian after few $10\,\text{µm}$. To have a better understanding, we now run the simulation for different nozzle diameters and the results are plotted Fig.66. A smaller nozzle diameter leads to a faster drop, but the density profile stays the same (at a different scale). The gas velocity is not constant through the laser axis, and can increase up to two times the sound velocity.

Figure 66: (a) Density and (b) Velocity distribution on r and z axis for different nozzle diameter d, Krypton. The grey dashed line represent the $100\,\mu\mathrm{m}$ line and the sound velocity of Krypton at STP.
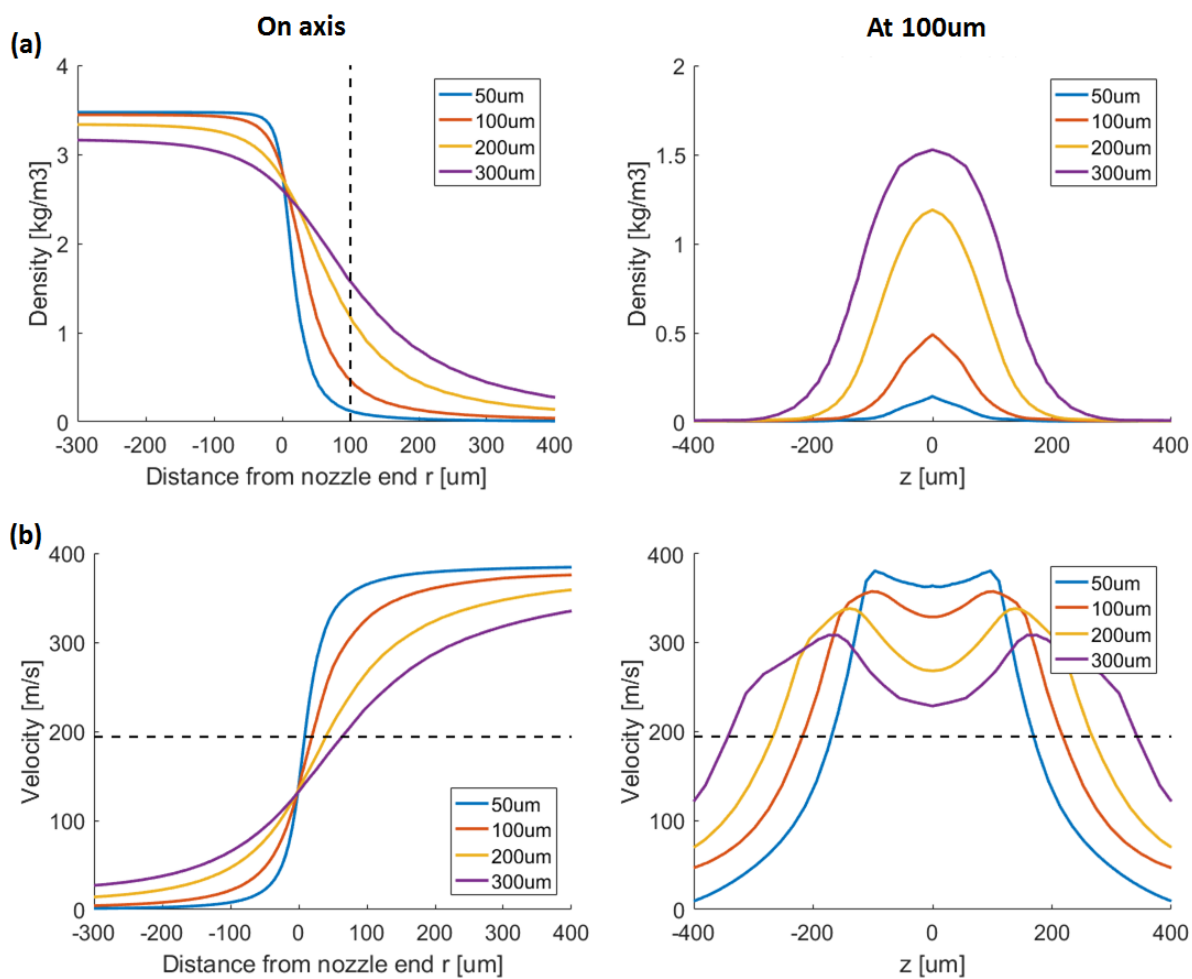
Dynamic nozzle

The dynamic nozzle is designed with two endfire nozzles nested into each other, contrary to the basic endfire nozzle studied in C.1, the dynamic nozzle has two inlets, the inner nozzle is filled with Krypton at pressure P_1 and the outer nozzle with Helium at pressure P_2. The inner nozzle width is set at $10\,\mu m$.

By controlling the pressure ratio P_1/P_2 between the two inlets, it will result a change in the velocity ratio V_1/V_2. And as emphasized in Fig.68, it allows us to adjust the krypton medium length after the nozzle outlet. In fact the interface Krypton-Helium is a curve which depends on the gas velocity:

$V_1 < V_2$ negative curvature
$V_1 = V_2$ straight line
$V_1 > V_2$ positive curvature
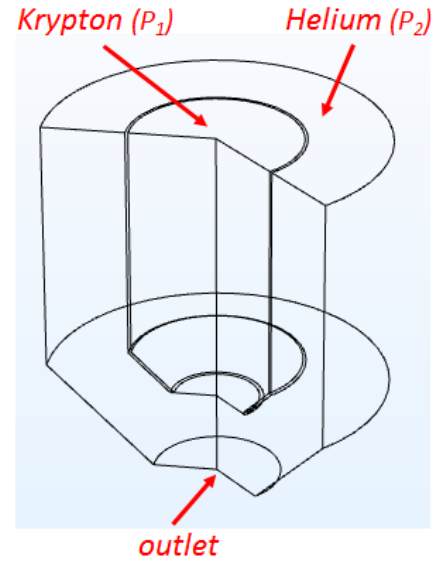
Figure 67: Dynamic nozzle design, *COMSOL*.
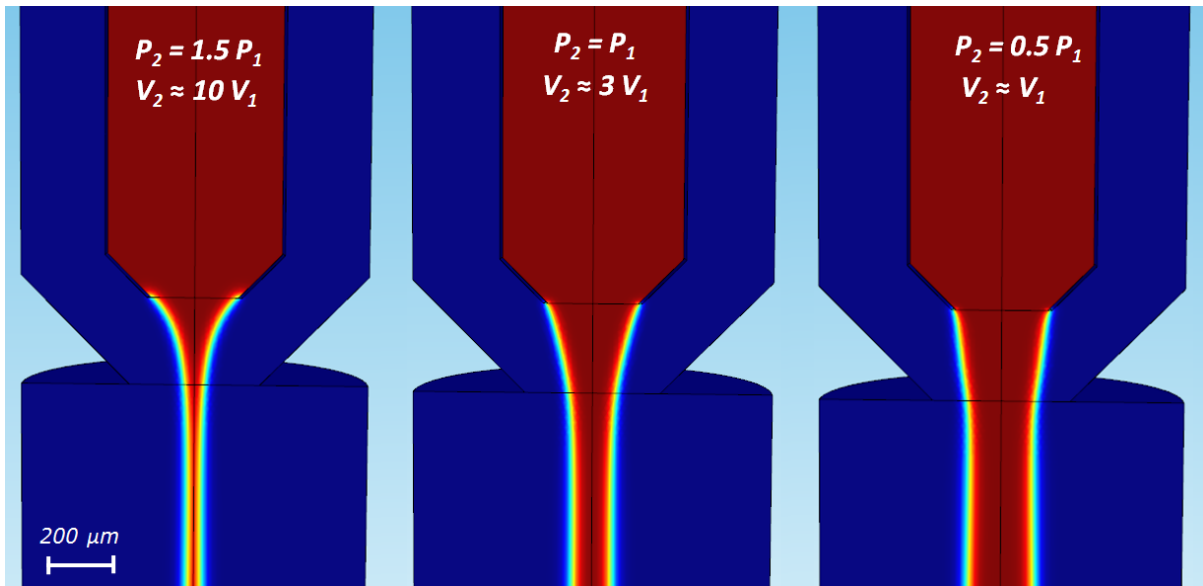
Figure 68: Volume fraction of Krypton for different inlet pressure ratio, $P_0 - P_{\text{vac}} = 20\,\text{Pa}$.

The *COMSOL* CFD module can not compute multiphase supersonic flows, so for this study we have to stay at low pressure gradient, otherwise the solver will not converge. Even though Krypton and Helium has very similar behavior when simulated on an endfire nozzle, we don't know how they interact with each other when they are supersonic. Thus we are not able to say if the the krypton density profile will be square or not.

Moreover, as discussed in IV.4.1, the helium absorption is not negligible and a significant part of the harmonics would be absorbed. A way to decrease the helium absorption would be reducing the Helium pressure, but then $V_1 \gg V_2$ and we don't know if the Krypton confinement would still work.

C.2   Complements on recombination

Ions recombination

In II.2.1 we describe the three body recombination rate in noble gas. However, depending on the environment, different types of recombination can occur [26], here we describe a few types of recombination previous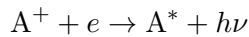ly observed in noble gases. There are many pathways for ions to decay with their own associated rates, ρ is the electron/ion density:

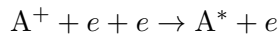- Collisional radiative recombination, this mechanism has three limiting forms:

    - Radiative recombination (occurs at low pressure and electron density)
        $$\mathrm{A}^+ + e \rightarrow \mathrm{A}^* + h\nu$$
        $$\Gamma_{\mathrm{RR}} = \rho \times 3\text{e-}16\ T_e^{-3/4}\ \mathrm{s}^{-1}$$
        $$\Gamma_{\mathrm{RR}}(\mathrm{STP}, 3\,\mathrm{eV}) = 3.2 \times 10^6\,\mathrm{s}^{-1}$$

    - Collisional recombination stabilized by an electron (occurs at high electron density)
        $$\mathrm{A}^+ + e + e \rightarrow \mathrm{A}^* + e$$
        $$\Gamma_{\mathrm{TBR},e} = \rho^2 \times 1.1\text{e-}20\ T_e^{-9/2}\ \mathrm{s}^{-1}$$
        $$\Gamma_{\mathrm{TBR},e}(\mathrm{STP}, 3\,\mathrm{eV}) = 2.9 \times 10^{10}\,\mathrm{s}^{-1}$$

    - Collisional recombination stabilized by an atom (occurs at high neutral atom density)
        $$\mathrm{A}^+ + \mathrm{A} + e \rightarrow \mathrm{A}^* + \mathrm{A}$$
        $$\Gamma_{\mathrm{TBR},A} = ??$$
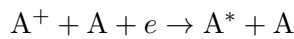
- Dielectronic recombination:
    $$\mathrm{A}^+ + e \rightarrow \mathrm{A}^{**} \rightarrow \mathrm{A}^* + h\nu$$

- Dissociative recombination:
    $$\mathrm{A}_2^+ + e \rightarrow \mathrm{A}^* + \mathrm{A}$$
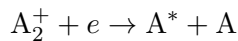
In the dielectronic recombination, the transfer of the excess energy to a bound electron seems to happen only at high temperatures ($\gg T_i$). Moreover, the dissociative recombination needs the presence of A_2^+ in the first place, which are created with $\mathrm{A}^+ + 2\mathrm{A} \rightarrow \mathrm{A}_2^+ + A$. The rate of A_2^+ formation being around $2 \times 10^{-43}\,\mathrm{s}^{-1}$ (unit problem ??), it is negligible in our time scale. Concerning the three mechanism of the collisional radiative recombination, the calculation of the rate with our experiment parameters (STP, 3 eV) show that the three body recombination rate is the dominant process.

Metastable atoms recombination and diffusion

Metastable atoms are neutral so they diffuse very slowly compared to ambipolar diffusion : $(D = 19\,\mathrm{cm^2\,Torr\,s^{-1}})$ [31]. In the afterglow, metastable atoms are relaxed by the following processes [31]:

- Two-body collisions with an atom in the ground state

    $A^* + A \rightarrow 2A$

- Three-body collisions with two atoms in the ground state

    $A^* + 2A \rightarrow A_2^* + A \rightarrow A_2 + A + h\nu$

- Collision with the plasma electrons

- Diffusion and relaxation on the walls

The main cause of decay in our experiment is the three-body collision with a rate of $7.6 \times 10^{-44}\,\mathrm{m^6 s^{-1}}$ [31] (to compare, the decay rate of A^+ is $4 \times 10^{-41}\,\mathrm{m^6 s^{-1}}$ at $3\,\mathrm{eV}$), in our experiment, it's on the timescale of $100\,\mathrm{ns} - 10\,\mathrm{\mu s}$ (depending of the pressure), which mean we can consider that none of the metastable atoms will decay between 2 pulses.

Calendar

Month(s)	Accomplished work
October - November	Phase matching
December	Atoms and ions dynamic
January - February	Dipole response & Absorption
March	Harmonic scaling
April-May	Square vs Gaussian density, writing report
June	Helium fraction, COMSOL simulations, Cavity study, Measurements

Bibliography :

[1] A McPherson, G Gibson, H Jara, U Johann, Ting S Luk, IA McIntyre, Keith Boyer, and Charles K Rhodes. Studies of multiphoton production of vacuum-ultraviolet radiation in the rare gases. *JOSA B*, 4(4):595–601, 1987.

[2] David Carlson. *Frequency Combs for Spectroscopy in the Vacuum Ultraviolet.* PhD thesis, University of Arizona, 2016.

[3] Christoph Gohle, Thomas Udem, Maximilian Herrmann, Jens Rauschenberger, Ronald Holzwarth, Hans A Schuessler, Ferenc Krausz, and Theodor W Hänsch. A frequency comb in the extreme ultraviolet. *Nature*, 436(7048):234–237, 2005.

[4] R Jason Jones, Kevin D Moll, Michael J Thorpe, and Jun Ye. Phase-coherent frequency combs in the vacuum ultraviolet via high-harmonic generation inside a femtosecond enhancement cavity. *Physical Review Letters*, 94(19):193201, 2005.

[5] Jan Rothhardt, Manuel Krebs, Steffen Hädrich, Stefan Demmler, Jens Limpert, and Andreas Tünnermann. Absorption-limited and phase-matched high harmonic generation in the tight focusing regime. *New Journal of Physics*, 16(3):033022, 2014.

[6] Carsten Winter. High-order harmonic generation. 2015. URL = `http://www.uni-muenster.de/Physik.PI/Zacharias/en/research/hh/hhg.html`.

[7] Aaron von Conta. An introduction to high-harmonic generation:towards high-harmonic spectroscopy. 2013. URL = `https://www.ethz.ch/content/dam/ethz/special-interest/chab/physical-chemistry/ultrafast-spectroscopy-dam/documents/lectures/spectroscopyFS13/projectsFS13/HHG_Instructions.pdf`.

[8] Paul B Corkum. Plasma perspective on strong field multiphoton ionization. *Physical Review Letters*, 71(13):1994, 1993.

[9] Thomas John Hammond. *Intracavity Generation of High Order Harmonics.* PhD thesis, University of British Columbia, 2007.

[10] Mette B Gaarde, Jennifer L Tate, and Kenneth J Schafer. Macroscopic aspects of attosecond pulse generation. *Journal of Physics B: Atomic, Molecular and Optical Physics*, 41(13):132001, 2008.

[11] Mette Borg Gaarde, F Salin, E Constant, Ph Balcou, KJ Schafer, KC Kulander, and Anne L'Huillier. Spatiotemporal separation of high harmonic radiation into two quantum path components. *Physical Review A*, 59(2):1367, 1999.

[12] TJ Hammond, Arthur K Mills, and David J Jones. Near-threshold harmonics from a femtosecond enhancement cavity-based euv source: effects of multiple quantum pathways on spatial profile and yield. *Optics express*, 19(25):24871–24883, 2011.

[13] Arthur K Mills, TJ Hammond, Matthew HC Lam, and David J Jones. Xuv frequency combs via femtosecond enhancement cavities. *Journal of Physics B: Atomic, Molecular and Optical Physics*, 45(14):142001, 2012.

[14] Mark Fox. *Optical properties of solids*, chapter 2. Oxford university press, 2001. URL = `http://www.phy.pku.edu.cn/~gwlyu/images/markfox.pdf`.

[15] Burton L Henke, Eric M Gullikson, and John C Davis. X-ray interactions: photoabsorption, scattering, transmission, and reflection at e= 50-30,000 ev, z= 1-92. *Atomic data and nuclear data tables*, 54(2):181–342, 1993. URL = `http://henke.lbl.gov/optical_constants`.

[16] JAR Samson and Wayne C Stolte. Precision measurements of the total photoionization cross-sections of he, ne, ar, kr, and xe. *Journal of electron spectroscopy and related phenomena*, 123(2):265–276, 2002.

[17] Philippe Balcou, Pascal Salieres, Anne L'Huillier, and Maciej Lewenstein. Generalized phase-matching conditions for high harmonics: The role of field-gradient forces. *Physical Review A*, 55(4):3204, 1997.

[18] MJ Kendrick, DH McIntyre, and O Ostroverkhova. Wavelength dependence of optical tweezer trapping forces on dye-doped polystyrene microspheres. *JOSA B*, 26(11):2189–2198, 2009.

[19] A Bideau-Mehu, Y Guern, R Abjean, and A Johannin-Gilles. Measurement of refractive indices of neon, argon, krypton and xenon in the 253.7–140.4 nm wavelength range. dispersion relations and estimated oscillator strengths of the resonance lines. *Journal of Quantitative Spectroscopy and Radiative Transfer*, 25(5):395–402, 1981. URL = `https://refractiveindex.info`.

[20] Amy Louise Lytle. *Phase Matching and Coherence of High-Order Harmonic Generation in Hollow Waveguides*. PhD thesis, University of Colorado, 2008.

[21] Helmholtz Gemeinschaft. Multiphoton ionization: New opportunities at flash. 2017. URL = `http://wof-cluster.desy.de/sites/site_photonscience/content/e58/e186104/e186825/e186879/index_print_eng.html`.

[22] LV Keldysh. Ionization in the field of a strong electromagnetic wave. *Zh. Eksperim. i Teor. Fiz.*, 47, 1964.

[23] Christian Spielmann, Clarence Kan, Neal H Burnett, Thomas Brabec, Michael Geissler, Armin Scrinzi, Matthias Schnurer, and Ferenc Krausz. Near-kev coherent x-ray generation with sub-10-fs lasers. *IEEE Journal of selected topics in quantum electronics*, 4(2):249–265, 1998.

[24] Gennady L Yudin and Misha Yu Ivanov. Nonadiabatic tunnel ionization: Looking inside a laser cycle. *Physical Review A*, 64(1):013409, 2001.

[25] AM Perelomov, VS Popov, and MV Terentev. Ionization of atoms in an alternating electric field. *Zhurnal Eksperimental'noi i Teoreticheskoi Fiziki (USSR) For English translation see Sov. Phys.-JETP (Engl. Transl.),* 50, 1966.

[26] A Barbet, N Sadeghi, and JC Pebay-Peyroula. Study of the electron-ion recombination processes in the xenon afterglow plasma. *Journal of Physics B: Atomic and Molecular Physics*, 8(10):1785, 1975.

[27] Einar Hinnov and Joseph G Hirschberg. Electron-ion recombination in dense plasmas. *Physical Review*, 125(3):795, 1962.

[28] PNB Neves, CAN Conde, and LMN Távora. A new experimental technique for positive ion drift velocity measurements in noble gases: Results for xenon ions in xenon. *Nuclear Instruments and Methods in Physics Research Section A: Accelerators, Spectrometers, Detectors and Associated Equipment*, 580(1):66–69, 2007.

[29] Earl C Beaty. Temperature dependence of the mobility of positive ions in argon and krypton. *Physical Review*, 104(1):17, 1956.

[30] Robert N Varney. Drift velocities of ions in krypton and xenon. *Physical Review*, 88(2):362, 1952.

[31] A Barbet, N Sadeghi, and JC Pebay-Peyroula. Decay of metastable xenon atoms xe*(3p2) in a xenon afterglow. *Journal of Physics B: Atomic and Molecular Physics*, 8(10):1776, 1975.

[32] Peter K Leichner, Kent F Palmer, JD Cook, and M Thieneman. Two-and three-body collision coefficients for xe (p 1 3) and xe (p 2 3) atoms and radiative lifetime of the xe 2 (1 u) molecule. *Physical Review A*, 13(5):1787, 1976.

[33] W Wieme. Decay of excited species in the afterglow of a pulsed discharge in xenon. *Journal of Physics B: Atomic and Molecular Physics*, 7(7):850, 1974.

[34] Daniel A Erwin and Joseph A Kunc. Ionization of excited xenon atoms by electrons. *Physical Review A*, 70(2):022705, 2004.

[35] E Constant, D Garzella, P Breger, E Mével, Ch Dorrer, C Le Blanc, F Salin, and P Agostini. Optimizing high harmonic generation in absorbing gases: Model and experiment. *Physical Review Letters*, 82(8):1668, 1999.

[36] Pablo U Suárez. An introduction to the split step fourier method using matlab. 2013.

[37] Xiao-Min Tong and Shih-I Chu. Theoretical study of multiple high-order harmonic generation by intense ultrashort pulsed laser fields: A new generalized pseudospectral time-dependent method. *Chemical Physics*, 217(2):119–130, 1997.

[38] MB Gaarde, Ph Antoine, Anne L'Huillier, KJ Schafer, and KC Kulander. Macroscopic studies of short-pulse high-order harmonic generation using the time-dependent schrödinger equation. *Physical Review A*, 57(6):4553, 1998.

[39] Jeffrey L Krause, Kenneth J Schafer, and Kenneth C Kulander. Calculation of photoemission from atoms subject to intense laser fields. *Physical Review A*, 45(7):4998, 1992.

[40] Maciej Lewenstein, Ph Balcou, M Yu Ivanov, Anne L'huillier, and Paul B Corkum. Theory of high-harmonic generation by low-frequency laser fields. *Physical Review A*, 49(3):2117, 1994.

[41] Steffen Hädrich, Jan Rothhardt, Manuel Krebs, Stefan Demmler, Arno Klenke, Andreas Tünnermann, and Jens Limpert. Single-pass high harmonic generation at high repetition rate and photon flux. *Journal of Physics B: Atomic, Molecular and Optical Physics*, 49(17):172002, 2016.

[42] CM Heyl, J Güdde, Anne L'Huillier, and U Höfer. High-order harmonic generation with μj laser pulses at high repetition rates. *Journal of Physics B: Atomic, Molecular and Optical Physics*, 45(7):074020, 2012.

[43] Ariel Paul, Emily A Gibson, Xiaoshi Zhang, Amy Lytle, Tenio Popmintchev, Xibin Zhou, Margaret M Murnane, Ivan P Christov, and Henry C Kapteyn. Phase-matching techniques for coherent soft x-ray generation. *IEEE Journal of quantum electronics*, 42(1):14–26, 2006.

[44] CM Heyl, CL Arnold, A Couairon, and A L'Huillier. Introduction to macroscopic power scaling principles for high-order harmonic generation. *Journal of Physics B: Atomic, Molecular and Optical Physics*, 50(1):013001, 2016.

[45] J Seres, E Seres, D Hochhaus, B Ecker, D Zimmer, V Bagnoud, T Kuehl, and C Spielmann. Laser-driven amplification of soft x-rays by parametric stimulated emission in neutral gases. *Nature Physics*, 6(6):455–461, 2010.

[46] S Kazamias, S Daboussi, O Guilbaud, K Cassou, D Ros, B Cros, and G Maynard. Pressure-induced phase matching in high-order harmonic generation. *Physical Review A*, 83(6):063405, 2011.

[47] Arthur K Mills, Sergey Zhdanovich, Alex Sheyerman, Giorgo Levy, Andrea Damascelli, and David J Jones. An xuv source using a femtosecond enhancement cavity for photoemission spectroscopy. In *SPIE Optics+ Optoelectronics*, pages 95121I–95121I. International Society for Optics and Photonics, 2015.

[48] DR Carlson, Jane Lee, John Mongelli, Ewan M Wright, and Ronald J Jones. Intracavity ionization and pulse formation in femtosecond enhancement cavities. *Optics letters*, 36(15):2991–2993, 2011.

[49] Henning Carstens, Maximilian Högner, Tobias Saule, Simon Holzberger, Nicolai Lilienfein, Alexander Guggenmos, C Jocher, T Eidam, D Esser, V Tosa, et al. High-harmonic generation at 250 mhz with photon energies exceeding 100 ev. *Optica*, 3(4):366–369, 2016.

[50] Richard A Keller and Nicholas S Nogar. Gasdynamic focusing for sample concentration in ultrasensitive analysis. *Applied optics*, 23(13):2146–2151, 1984.

[51] Robin Santra. Why complex absorbing potentials work: A discrete-variable-representation perspective. *Physical Review A*, 74(3):034701, 2006.

[52] David E Manolopoulos. Derivation and reflection properties of a transmission-free absorbing potential. *The Journal of chemical physics*, 117(21):9552–9559, 2002.

[53] James Grant-Jacob, Benjamin Mills, Thomas J Butcher, Richard T Chapman, William S Brocklesby, and Jeremy G Frey. Gas jet structure influence on high harmonic generation. *Optics express*, 19(10):9801–9806, 2011.